A Study of the Dysplastic Hip
Diagnosis, Morphology, and Treatment

PhD dissertation

Sepp De Raedt

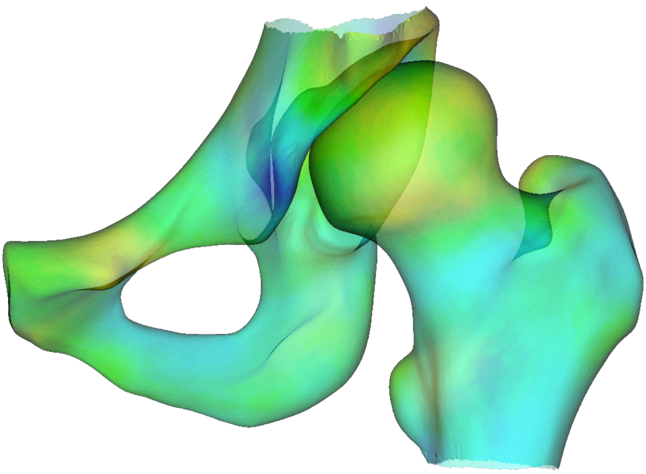

Health
Aarhus University
2015

A Study of the Dysplastic Hip
Diagnosis, Morphology, and Treatment

PhD dissertation

Sepp De Raedt

Health
Aarhus University
Department of Orthopaedic Research

AARHUS UNIVERSITY

Supervisors

Kjeld Søballe, Professor, Senior Consultant, MD, DMSc
Department of Orthopaedics
Aarhus University Hospital, Denmark

Marleen de Bruijne, Associate Professor, PhD
Departments of Radiology and Medical Informatics, Erasmus MC Rotterdam, The Netherlands
Department of Computer Science, University of Copenhagen, Denmark

Inger Mechlenburg, Associate professor, PT, MSc, PhD
Department of Clinical Medicine, Aarhus University, Denmark
Orthopaedic Research Unit, Aarhus University Hospital, Denmark

Maiken Stilling, Associate professor, MD, PhD
Department of Clinical Medicine, Aarhus University, Denmark
Department of Orthopaedics, Aarhus University Hospital, Denmark

Evaluation committee

Stephan M. Röhrl, Associate professor, Orthopaedic consultant, MD. PhD
Department of Orthopaedic Surgery and Neuroscience
Oslo University Hospital / Ullevål, Norway

Guoyan Zheng, Associate professor, PhD, PD
Institute for Surgical Technology and Biomechanics
University of Bern, Switzerland

Bente Langdahl, Professor, Consultant, PhD, DMSc (chairman)
Department of Endocrinology and Internal Medicine THG
Aarhus University Hospital, Denmark

Correspondence

Sepp De Raedt, MSc
Mobile: +45 2629 2686
E-mail: sderaedt@gmail.com

Department of Orthopaedics
Aarhus University Hospital
Tage-Hansens Gade 2, Building 10A
DK-8000 Aarhus C, Denmark

Acknowledgements

The research of this thesis was conducted from 2012 to 2015 at the Orthopaedic Research Group, at the Department of Orthopaedics, Aarhus University Hospital, THG.

I would like to thank my main supervisor Kjeld Søballe for the guidance and trust that he has shown and the opportunity to work on an exciting topic. I am also indebted to my supervisors Inger Mechlenburg and Maiken Stilling for always providing support and feedback. Without their help, this thesis would not have been possible. Inger's clinical insight and help has been invaluable throughout my time as a PhD student. Maiken's enthusiasm for research is infectious and her encouragement has been a great influence on both a personal and professional level. Finally, I am also sincerely thankful for the help and insight I have received from Marleen de Bruijne. Her experience and technical expertise have been crucial in development of the work presented in this thesis. I am grateful for the opportunity to work at the Erasmus MC in Rotterdam in the spring of 2014.

I would like to thank the patients and clinical staff that made this thesis possible. In particular I would like to thank Lone Rømer, Lissy F. Kristiansen, and colleagues at the Department of Radiology. Lone's expertise as a radiologist and willingness to perform manual measurements has been central to the validation of the methods developed in this thesis. I am thankful for the help and patience provided by Birthe Thykjær

Hansen and colleagues at the surgical department throughout the surgical studies.

My daily life as a PhD student would not have been the same without the company of the members of our research group. A special thank you goes to the other PhD students, scientific staff, the research coordinators, and Tina Kirkeby Stenumgaard. Coffee and cake makes any day better.

Finally, I would like to thank my friends and family for their support. Above all, I would like to thank my loving wife, Frøydis Slettevoll, and our son, Marius. I could not imagine what life would be without them. Her love, support, and encouragement have made it possible to complete my thesis and I look forward to the next chapter in our lives together.

Sepp De Raedt
April 29, 2015

The work of this thesis was generously supported by the Toyota Foundation, the Danish Orthopedic Association, the Danish Rheumatism Association, the Faculty of Health, Aarhus University, and Aarhus University Hospital.

List of papers

This thesis is based on the following papers:

I. De Raedt, S., Mechlenburg, I., Stilling, M., Rømer, L., Søballe, K., and de Bruijne, M. (2015c). Lunate Extract: Fully automatic acetabular lunate segmentation and hip angle measurements. *Submitted to Medical Image Analysis*

II. De Raedt, S., Achterberg, H. C., Mechlenburg, I., Stilling, M., Rømer, L., Søballe, K., and de Bruijne, M. (2015a). Morphology of the dysplastic hip and the relationship with gender and acetabular version. *Submitted to PLoS One*

III. De Raedt, S., Mechlenburg, I., Stilling, M., Rømer, L., Murphy, R. J., Armand, M., Lepisto, J., de Bruijne, M., de Bruijne, M., and Søballe, K. (2015b). Are computer reported measurements during periacetabular osteotomy using a minimally invasive approach reliable? *Submitted to Clinical Orthopedics and Related Research*

English summary

In the dysplastic hip, the acetabulum is typically described as being shallow with a steep roof and provides incomplete coverage of the femur. The incomplete coverage is thought to lead to increased pressure in the joint and result in pain and disability. Furthermore, it is believed to result in the early development of osteoarthritis. Hip dysplasia can be treated with joint preserving surgery if the correct diagnosis is given before development of osteoarthritis.

The aim of this thesis was to improve the use of three dimensional information by use of state-of-the-art techniques in the diagnosis and treatment of patients with hip dysplasia. The three studies therefore focus on three aspects related to hip dysplasia: diagnosis, morphology, and treatment.

In the first study, a method for the automatic segmentation of the lunate surface of the acetabulum is developed. The resulting lunate segmentation is used to automatically measure angles used in the diagnosis of hip dysplasia. The method is validated against repeated manual measurements by three raters on a dataset of 18 patients (36 hips). We find a good agreement between the manual and the automatic measurements and believe that the method will be invaluable for diagnosis and pre-operative planning for computer assisted joint preserving surgery in the future.

In the second study, the aim was to study the relationship between the morphology of the hip, gender, and hip dysplasia. This relationship was studied by the creation of combined CT-based statistical shape models of the pelvic bones and femur, while correcting for differences in femur pose. Using regression models and a novel method, we show the characteristic shape differences associated with both gender and hip dysplasia. An important finding was that acetabular anteversion was not significantly associated with hip dysplasia, but was associated with gender. This finding should be taken into consideration during corrective surgery in patients with hip dysplasia.

In the third study, the aim was to validate the use of a computer assisted surgery system when performing a joint preserving periacetabular osteotomy using a minimally invasive approach. The intra-operative angle measurements were compared to manual angle measurements and the reduction in peak pressure was calculated. A good agreement was found between the system reported angle measurements and manual angle measurements. The peak pressure in the hip joint was shown to be reduced post-operatively.

The three studies together contribute to a better understanding of the dysplastic hip and provide methods to aid clinicians in the diagnosis and treatment of patients with hip dysplasia. Although it has been shown that the treatment of hip dysplasia by periacetabular osteotomy is safe and offers a good long-term survivorship of the natural joint, it is unknown if the optimal correction of the acetabulum is achieved in all patients. In the future, the methods developed in this thesis may contribute to ensuring that all patients are treated optimally.

Danish summary

Ved hoftedysplasi er hofteskålen flad med et stejlt loft, der ikke dækker lårbenshovedet tilstrækkeligt. Den reducerede bæreflade menes at føre til forøget ledtryk og smerte samt nedsat funktion. Derudover antages den reducerede bæreflade at føre til tidlig udvikling af osteoartrose. Hvis man får stillet den korrekte diagnose inden udvikling af artrose, kan hoftedysplasi behandles med ledbevarende hofteoperation.

Formålet med denne afhandling var at forbedre anvendelsen af tredimensionel information ved brug af de nyeste teknikker ved både diagnose og behandling af patienter med hoftedysplasi. De tre studier fokuserer derfor på forhold relateret til hoftedysplasi: diagnose, hoftens morfologi og behandling.

I det første studie blev der udviklet en metode til automatisk segmentering af hofteskålens bruskbeklædte overflade. Den afgrænsede hofteskål blev anvendt til automatisk udmåling af vinkler, som anvendes til at stille diagnosen hoftedysplasi. Metoden blev valideret mod gentagne målinger af tre forskellige personer på et datasæt bestående af 18 patienter (36 hofteled). Der var god overensstemmelse mellem de manuelt og de automatisk målte vinkler. Metoden vil være særdeles værdifuld for at stille diagnosen samt for præoperativ planlægning af computer-assisteret ledbevarende hoftekirurgi i fremtiden.

I det andet studie var formålet at undersøge forholdet mellem morfolo-

gien af hofteleddet, køn og hoftedysplasi. Forholdet blev undersøgt ved at skabe en kombineret CT baseret "statistical shape" model af bækkenets knogler samt af lårbenet, korrigeret for lårbenets position under scanningen. Studiet viste, at forskelle i morfologien er associeret med køn og med hoftedysplasi. Et vigtigt fund var, at acetabulær anteversion ikke var associeret med hoftedysplasi men derimod med køn. Denne viden er vigtig at have, når man foretager ledbevarende hoftekirurgi på patienter med hoftedysplasi.

I det tredje studie var formålet at validere brugen af et computer-assisteret system under minimal invasiv ledbevarende hoftekirurgi. De per-operative acetabulære vinkler målt med det computer-assisterede system blev sammenlignet med manuelt målte vinkler. Ligeledes blev ledfladetrykket i hofteleddet målt. Der var god overensstemmelse mellem de acetabulære vinkler målt med det computer-assisterede system og med manuelt målte vinkler. Ledfladetrykket i hofteleddet blev reduceret efter operationen.

Disse tre studier bidrager tilsammen med en dybere forståelse af det dysplastiske hofteled. Ligeledes bidrager de med metoder, som kan hjælpe klinikeren til at stille diagnosen samt behandle patienter med hoftedysplasi. Skønt ledbevarende hoftekirurgi har vist sig at være en sikker behandling, der giver lang overlevelse af det biologiske hofteled, er det uvist om den optimale korrektion af hofteskålen opnås hos alle patienter. Metoderne udviklet i denne afhandling kan anvendes i forsøget på, at alle patienter i fremtiden behandles optimalt.

Contents

List of Figures

List of Tables

Acronyms

AASA	Anterior acetabular sector angle
AcAV	Acetabular anteversion angle
AI	Acetabular index
AIIS	Anterior inferior iliac spine
ANOVA	Analysis of variance
AP	Anteroposterior
ASIS	Anterior superior iliac spine
BGS	Biomechanical guidance system
CE	Center-edge
CT	Computed tomography
FAI	Femoroacetabular Impingement
HASA	Horizontal acetabular sector angle
HU	Hounsfield unit
ICC	Intraclass correlation coefficient
MRI	Magnetic resonance imaging

OA Osteoarthritis

PACS Picture archiving and communication system

PAO Periacetabular osteotomy

PDM Point distribution model

PASA Posterior acetabular sector angle

PCA Principle component analysis

SSM Statistical shape model

THA Total hip arthroplasty

1

Introduction

1.1 Medical imaging

Since the discovery of x-rays by Wilhelm Röntgen, it has become possible to image the structures inside the body without exploratory surgery. With the subsequent invention of ultrasound imaging and magnetic resonance imaging (MRI), similar non-invasive imaging can be performed, albeit without the use of ionizing radiation. Further developments have lead to the introduction of other modalities, which collectively have formed the field of medical imaging.

The ability to image the internal structures of the human body and obtain important diagnostic information has revolutionized the field of medicine. However, prior to every investigation a careful cost-benefit analysis must

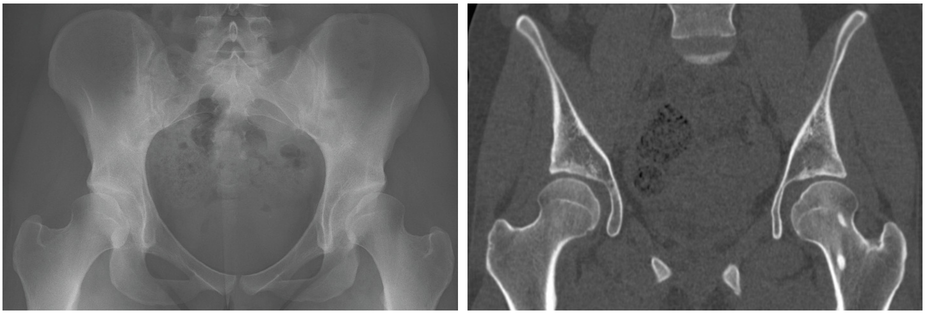

(a) (b)

Figure 1-1: An example of (a) a standard anterior-posterior standing radiograph and (b) a coronal slice of a CT showing the pelvis of a patient.

be taken into consideration. Depending on the modality, the cost may include a combination of the associated risks, acquisition time, and the economic costs. In investigations involving ionizing radiation, the associated risk importantly includes the increased risk to develop cancer. Naturally, the benefit to the patient should outweigh the cost associated with an investigation. Another important aspect that should be considered is if the information obtained by an investigation is being used optimally. This question is central to this thesis and has played an important role in its conception.

In the field of orthopaedic surgery, medical imaging is an essential tool in the diagnosis, treatment, and follow-up of many diseases. Due to the high mineral density of bone, x-ray based imaging techniques result in images with high contrast between bone and soft tissue. This facilitates the diagnosis of trauma related injuries, skeletal abnormalities, and diseases, when clinical and physical examinations are not sufficient.

The most common investigation used is projection radiography, sometimes referred to as conventional radiography or x-ray. In projection radiography, the three dimensional anatomy is projected onto a two dimensional imaging surface as shown in Fig. 1-1a. The x-ray source produces a short pulse of x-rays that travel through the patient and in the direction of the detector. The contrast of the image is created due to the absorption and scattering of the x-ray beam in the patient. X-ray photons that are not absorbed or scattered are detected by the detectors. The low cost, low radiation dose, and short acquisition time of projection radiographs has clear advantages over more advanced techniques used in the clinic. With excellent knowledge of the three dimensional anatomy, a radiologist or surgeon can interpret the two dimensional images and reach a clinical diagnosis. However, over-projection or superposition of different structures may conceal important information and prevent the correct interpretation. This effect can be seen by comparing Fig. 1-1 (a) to (b). In these cases, it is necessary to use more advanced techniques to obtain three dimensional information.

To obtain three dimensional information, computed tomography (CT) can be used. Tomography is a technique to obtain a visualization of a slice through the human body as shown in Fig. 1-1b. CT is based on the basic principle of obtaining a series of projection images by rotating the source and detector around the patient. The information contained in the projection images can then be combined in a process commonly referred to as reconstruction. The resulting images represent cross-sections through the scanned volume and can be used for further analysis. Typically, the individual slices may be viewed and distance and angle measurements may be performed. In addition, three dimensional models can be constructed in order to visualize the three dimensional structures as shown in Fig. 1-2. CT investigations are therefore commonly used to obtain a complete

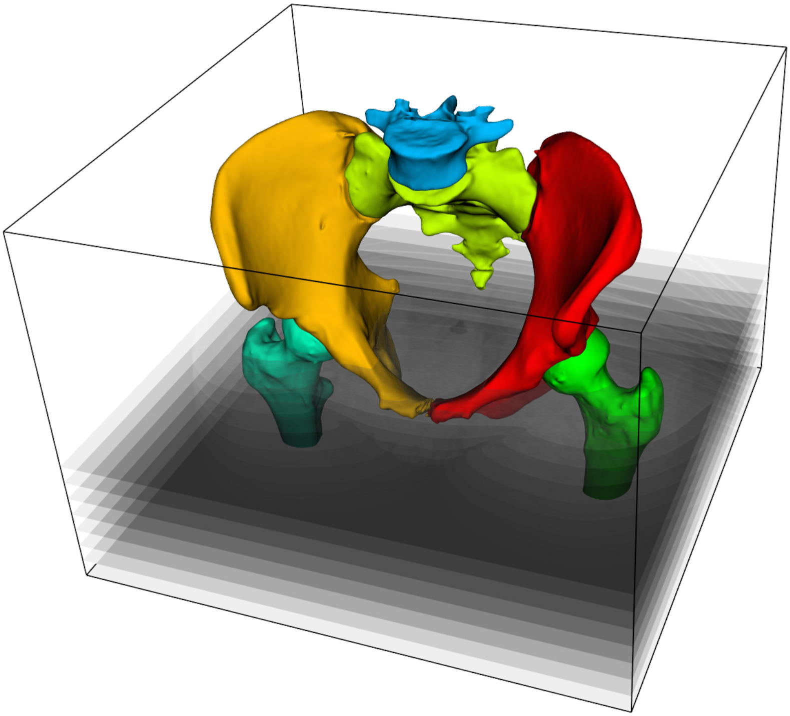

Figure 1-2: Visualization of axial slices acquired by computed tomography with bones visualized as colored surfaces. Axial slices are shown as transparent surfaces for visualization purposes.

picture of the three dimensional anatomy and bones.

However, often in clinical practice the three dimensional information is not used to the full extent possible. This may be due to the fact that two dimensional information is sufficient. However, another explanation may be that the tools or methods, and often software, is not available to perform the necessary analysis. The aim in this thesis was therefore to improve the use of the three dimensional information in the diagnosis and treatment of patients with hip dysplasia. The following sections will give a short introduction to quantitative image analysis and the basis for the key methods used in this thesis. Finally, we introduce hip dysplasia and the three aspects that are the focus of this thesis: diagnosis, morphology, and treatment.

1.2 Quantitative image analysis

The cornerstone of this thesis is the concept of quantitative image analysis. Meaning that we aim to use methods that provide quantitative measures upon which we can base conclusions and interpretations. This is in contrast to qualitative analysis, which is based on evaluating the quality without measuring. The following sections will introduce the concept of image segmentation.

Prior to discussing segmentation in the following section, it is important to define what an image is. Intuitively, an image may be described as a two dimensional representation for the purposes of visualization. A more formal definition is offered by Gonzalez and Woods[41], who define an image as a two dimensional function $f(x, y)$, where x and y are the spatial coordinates defined on the image plane. The value of the function or amplitude of f is then described as the intensity at the specified coordinates. Each of the coordinates of the image represent a pixel in two-dimensional images or a voxel in three dimensions.

In x-ray based imaging the intensity of the image is primarily a function of the settings of the x-ray machine and the amount of absorption and scattering. In CT imaging the intensity value is based on the attenuation in a voxel and is expressed in Hounsfield units (HU), which is named after the inventor of the CT scanner Sir Godfrey Houndsfield[85]. The Hounsfield unit of a voxel with an average attenuation coefficient of μ is defined as:

$$\mathrm{HU} = 1000 \times \frac{\mu - \mu_{water}}{\mu_{water} - \mu_{air}}, \tag{1-1}$$

where μ_{water} and μ_{air} are the linear attenuation coefficients of distilled water and air respectively, at standard temperature and pressure. At standard temperature and pressure, distilled water has a HU value of zero and air has a HU value of -1000. This linear transformation of the attenuation coefficient ensures that intensity values are comparable between (properly calibrated) machines or the same machine at different time points in ideal conditions.

1.2.1 Segmentation

In the general sense, segmentation is the process of dividing objects into different parts. In medical image segmentation, we are often interested in subdividing images into different anatomical structures. Depending on the application and field, this may be into different regions of the brain or as in this thesis into the individual bones of the hip joints. Although identifying individual bones is relatively easy for a human, the task is not trivial for a computer. In this section we will briefly introduce a few common methods used for bone segmentation.

In Fig. 1-3 a CT slice through the center of the head of the femur and the acetabulum is shown. For a human, with a little bit of training, it is easy to identify the femur and the pelvic bone. Therefore, the most obvious method to perform segmentation is to manually identify the bones of interest. This is however a time consuming procedure and suffers from both intra- and inter-observer variability. Therefore it is desirable to have

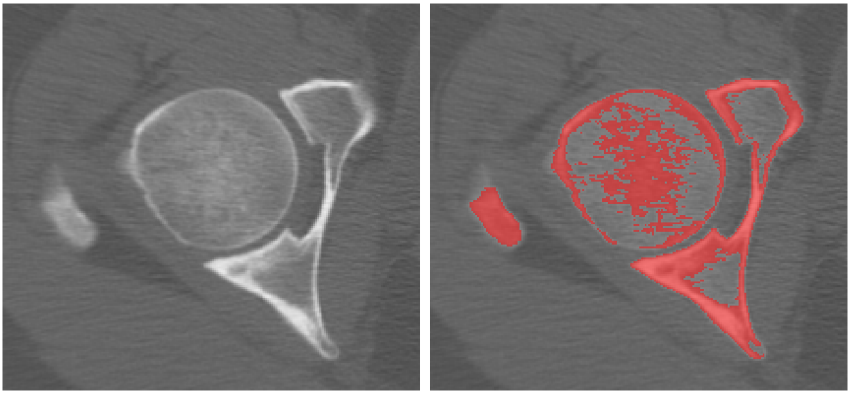

(a) (b)

Figure 1-3: An example (a) of a CT slice through the center of the femoral head. In (b), the image has been segmented with a threshold value of 350 HU.

automatic methods to perform the task of segmentation.

The most basic form of segmentation that is often used is thresholding. In thresholding, the image is divided into objects based on choosing a threshold intensity. As the intensity of a voxel is a function of the density of the object at the voxel location, an appropriate threshold should lie between the densities of the objects to be segmented. However, as can be seen in Fig. 1-3b, the resulting segmentation is not complete. This is due to the fact that the intensity of the trabecular bone is similar to that of soft tissue. Therefore more advanced techniques are needed.

In region growing, an initial area is identified by defining seeds and is subsequently grown by finding adjacent areas that are similar based on a defined set of properties, such as similar intensities[41]. This allows regions to grow until a neighboring area is found with different intensities. However, if the intensity difference is small at the edge of the object, the region may not stop and will proceed to “leak”. This problem is common for many segmentation techniques, such as watersheds and level-sets[20]. Possible solutions are to manually correct the segmentation or use prior knowledge to restrict the possible shape of the object to be segmented.

One method to restrict the shape, is through the use of statistical shape models. Statistical shape models capture the mean shape of a set of shapes and the main modes of variation based on principle component analysis[19]. In the point distribution model popularized by Cootes et al.[19], shapes are represented as points and the main modes of variation can be visualized by deforming the shape according to the modes of variation. The resulting models can be used to segment unseen examples or to study the morphological variability associated with disease or other dependent variables. For a complete introduction to the use of statistical shape models for image segmentation and other applications the reader is referred to Heimann and Meinzer[48] and Sarkalkan et al.[92]. One limitation to the use of statistical shape models is that since it is based on a set of example shapes, the model may not be able to accurately generalize to the segmentation or analysis of objects that are not sufficiently represented among the examples used for model construction.

A method that is not based on prior shape information, but still achieves accurate segmentations was introduced by Krčah et al.[60]. In this method, the segmentation procedure is based on the use of graph cuts and a cost function based on a sheetness measure. In graph cut segmentation, the image is represented as a graph structure with each voxel being a node and edges between neighboring voxels[12,13]. This method was shown to be more accurate than other state-of-the-art techniques, and to work well for femurs and other bones[60]. Obtaining accurate bone segmentations automatically greatly facilitates further quantitive analysis.

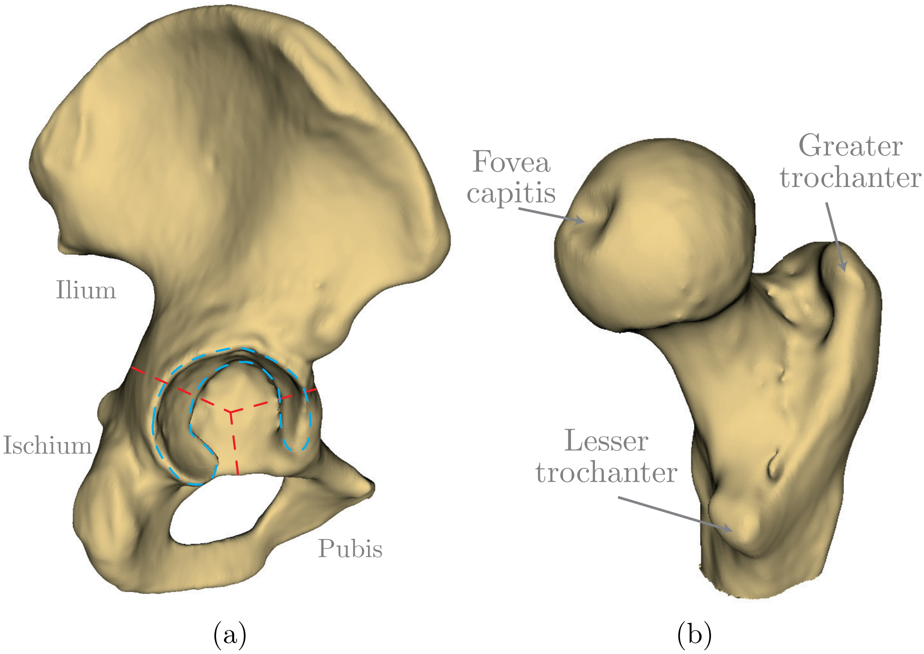

Figure 1-4: Illustration of (a) the right pelvis bone and (b) the proximal right femur bone. The acetabulum is formed by the joining of the ilium, pubis and ischium bones (red lines). The head of the femur fits in the acetabulum and articulates with the horse-shoe shaped lunate surface of the acetabulum (blue outline).

1.3 Anatomy of the hip joint

The hip joint is a ball and socket joint and is essential to human locomotion. The pelvic bones initially consist of three bones: the ilium, pubis, and ischium bones as shown in Fig. 1-4a. The three bones fuse together to form the acetabulum between the ages of 7 and 9 years, but skeletal maturity is not reached until the Y-shaped growth plate fuses between the ages of 14 and 16 years[30,107]. The acetabulum is a hemispherical socket

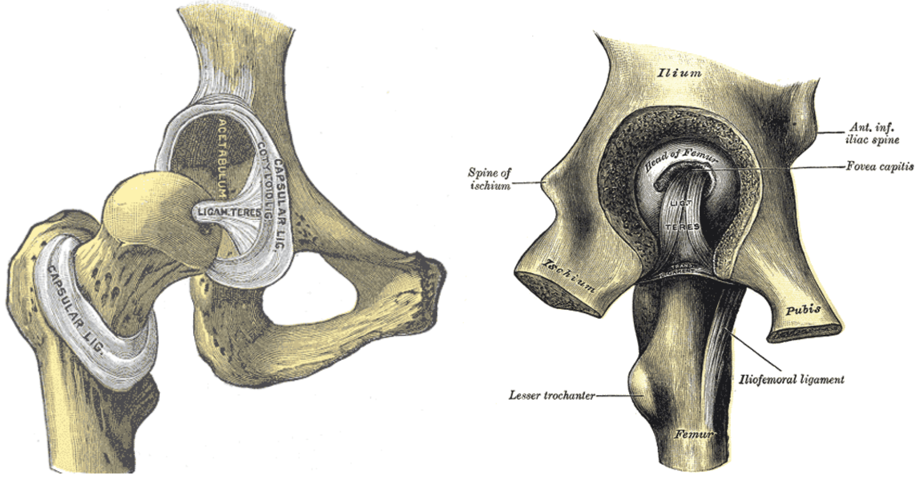

(a) (b)

Figure 1-5: Illustration of (a) the right hip joint and the insertion point of the foveal ligament. Illustration of (b) joint as seen from within the pelvis with part of the acetabulum removed for visualization. (Henry Vandyke Carter [Public domain], via Wikimedia Commons).

that together with the labrum covers approximately 50% of the femoral head[107]. The acetabular fossa is the centrally located depression of the acetabulum and is filled by the fatty tissue[107]. The horse-shoe shaped articulating surface of the acetabulum is known as the lunate surface and is lined by articular cartilage.

The femur bone is the longest and strongest bone in the human body and consists of the femoral head proximally and two condyles distally[44]. The head is hemispherical in shape and points in a medial, upward, and slightly forward direction[44]. The surface of the head is smooth and is covered by cartilage, with exception of a small depression known as the fovea capitis femoris as shown in Fig. 1-5b. The depression is the insertion point for the foveal ligament, which provides arterial supply to the femoral head during childhood and in case of fracture of the femoral neck in adults[103]. The proximal part of the femur is shown in Fig. 1-4b.

In the normal hip, the femur fits in the socket of the acetabulum and a stable joint is formed as shown in Fig. 1-5b. However, many different diseases of the hip exist for which this is not the case. In the following section, and the rest of the thesis, we will mainly focus on one of them: hip dysplasia.

1.4 Hip dysplasia

Hip dysplasia is a complex disease which may consist of a wide spectrum of developmental deformities of the hip joint[58]. It is associated with deformity of the femoral head, rotation of the femoral neck (femoral anteversion), an increased angle between the neck and shaft of the femur (coxa valga), and a shallow acetabulum[71,97]. However, the characteristic shallow acetabulum and steep roof, in the direction of the lateral edge, are the hallmark of hip dysplasia. The dysplastic acetabulum leads to the incomplete coverage of the femur. Although the coverage is globally deficient, the lack of coverage is most pronounced along the lateral and anterior aspect of the acetabulum[80]. Hipp et al. [51], found that the contact area was 26% smaller and the contact pressure was 23% higher in dysplastic hips compared to normal controls.

Together, these morphological abnormalities contribute to a reduced weight-bearing surface, which is believed to result in increased pressure in the hip joint[17,58,74,115]. This results in pain and disability and is thought to lead to the deterioration of the cartilage layer of the hip and the subsequent development of osteoarthritis (OA) at an early age[71,79,81,115]. Although the exact etiology is not completely understood, most authors agree that hip dysplasia is a significant risk factor for the development of OA[71,79]. In previous studies, it has been found that between 20.9% and as much as 47.9% of all osteoarthritic hips showed evidence of dysplasia[38,71,115]. Ganz et al.[40] proposed that in patients without hip dysplasia, the development of early osteoarthritis may be attributed to another hip disease known as femoroacetabular impingement (FAI). In FAI, the coverage of the femoral head is excessive or a deformity of the femoral head exists, which leads to the risk of impingement. In both hip dysplasia and FAI, the altered morphology is thought to be responsible for the development of osteoarthritis[40,58]. This is further supported by Harris[46], who found that the hip joint showed abnormalities at the cessation of growth in 90% of the cases diagnosed as primary OA. Therefore, it is clear that an important goal of the treatment of hip dysplasia is to normalize the joint mechanics and delay or prevent the development of osteoarthritis.

Patients with symptomatic hip dysplasia are typically female between the age of 20 and 40 years old[47,107]. However, the exact prevalence of hip dysplasia depends on the definition, measurement technique, ethnicity, and imaging used[54]. In the caucasian population the prevalence is thought to be approximately 3.5% and higher in the asian population[54]. In a study of the Sami population of Norway by Johnsen et al.[56], it was found that 38% had a center-edge angle of less than 25° and 17% had a center-edge angle under 17°.

1.5 Diagnosis

Diagnosis of hip dysplasia is typically based on a combination of physical examination and imaging investigations. In new borns, screening is performed to detect hip instability and possible dislocation. If abnormalities are suspected, further examinations using ultrasound are performed[26]. A similar diagnostic procedure may be used for young children. Abnormalities left untreated, may lead to the development of hip dysplasia in later life and can be treated by Rosen splint, Pavlik harness, or Frejkas pillow[107].

The main focus of this thesis however is hip dysplasia in adults. These patients have not previously been diagnosed or have been asymptomatic. The symptomatic patient commonly presents with persistent pain in the hip[107]. Typically a sharp pain located deep in the groin which can be provoked by hip flexion and internal rotation[42]. The diagnosis of acetabular dysplasia is confirmed by angle measurements on standardized standing anterior-posterior (AP) radiographs or CT.

When diagnosis is based on AP radiographs, the acetabular center-edge (CE) angle of Wiberg[115] and the acetabular index (AI) of Tönnis[107] are used, as illustrated in Fig. 1-6. The CE angle is the angle between the vertical line through the center of the femoral head and the line to the lateral edge of the weight-bearing edge of the acetabulum. Where the vertical line is perpendicular to the line connecting the teardrop line as shown in Fig. 1-6. This angle quantifies the coverage of the femoral head by the acetabulum and is generally accepted to be greater than 25° in normal hips[36,115]. A CE angle of less than 20° is classified as dysplastic. A CE angle between 20° and 25° is commonly termed borderline dysplastic[18,36,115]. The AI angle quantifies the steepness of the roof and is defined as the angle

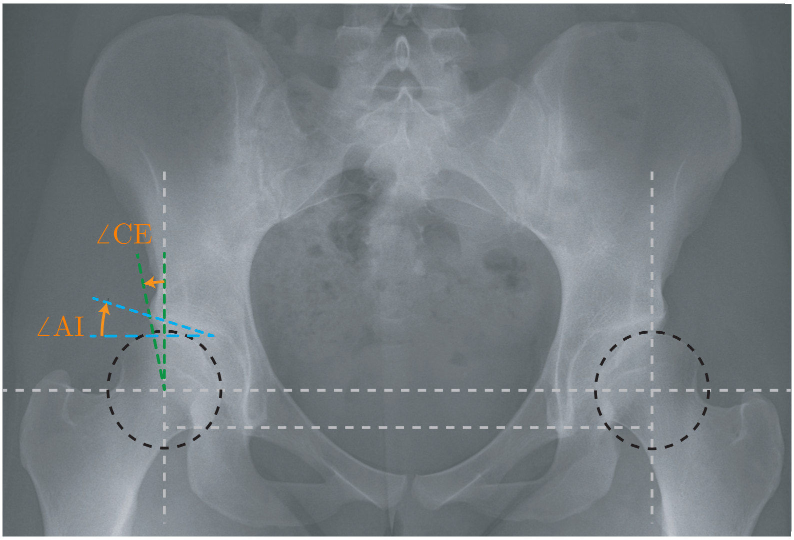

Figure 1-6: Radiograph showing the center-edge (CE) angle of Wiberg and acetabular index (AI) angle of Tönnis for the right hip.

between a horizontal line through the medial edge of weight-bearing sclerotic line of the acetabulum and a line tangent to the lateral edge of the sclerotic line[107]. In the normal hip the roof is nearly horizontal and the AI angle is less than 10°[107]. An AI angle of more than 10° is considered to be indicative of hip dysplasia[107]. However, the final diagnosis of hip dysplasia is commonly based solely on the threshold of the CE angle.

In some cases a CT investigation may be performed, especially prior to corrective surgery[27,110]. The CE and AI angle may be measured on a coronal slice through the center of the heads of the femurs, correcting for tilt and rotation of the pelvis as shown in Fig. 1-7a. In addition, the anterior and posterior coverage of the acetabulum may be quantified by the sector angles defined by Anda et al.[3] as shown in Fig. 1-7b. The anterior acetabular sector (AASA) angle and posterior acetabular sector

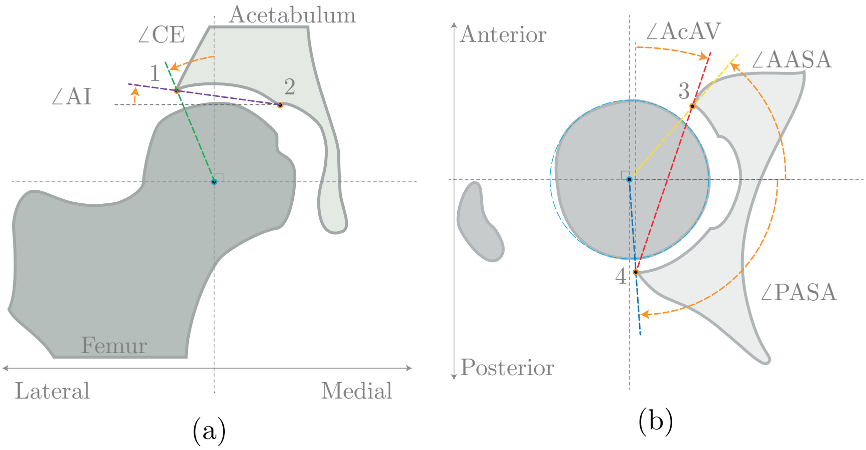

Figure 1-7: Illustration of angle measurements as performed on CT slices. (a) The center-edge (CE) and acetabular-index (AI) angle are measured in the coronal plane. (b) The acetabular-anteversion (AcAV), posterior-sector (PASA), and anterior-sector (AASA) angles are defined in the axial plane. The lateral, medial, anterior and posterior landmark points are numbered $1-4$ respectively.

angle (PASA) are defined in the axial slice through the centers of the femoral heads. The angles are measured between a line connecting the centers of the heads and the line tangent to the anterior and posterior edge of the acetabulum respectively. In addition the acetabular anteversion can be measured by the angle between an anterior posterior line through the posterior edge of the acetabulum and the line tangent to the anterior edge on the slice through the centers of the femurs[2,3].

The diagnosis using angle measurements on radiographs and CT are however time consuming and require an experienced radiologist. In addition, the measurements do not capture the complete three dimensional information available. Therefore, it is clear that automated and semi-automated methods to quantify the relationship between the femur and acetabulum are of great value. The ability to capture the three dimensional information may lead to an increased appreciation of the variation of the dysplastic hip and aid in the improvement of the treatment in patients with hip dysplasia.

In order to obtain the three-dimensional information, the lunate surface of the acetabulum must be identified. No previous methods have been presented to segment the lunate surface automatically. Initial work to quantify the coverage of the acetabulum was performed by Klaue et al.[59]. The coverage was measured by manually outlining the contour of the acetabulum on axial CT slices. Armand et al.[4] used a similar approach to outline the cartilaginous area on each slice and subsequently performed a spherical fit to obtain a three-dimensional surface approximating the lunate surface. In later work, Armiger et al.[5] refined the previously introduced method and named it Lunate Trace. This method is based on defining the center of the femoral head and manually annotating the medial and lateral edge of lunate surface on oblique slices through the center point. The smoothed outlines can then be used to calculate the diagnostic angles for the diagnosis of hip dysplasia. More recently, a similar approach was used by Steppacher et al.[100] on MRI images.

In research to determine the acetabular orientation, various authors have developed methods to identify the lateral edge of the lunate surface[89,104,113]. Wassilew et al.[113] used manually placed points along the lateral edge. Puls et al.[89], introduced an iterative procedure where points from the surface of the acetabulum within a threshold distance to an initially placed plane are projected to the plane and a distance map is created. A contour extracted from the distance map identifies new points of interest that are projected back to the surface, which are then used to recompute the plane orientation. This process is repeated until convergence. Tan et al.[104], find the lateral rim by using a level set method with a cost function based on surface curvature. Since these methods do not find the medial edge of the lunate surface, the acetabular index angle can not be calculated and the complete three-dimensional information is not obtained.

An alternative approach to determine the diagnostic angles is to identify the landmark points along the lateral, medial, posterior, and anterior edge of the lunate surface directly. Ehrhardt et al.[32], used an atlas based method to transfer manually placed points to a subject using registration. Subburaj et al.[101], performed analysis of the surface curvature of a pelvis surface and classified regions according to curvature characteristics. Anatomical landmarks were then identified by combining the curvature information with rules describing the relative position with respect to each other.

1.6 Morphology

The morphological variation of the pelvis is diverse and in clinical practice it is apparent that there is a wide spectrum of acetabular configurations which may combine subtle variations of different deformities. Understanding which variation may be associated with normal differences based on gender or ethnicity and pathological variation due to disease would provide valuable information in better understanding hip dysplasia and other hip related diseases.

It is well established that there are clear differences in the shape of the pelvis between genders[25]. The main differences between genders are the difference in angle of the pubic arch, the shape of the pelvic inlet, and

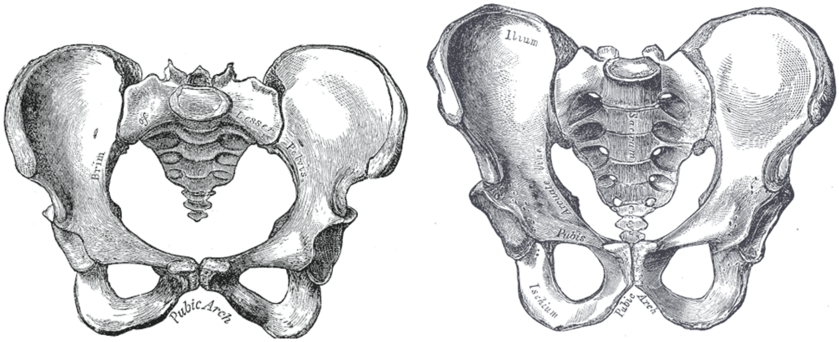

(a) Female (b) Male

Figure 1-8: Reference figures of the male and female pelvis. Indicative gender differences are the difference in angle of the pubic arch, shape of the pelvic inlet, and the width and height of the pelvis (Henry Vandyke Carter [Public domain], via Wikimedia Commons).

the width and height of the pelvis as illustrated in Fig. 1-8[25]. Although the female pelvis is smaller, it has a larger pelvic opening than the male pelvis[25]. The increased width creates a wider birth canal and aids during the process of child birth. However, it is also well established that the incidence of hip dysplasia is up-to four times higher in females than in males[39,47]. It is however unclear if the increased incidence of hip dysplasia in females may be attributed to morphological differences.

In patients with hip dysplasia, the morphological variation associated with coverage and version of the acetabulum is of primary interest. The steep roof and shallow acetabulum of the dysplastic hip results in the incomplete coverage of the femur[71,80,97]. The version of the acetabulum describes the orientation of the acetabular opening[73]. The acetabular opening may be orientated in a neutral position, anteriorly, or posteriorly and the acetabulum may be described as neutral, anteverted, or retroverted respectively. Understanding the version of acetabulum and the lateral coverage of the femur allows the surgeon to optimally treat dysplasia when corrective surgery is undertaken.

A statistical shape model (SSM) can be used to understand the morphological shape variation and the association with different charateristics[48,92]. The method was first introduced by Cootes et al.[19] and is based on using principle component analysis to describe the mean shape of a set of shapes and the main modes of variation. This method has been previously used to predict the development of OA and the risk of total hip replacement using a two-dimensional SSM[1,9,112]. Three-dimensional model was used in the study of patients with Legg-Calvé-Perthes and FAI[14,45]. No previous study has investigated the relationship between a combined femur and pelvis model and shape, gender, and hip dysplasia.

1.7 Treatment

When conservative treatment and general life-style improvements fail to alleviate symptoms, further treatment is needed. Since 1984, the Ganz or Bernese osteotomy, now commonly referred to as periacetabular osteotomy (PAO), has been the treatment of choice for young adults with hip dysplasia[39]. This procedure has a number of advantages over previous treatment options such as the triple or spherical acetabular osteotomies[94,99,107]. The posterior column remains intact, allowing immediate partial weight-bearing postoperatively and maintaining a stable pelvis[39]. The procedure maintains the blood supply[75] to the acetabulum and preserves the natural shape of the pelvis, while allowing full three-dimensional reorientation of the fragment[39].

During the procedure, the acetabulum is osteotomized and reorientated in order to improve the coverage of the femoral head and normalize the joint

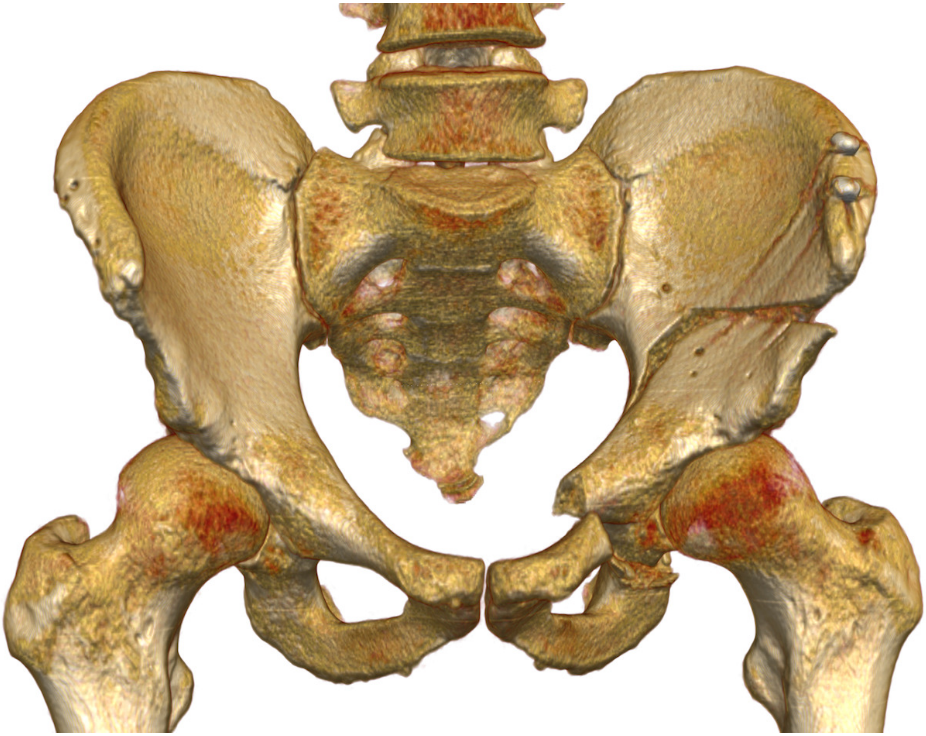

Figure 1-9: Post-operative volume visualization after PAO. The fragment has been reorientated to increase the lateral coverage and is fixated by two screws.

mechanics. The rationalization is that the reorientation will relieve pain and reduce the contact pressures of the joint and prevent, or at least delay, the onset of osteoarthritis[39]. In Fig. 1-9, a volume visualization created from a post-operative CT scan is shown.

However, since the initial introduction, a number of improvements have been achieved. In 2003, a new minimally invasive transsartorial approach was introduced which aimed to reduce the trauma to the soft tissue while maintaining the ability to achieve optimal reorientation of the fragment[108].

In addition, the procedure was found to reduce the intra-operative blood loss to 250 ml and shortened the length of surgery to 73 minutes[108]. Fixation of the acetabular fragment is achieved using two screws, which has been shown to be safe and stable after surgery using radiostereometric analysis[76].

Due to the difficulty of the procedure, there is a well established learning curve during both the approach and the correction[39,52,73,86,108,111]. During the procedure, single-plane fluoroscopy is used in order to determine the locations of the osteotomies and the correction applied. However, the three dimensional reorientation of the acetabular fragment can be difficult to fully capture solely by fluoroscopy. This is especially the case when the acetabulum is retroverted and the anterior and posterior coverage must be optimized[73]. In these cases, it would be advantageous to obtain realtime feedback on the three dimensional correction. This information may be obtained using intra-operative computer assisted surgery systems.

Computer assisted surgery systems are designed to help the surgeon intra-operatively and are commonly used in surgical specialities such as neurosurgery and orthopaedic surgery. Langlotz et al.[64], introduced the first computer assisted surgery system for tool tracking for PAO. This system allowed the tracking of the osteotomes during the surgery and helped the surgeon visualize the location of the cuts using information from a pre-operative CT. In later work, the authors enhanced the system to allow the tracking of the fragment during reorientation by reporting the applied rotations and translations[62,63]. The system reported rotations and translations may however be difficult to interpret, especially if rotations are applied in multiple directions simultaneously, as is often the case when correcting both the lateral and anterior coverage.

Another computer assisted surgery system named the Biomechanical Guidance System was later developed for assistance in PAO[4]. This system was developed with the goal to provide the surgeon with both radiological angle measurements and the pressure distribution in the joint in real time[5,68]. The system was found to be accurate and extensively validated using cadaver studies[5,78]. However, the system has not previously been validated using a minimally invasive approach.

2

Aim of the thesis

The overall aim of the thesis was to improve the use of the three dimensional information in the diagnosis and treatment of patients with hip dysplasia. Specifically, the aim was to develop computer methods to aid clinicians in the diagnosis and treatment of patients with hip dysplasia. These aims were realized within the following three studies.

Study I The first study aimed to develop methods to automatically measure the radiographic angles used in the diagnosis of hip dysplasia using CT images. We hypothesize that automatic measures are as reliable as manual measurements.

Study II The second study aimed to quantify the morphological variability of the pelvis and the relationship between morphology, gender, and hip dysplasia using a combined statistical shape model of the hip.

Study III The third study aimed to evaluate the accuracy of intra-operative computer reported angle measurements during periacetabular osteotomy using a minimally invasive approach and study the change in peak-pressure. We hypothesize that intra-operative angle measurements agree with manual measurements and that peak-pressure will decrease.

3

Methods and Materials

In the following sections a summary of the methods developed and used in the three studies of the thesis are introduced, including methodological considerations where relevant. Further methodological considerations will be discussed in the discussion. Subsequently, the study design, data, and experiments performed in the studies are presented.

3.1 Bone segmentation

All studies in this thesis required the segmentation of CT volumes to obtain three-dimensional representations of the bones. Therefore, a modified version of the automated method introduced by Krčah et al.[60] was developed and implemented. The core idea of the method is based on using the second order image information to formulate a cost function which is subsequently optimized by a graph cut optimization[12,13]. The procedure is illustrated in Fig. 3-1.

In a graph cut based optimization, a graph $\mathcal{G} =< \mathcal{V}, \mathcal{E} >$ with nodes $\mathcal{V}$ and edges $\mathcal{E}$ connecting neighboring nodes is defined[13]. The nodes may represent voxels in an image volume or vertices on a surface mesh and the edges are the connections between adjacent nodes[24]. In addition, a source node S and sink node T are introduced[12]. The cost function is defined as:

$$E(A) = \sum_{p \in \mathcal{V}} R_p(A_p) + \lambda \sum_{(p,q) \in \mathcal{N}} B(p,q) \cdot \delta_{A_p \neq A_q}, \tag{3-1}$$

where minimizing the cost function results in a binary labeling corresponding to the optimal segmentation in this application. This is achieved by finding the solution to the maximum flow/minimum cut problem, which completely separates the source S from the sink T on the graph $\mathcal{G}$[12]. The energy function $E(A)$ consists of two main components: the regional term $R_p(A_p)$ and a boundary term $B(p,q)$. The regional term is the associated cost for assigning a label A_p to node p. The boundary term is the associated cost for two neighboring nodes p and q. The term $\delta_{A_p \neq A_q}$ is 1 if $A_p \neq A_q$ and 0 otherwise. This ensures that no boundary cost is associated when the labels are the same. The relative importance of the two terms is determined by λ.

In this application, the regional term is used as an initialization by finding regions that can confidently be labeled as background and bone. The boundary cost function builds on previous work on the use of structure in segmentation of blood vessels, bronchi, and the sinus bone[29,35,93]. Specif-

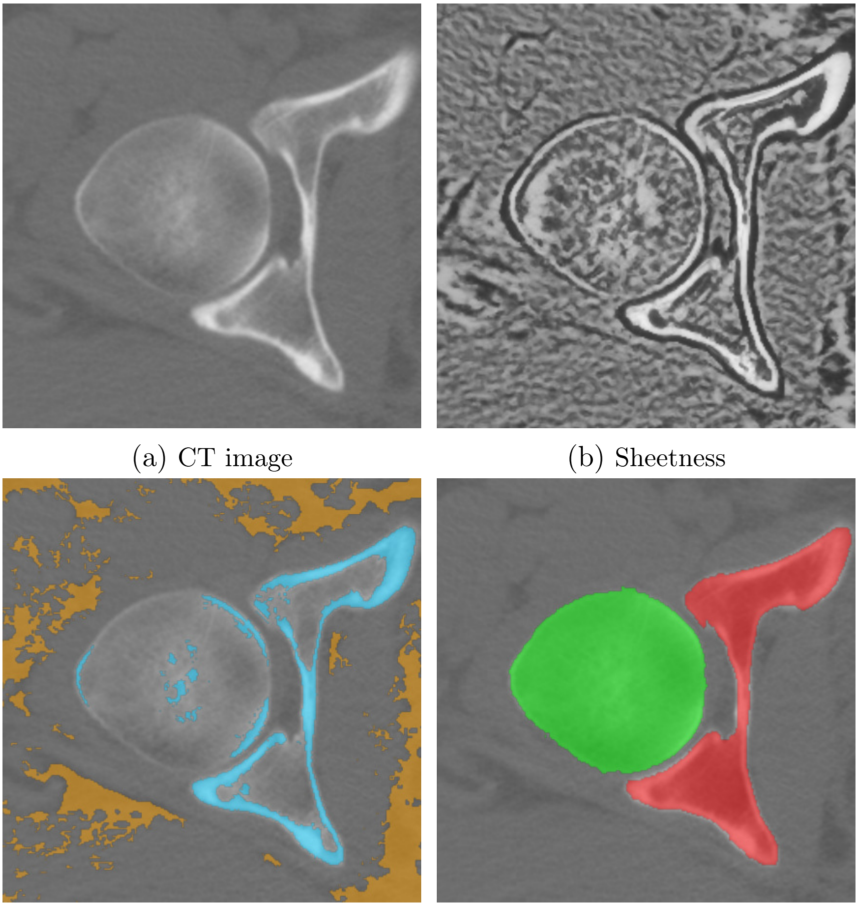

(a) CT image

(b) Sheetness

(c) Initialization

(d) Segmentation

Figure 3-1: The (a) input CT image is segmented by calculating (b) the sheetness measure in the boundary term and estimating (c) the initial regions for the regional term. Optimization of the graph cut results in (d) the final segmentation.

ically, eigen analysis of the hessian matrix is performed and the resulting eigenvalues are subsequently used to formulate a sheetness measure[60].

The eigenvalues are ordered by absolute value such that $|\lambda_1| \leq |\lambda_2| \leq |\lambda_3|$. An overview of the different measures from the literature and their properties are presented in Table 3-1. In our work, the following four ratios were used:

$$R_{sheet} = \frac{|\lambda_2|}{|\lambda_3|} \tag{3-2}$$

$$R_{tube} = \frac{|\lambda_1|}{\sqrt{|\lambda_2||\lambda_3|}} \tag{3-3}$$

$$R_{blob} = (2|\lambda_3| - |\lambda_2| - |\lambda_1|)/|\lambda_3| \tag{3-4}$$

$$R_{noise} = (\sum_{i}^{3} |\lambda_i|)/T, \tag{3-5}$$

where T is defined as the average of the sum of the absolute eigenvalues. The value of R_{sheet} and R_{tube} will be low for the corresponding structure and high when the structure is absent. In contrast with Krčah et al.[60], we choose to take the square root of the denominator in R_{tube} to make the measure dimensionless and allow for unbiased scale selection. Furthermore, this ensures that the value is bounded when the second eigenvalue is small as noted by Frangi et al.[35]. In addition we include R_{blob} as defined by Descoteaux et al.[28] which will be low for blob like structure[29]. Finally, the value of R_{noise} will be small for areas with little structure and small corresponding eigenvalues. The sheetness score $S(x)$ for a voxel x is defined as the product of these terms and is given by:

$$\begin{aligned} S(x) = \underset{\sigma\in\Sigma}{\operatorname{argmax}}\, S_\sigma(x) = &- sgn(\lambda_3)\cdot \\ &\left(\exp\left\{-\frac{R_{sheet}^2}{2\alpha^2}\right\}\right)\cdot \\ &\left(\exp\left\{-\frac{R_{tube}^2}{2\beta^2}\right\}\right)\cdot \\ &\left(1-\exp\left\{-\frac{R_{blob}^2}{2\eta^2}\right\}\right)\cdot \\ &\left(1-\exp\left\{-\frac{R_{noise}^2}{2\gamma^2}\right\}\right), \end{aligned} \tag{3-6}$$

The boundary cost is then defined as:

$$B(p,q) \propto \begin{cases} \exp\left\{-\frac{|S(p)-S(q)|}{\sigma_s}\right\}, & \text{for } S(p) \geq S(q), \\ 1, & \text{otherwise,} \end{cases} \tag{3-7}$$

where σ_s is a constant scaling factor that regulates the response.

The regional term is used as an initialization of the graph cut. The goal is to identify regions that can be confidently be identified as bone and background. The two regions are identified by the following relationships:

$$\begin{aligned} E_{bone} &= x \in \Omega | \mathcal{I}(x) \geq 400HU \wedge S(x) > 0, \\ E_{bkg} &= lcc(x \in \Omega | \mathcal{I}(x) < -50HU), \end{aligned}$$

where E_{bone} identifies voxels x in the image $\mathcal{I}$ that have a high intensity and positive sheetness. The background is taken as the largest connected component (lcc) of the input image with a low intensity. This ensures that low intensity voxels in trabecular bone are not included in the background.

Table 3-1: Overview of different measures used for analysis of structure.

Measure	Ratio	Sheet	Tube	Blob	Noise	Reference
R_{sheet} †	$\frac{\lvert\lambda_2\rvert}{\lvert\lambda_3\rvert}$	0	1	1	undef.	Descoteaux et al.[29], Frangi et al.[35], Krčah et al.[60]
R_{blob}	$\frac{2\lvert\lambda_3\rvert-\lvert\lambda_2\rvert-\lvert\lambda_1\rvert}{\lvert\lambda_3\rvert}$	2	1	0	undef.	Descoteaux et al.[29]
R_B	$\frac{\lvert\lambda_1\rvert}{\sqrt{\lvert\lambda_2\rvert\lvert\lambda_3\rvert}}$	0	0	$\frac{1}{\sqrt{2}}$	undef.	Frangi et al.[35]
R_{tube}	$\frac{\lvert\lambda_1\rvert}{\lvert\lambda_2\rvert\lvert\lambda_3\rvert}$	0	0	$1/2$	undef.	Krčah et al.[60]
R_{noise}	$\sqrt{\sum_i^3 \lambda_i^2}$	λ_3	$\sqrt{2}\lambda_3$	$\sqrt{3}\lambda_3$	0	Descoteaux et al.[29], Frangi et al.[35]
R_{noise} ‡	$\frac{\sum_i^3 \lvert\lambda_i\rvert}{T}$	$\frac{\lvert\lambda_3\rvert}{T}$	$\frac{2\lvert\lambda_3\rvert}{T}$	$\frac{3\lvert\lambda_3\rvert}{T}$	0	Krčah et al.[60]

†Frangi et al.[35] refer to R_{sheet} as R_A
‡T is the average sum of absolute eigenvalues

Finally, the regional term is defined as:

$$R_p(A_p) \propto \begin{cases} 1, & \text{if } A_p = \text{"}Bone\text{" and } p \in E_{bkg}, \\ 1, & \text{if } A_p = \text{"}Bkg\text{" and } p \in E_{bone}, \\ 0, & \text{otherwise,} \end{cases}$$

where an initial cost is associated with the regions previously introduced. Voxels that are not part of the two regions are assigned no initial cost.

3.2 Acetabular lunate segmentation

In Study I, a new fully automatic method for lunate segmentation was developed. The method is based on a two-step process that first segments the femur and acetabulum using the method described in Sec. 3.1. Subsequently, the lunate surface is segmented from the mesh using a graph cut with a novel cost function.

The distinguishing features of the lunate surface are the rim along the edge of the lunate and the congruency of the weight bearing surface between the acetabulum and the femoral head. Therefore two cost functions are introduced, one based on surface curvature and the other based on surface congruency between the femur and acetabulum. The curvature cost function was defined as:

$$B_\kappa(p,q) \propto \begin{cases} \exp\left\{-\frac{\kappa(p)^2}{\sigma_\kappa^2}\right\}, & \text{for } \kappa(p) > \kappa(q), \\ 1, & \text{otherwise,} \end{cases} \tag{3-8}$$

where $\kappa(p)$ is the curvature for point p and σ_κ is a constant scaling factor that regulates the curvature cost. The congruency cost was then defined as:

$$B_\theta(p,q) \propto \left(1 - \exp\left\{-\frac{(R_\theta(p)+\theta_c)^2}{\sigma_\theta^2}\right\}\right), \tag{3-9}$$

where R_θ is the dot product of the surface normals of point p and the closest point q on the surface of the femur. The constant scaling factors θ_c and θ respectively shift the boundary and regulate the congruency cost.

Finally a third combined cost function was introduced that combined the two curvature and congruency cost functions:

$$B_{combined}(p,q) \propto B_\kappa(p,q) \cdot B_\theta(p,q). \tag{3-10}$$

Similar to the bone segmentation, the region term is also used as an initialization by finding vertices on the mesh that can be confidently estimated to belong to the lunate surface and points that are not part of the lunate. This is shown in Fig. 3-2c, where the red points belong to the lunate surface and the blue points do not. Note however, that in this case some of the points on the lunate surface are incorrectly labeled (shown in blue). The resulting segmentation in Fig. 3-2d is however correct, due to the high boundary cost that would be introduced if the initial labeling would be preserved.

3.3 Automatic angle measurement

The resulting lunate segmentation can subsequently be used to automatically identify the landmark points to determine the diagnostic angles. The procedure consists of first determining the centers of the femoral heads by fitting spheres to the articulating surface of the femur[22]. Subsequently, orthogonal planes through the centers are determined to define the anatomic axis. Finally, an iterative ray projection procedure is used to determine the landmark points by rotating the ray perpendicular to the plane until the last intersection point is found as illustrated in Fig. 3-3.

3.4 Statistical shape model

In Study II, statistical shape models of the femur and pelvic bones were developed. The first step in the building of statistical shape models is to obtain shapes with corresponding points. The complete pipeline to achieve this is shown in Fig. 3-4. Input images are first preprocessed by segmenting each of the bones and creating masks to limit the region of interest for

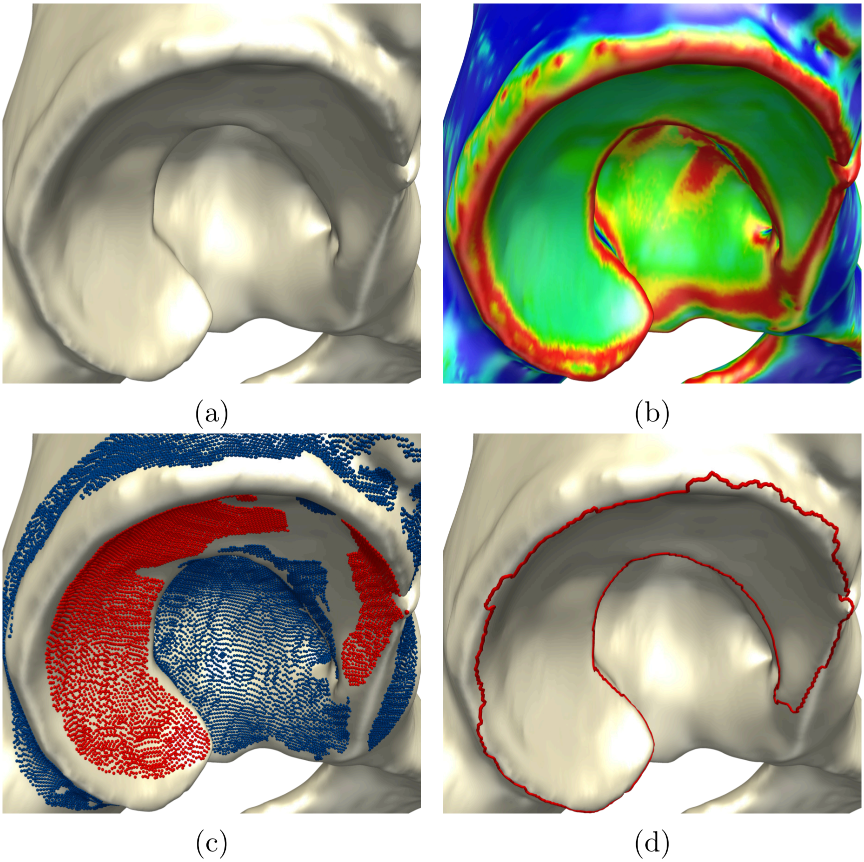

Figure 3-2: (a) Input surface of the acetabulum. (b) shows the (undirected) combined curvature and congruency cost function. Red regions introduce a low cost and blue high cost. (c) points . Note that some points on the lunate surface are incorrectly initialized, however the resulting segmentation is correct as shown in (d).

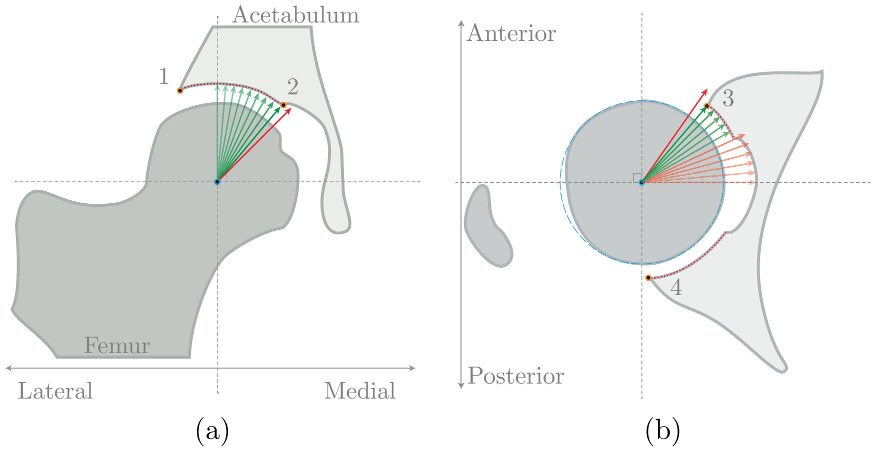

Figure 3-3: Illustration of the automatic landmark detection procedure. The red dotted line illustrates the segmented lunate surface. The green arrows indicate rays from the center of the femur that intersect the lunate surface. In (a) the ray is rotated until the medial edge is detected. The same procedure is used to detect the anterior edge in (b). The procedure is then repeated for the lateral and posterior edges.

registration. The input images and mask images are then used to perform non-rigid image registration. By averaging the individual registrations, each input image can be transformed to a mean space from which a mean shape is created. The mean shape can then be transformed by the inverse transformation to obtain individual shapes with point correspondences[96].

3.4.1 Shape alignment and pose correction

After point correspondences have been determined, the shapes must be aligned. This is typically achieved by performing generalized procrustes analysis[43] to optimally align and scale shapes. Aligning the combined femur and pelvis shapes directly would however result in statistical shape

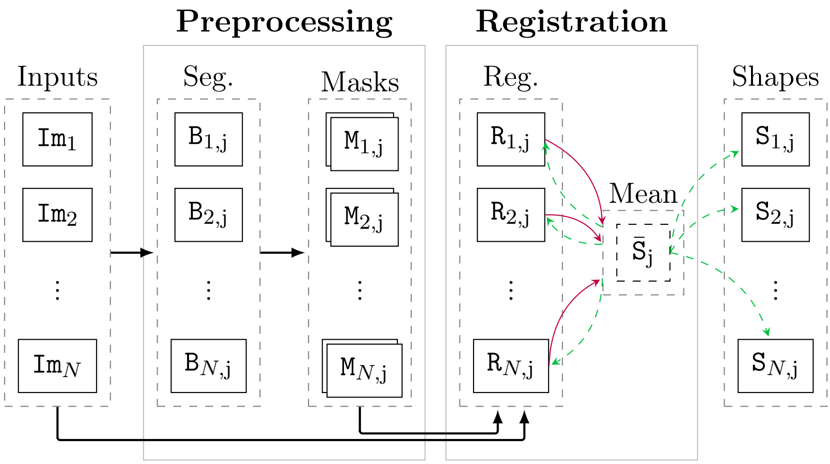

Figure 3-4: Overview of the complete pipeline used to obtain shapes of the femur and pelvic bones with corresponding points for the creation of statistical shape models. Each input image $\mathtt{Im}_i$ is segmented, producing a binary segmentation $\mathtt{B}_{i,j}$ for subject i and bone j. The mask images $\mathtt{M}_{i,j}$ and input images are then used to perform pairwise registrations $\mathtt{R}_{i,j}$. $\bar{\mathtt{S}}_j$ is the mean shape obtained from the mean soft mask image and $\mathtt{S}_{i,j}$ are the individual shapes.

models that modeled differences in pose of the individual patients at the time of scanning. Therefore a new procedure was developed to correct for pose, while maintaining the position of the femur with respect to the acetabulum.

First the combined left and right pelvis bones are aligned using procrustes analysis to remove pose and scaling differences. Subsequently, the same transformation is applied to the left and right femur bones and the centers of the femoral heads are calculated using sphere fitting[22]. In order to remove the differences in pose of the femur, the left and right femurs are separately aligned using only translations and rotations. However, after alignment the center of each femur is restored to its initial position. The pose correction is repeated until convergence.

3.4.2 Regression analysis

In Study II, a new method was developed to visualize the characteristic differences in shape based on regression analysis. The novel method allows the relationship between shape and dependent variables such as gender, dysplasia, and angle measurements to be studied. The procedure is based on creating logistic or linear regression models for the dependent variables based on the shape parameters. Subsequently, the regression coefficients can be used to visualize the characteristic shape differences by deforming the mean shape along the discriminating direction.

3.5 Computer assisted surgery

In Study III, a computer assisted surgery system was used to perform minimally invasive PAO using a transsartorial approach. In this study, the Biomechanical Guidance System (BGS) developed at John Hopkins University by Armand et al.[4] was used. The system allows the real-time calculation of diagnostic angles and joint pressure using finite element analysis.

The system consists of a Polaris optical tracking system (Northern Digital Inc., Waterloo, Canada), a workstation, and a surgeon display as shown in Fig. 3-5a. In addition, three optically tracked tools were used:

- Optically tracked pointer - An optically tracked pointer used for collecting data points,
- Calibration reference - Used for calibration of the pointer,
- Reference geometry - Removable reference geometry (BrainLab, Feldkirchen, Germany).

3.5.1 Pre-operative workflow

Pre-operatively the patient underwent CT scanning according to a standardized protocol. The bony pelvis and the femurs were automatically segmented using the method described in Sec. 3.1 and surface models were created. The lunate surface was segmented using the lunate-trace method developed by Armiger et al.[5]. Finally, a pre-operative plan based on the biomechanically predicted optimal alignment was made using the BGS software. The workflow is shown in Fig. 3-6.

3.5.2 Intra-operative workflow

Prior to the start of surgery the optical tracker is positioned on the contralateral side. While the surgeon performs the opening and initial ap-

(a)

(b)

Figure 3-5: Shown in (a) is the Biomechanical Guidance System consisting of a optical tracking system, a workstation, and a monitor for the surgeon. In (b), the optically tracked pointer, reference geometry, and calibration reference are shown with the base of the reference geometry fixated on the contralateral side.

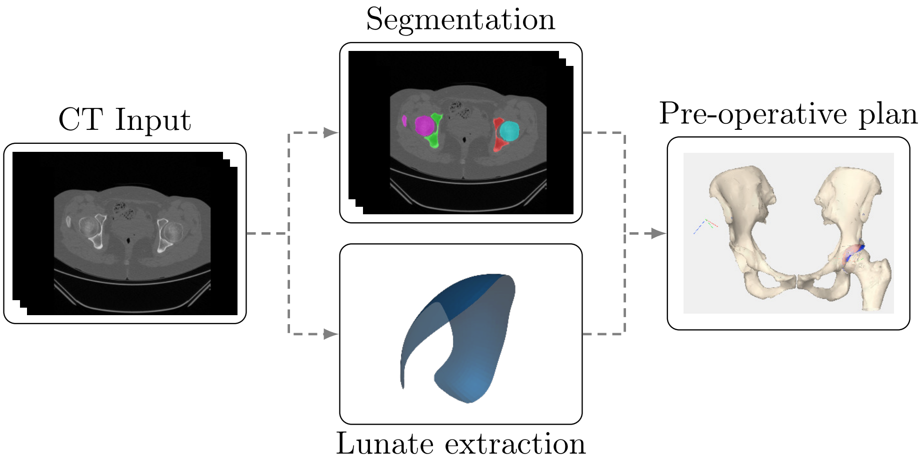

Figure 3-6: The pre-operative workflow consists of acquiring a CT scan, segmenting the bones and lunate, and creating a pre-operative plan.

proach, the surgical assistant performs a pivot calibration of the optically tracked pointer. This allows the tip of the pointer to be accurately tracked by the navigation system. Subsequently, the base of the reference geometry is attached on the contralateral side. The reference geometry establishes a fixed reference frame allowing the tracking of the fragment after the osteotomy is completed. The pelvis surface model is registered to the patient anatomy in a two step process. First an initial transformation is calculated by indicating the superior iliac spines on both sides and the inferior iliac spine on the operative side on the model and patient. This establishes an approximate alignment. The registration is refined by collecting surface points on the ilium, pubis, and the iliac crest and performing a point to surface registration[10]. Prior to the final osteotomy, four evenly spaced indentations (fiducials) are created using a 1 mm bone burr on the planned fragment. The position of the fragment can then be determined by touching the fiducials in the same order with the optically tracked pointer.

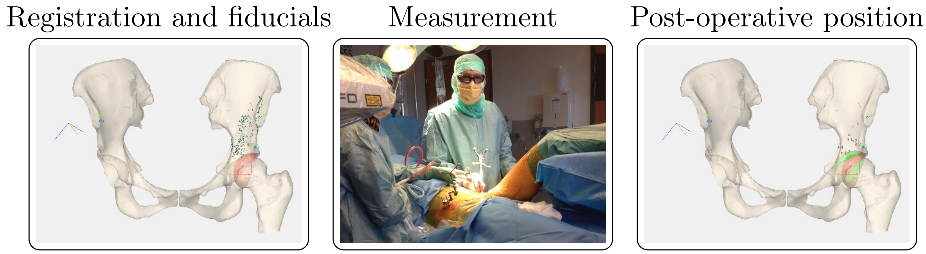

Figure 3-7: The intra-operative workflow consists of three stages. (Left) First a registration is performed to align the pre-operative CT model to the patient. (Middle) Subsequently measurements are acquired prior and after re-orientation to determine the position of the fragment. (Right) The post-operative position is graphically displayed and all measurements are shown separately.

After, the last osteotomy is completed and the fragment is repositioned, the new fragment position can be calculated. The repositioning of the fragment was achieved by fluoroscopic guidance according to the surgeons usual procedure. The main steps of the intra-operative workflow is shown in Fig. 3-7.

3.6 Study Design

Study I and Study II were retrospective cross-sectional studies. Study III was a prospective case series study.

3.7 Data

3.7.1 Study I & II

For the validation of the methods developed in Study I and Study II a dataset was retrospectively collected of patients that underwent CT investigation of the hip between January 2006 and October 2008. All patients were referred for scanning due to symptomatic hip pain, most commonly due to suspected primary or secondary hip dysplasia. Patient characteristics are shown in table Table 3-2.

Scans were acquired using a standardized protocol with the patient in a supine position and legs in a neutral position. The scan volume ranged from below the lesser trochanter until superior to the acetabulum. Scans were acquired on a Philips Mx8000, Philips Brilliance 40, or Philips Brilliance 64 (Philips Medical Systems, Best, The Netherlands). The mean voxel size was $0.45\,\mathrm{mm} \times 0.45\,\mathrm{mm} \times 1.25\,\mathrm{mm}$. The in-plane and out-of-plane voxel size ranged from $0.38\,\mathrm{mm}$ to $0.52\,\mathrm{mm}$ and $1.25\,\mathrm{mm}$ to $1.6\,\mathrm{mm}$ respectively.

In Study I, a subset of 18 patients (36 hips) were selected for the validation of the automatic lunate segmentation and 23 patients (46 hips) were used for the parameter optimization of the automated method.

In Study II, a subset of 75 patients (150 hips) were used for the creation of the statistical shape models.

3.7.2 Study III

All patients scheduled for PAO between September 2013 and January 2014 were identified for inclusion in Study III. Inclusion criteria were:

Table 3-2: Patient characteristics for patients that underwent CT investigation of the hip (N=96).

Parameter	Value
Age (Years)	
Median	36
Range	13 to 65
Sex	
Female	63 (67.7%)
Male	33 (34.3%)
Indication for CT investigation	
Dysplasia	73 (76%)
Impingement	7 (7.3%)
Legg-Calvé-Perthes	2 (2%)
Other	14 (14%)

- radiological diagnosed dysplasia (center-edge angle $< 25°$);
- osteoarthritis degree ≤ 1 on the Tönnis scale;
- symptomatic hip pain.

The exclusion criteria were:

- Legg-Calvé Perthes disease;
- neuromuscular diseases;
- previous major hip surgery;
- persons with cognitive problems;
- age ≤ 18 years.

The number of patients that could be included per operative day was limited to one due to the need to clean and sterilize the surgical equipment after each procedure. Therefore, when multiple candidates were available the surgeon selected the most technically challenging patient.

Ethical approval was obtained from the Central Denmark Region Committee on Biomedical Research Ethics (Journal number: M-20100274) and the study was registered at ClinicalTrials.gov (NCT02015247). Written consent was obtained from all included patients.

Scans were acquired on a Philips Brilliance 64 (Philips Medical Systems, Best, The Netherlands). A standardized protocol was used and the patient was in a supine position with legs in a neutral position. The scan volume ranged from below the lesser trochanter until superior to the L5-S1 joint. All scans were acquired with a voxel size of $0.45\,\text{mm} \times 0.45\,\text{mm} \times 0.7\,\text{mm}$.

3.8 Experiments

3.8.1 Study I

The automatic angle measurement method based on the lunate segmentation method developed in Study I, was validated against manual measurements by raters with different levels of experience. The manual measurements were performed using a standardized workflow, consisting of:

1. Selecting the centers of the femoral heads;
2. Automatic reformatting of the volume to align the centers of the femoral heads;
3. Selecting the reference landmarks;

4. Automatic calculation of the angle measurements.

To aid the rater in finding the center of the head a sphere with an adjustable radius was shown on each orthogonal view.

All measurements were performed independently and blinded from previous measurements. A second rating was performed by all raters with at least one month between ratings.

Landmark placement

Two experiments were performed to determine the accuracy of identifying the landmarks used for angle measurements. The first experiment quantified the manual raters ability to identify the same landmark on repeated readings by calculating the euclidean distance between the manual raters repeated measurements.

For the second experiment a mean landmark position (geometric average) was calculated for the raters first rating. Subsequently, the distance to the mean landmark was calculated for all raters and the automatic method.

Angle measurement

Two experiments were performed to determine the accuracy of measuring the diagnostic angles based on the identified landmarks. The first experiment compared the raters ability to measure the same angle by comparing the difference between the repeated measurements.

For the second experiment, the mean angle measurement for the raters first measurement was calculated. Subsequently, the difference with the raters second measurement was calculated and analyzed.

Statistics

Differences between measurements were evaluated graphically and by analysis of variance (ANOVA). ANOVA results were corrected for multiple comparisons with Box's conservative epsilon. Significant differences between raters were determined with the Tukey HSD *post-hoc* test and are reported as mean differences, p-value, and 95% confidence intervals. Significance was set at $p \leq 0.05$. Non-normally data was log transformed before analysis. All analysis was performed with STATA 13 (StataCorp, College Station, USA).

3.8.2 Study II

The methods developed in Study II, were used to study the relationship between hip dysplasia, gender, and the morphology of the hip.

Gender differentiation

To determine the association between gender and the morphology of the hip a complete statistical shape model of the left and right pelvic bones and femurs was created. Subsequently, a logistic regression model was created to determine the characteristic differences between men and women.

Hip dysplasia

To determine the morphological differences between dysplastic and non-dysplastic hips, two separate models of the combined pelvic bone and femur were created for the left and right side. Subsequently, logistic regression models were created to determine the characteristic differences between dysplastic and non-dysplastic hips.

Diagnostic angle measurements

To determine the association between angle measurements and the morphology of the hip, linear regression models were created with the center-edge, acetabular index, and acetabular anteversion angle.

The association between angle measurements, gender, and hip dysplasia was determined by two-way mixed effects ANOVA model with one within-subject factor (left and right side) and two between-subject terms for gender and hip dysplasia with interaction between side and both between-subject terms.

Statistics

All regression models were evaluated using leave-one-out cross-validation. Area under the curve was used to evaluate logistic regression models. Linear regression models were evaluated with correlation and residual plots including the limits of agreement. Significance was set at $p \leq 0.05$. All analysis was performed with STATA 13 (StataCorp, College Station, USA).

3.8.3 Study III

In Study III, the Biomechanical Guidance System was used to intra-operatively measure the diagnostic angles and peak-pressure during PAO surgery using a minimally invasive approach. The intra-operative measurements were compared to manual measurements on pre- and post-operative CT scans.

Statistics

Differences in angle measurements were investigated by summary statistics, the intraclass correlation coefficient (ICC), and Bland-Altman plots to examine bias and limits of agreement[11]. The change in post-operative peak-pressure was calculated as a percentage with respect to base-line. All analysis was performed with STATA 13 (StataCorp, College Station, USA).

4

Summary of results

4.1 Study I

4.1.1 Landmark placement

In the first experiment we found no difference between raters in the ability to determine the center (p=0.17), anterior (p=0.17), and posterior (p=0.9) landmark points. A statistically significant difference was found between rater 3 and rater 2 for both the AI ($-1.8°$, p=0.004, 95% CI:-3.1,-0.49) and the AcAV ($1.1°$, p=0.001, 95% CI:0.37,1.75) angle. The results are shown in Fig. 4-1a.

In the second experiment we found no difference in distance to the mean landmark points between the automatic method and the manual raters.

Table 4-1: Summary statistics for the distance (mm) to the mean landmark position for raters and the automatic method.

Landmark	Mean	Std. Dev.	Min.	Max.
Center	0.92	0.58	0.17	3.58
Anterior	1.06	0.54	0.26	3.42
Posterior	1.41	0.99	0.12	5.91
Lateral	1.37	0.95	0.23	6.1
Medial	1.99	1.98	0.07	10.8

The summary statistics are shown in Table 4-1. The results are shown in Fig. 4-1b.

4.1.2 Angle measurement

Analysis found no statistically significant difference between raters in repeated measurement of the CE (p=0.32), AASA (p=0.08), and PASA (p=0.09) angles. A statistically significant difference was found for both the AI (-1.8, p=0.004, 95% CI:-3.1,-0.49) and the AcAV angle (1.1, p=0.001, 95% CI:0.37,1.75) between rater 2 and 3. The results are shown in Fig. 4-2a.

Analysis found no statistically significant differences between raters and the automatic method for the AASA (p=0.1) and PASA (p=0.08) angles. For the CE angle, a statistically significant difference was found between the automatic method and rater 3 (2.44, p=0.001, 95% CI:0.84, 4.03). For the AI angle, a statistically significant difference was found between rater 3 and rater 2 (1.54, p=0.031, 95% CI:0.1,3.0) and the automatic method and rater 3 (-2.23, p=0.001, 95% CI:-3.68,-0.79). For the AcAV angle, a statistically significant difference was found between the automatic method

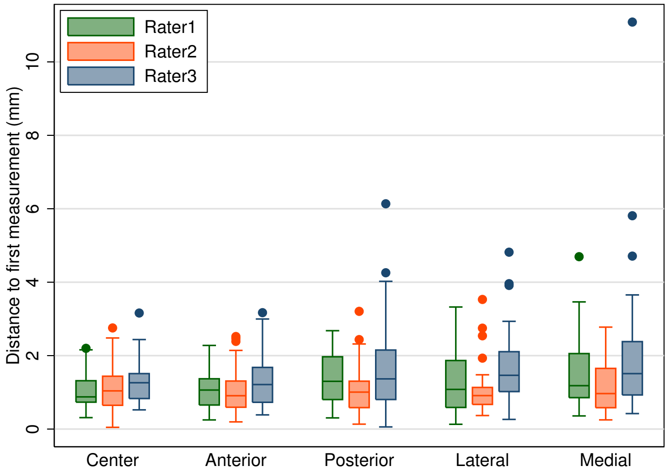

(a)

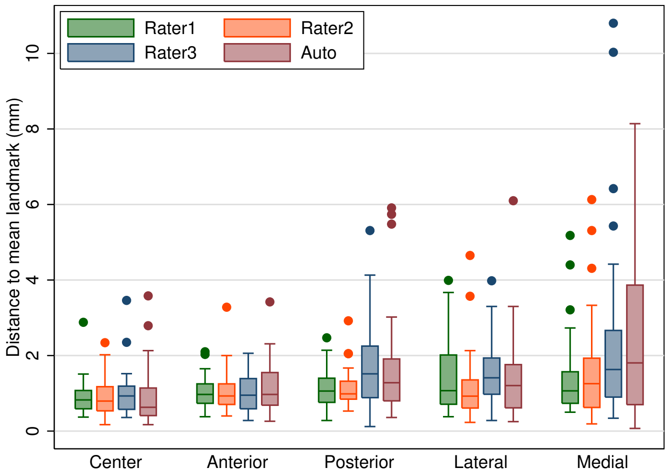

(b)

Figure 4-1: Comparison between landmark position. In (a) the distance to the raters first rating is shown. In (b) the the distance to the mean landmark is shown for each of the raters and the automatic method.

Table 4-2: Intraclass correlation coefficient for each angle measurement and 95% confidence interval.

Angle	ICC	95 % CI	
Center-edge	0.96	0.93	0.98
Acetabular index	0.94	0.89	0.96
Anterior sector	0.99	0.98	0.99
Posterior sector	0.96	0.94	0.98
Acetabular anteversion	0.99	0.98	0.99

and rater 2 (-0.78, p=0.004, 95% CI:-1.38,-0.19). The results are shown in Fig. 4-3. The ICC for each angle measurement is shown in Table 4-2.

4.2 Study II

In Study II, three models were created to study the association between hip dysplasia, gender, and morphology of the hip. The three models consisted of a combined pelvis and femur model shown in Fig. 4-4, and a left and right hip model shown in respectively Fig. 4-5 and Fig. 4-6. Each model is visualized as the mean model and the four most significant modes deformed by three standard deviations. The colors indicate the relative point displacement for the mode.

4.2.1 Gender differentiation

The discriminating direction determined by regularized logistic regression model for gender is visualized in Fig. 4-7. The model is based on 28 modes which explain 95% of the total variance in the model. The model

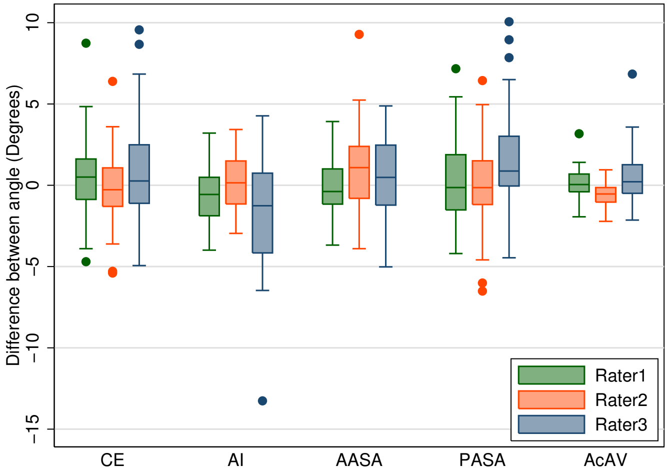

(a)

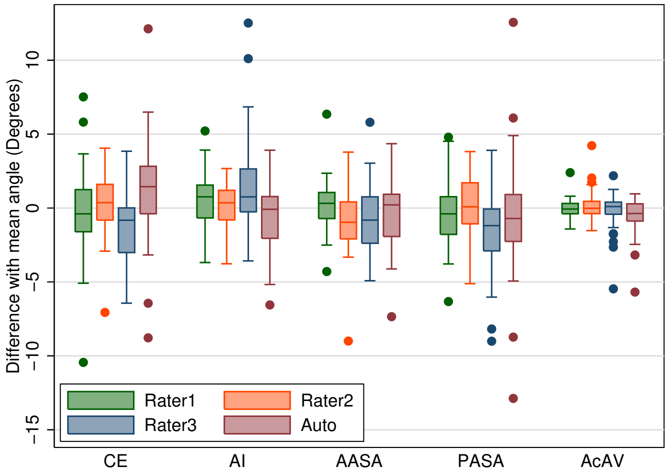

(b)

Figure 4-2: Comparison between angle measurements. In (a) the difference between repeated angle measurements for manual raters is shown. In (b) the difference between the mean angle measurement and each of the raters and the automatic method is shown.

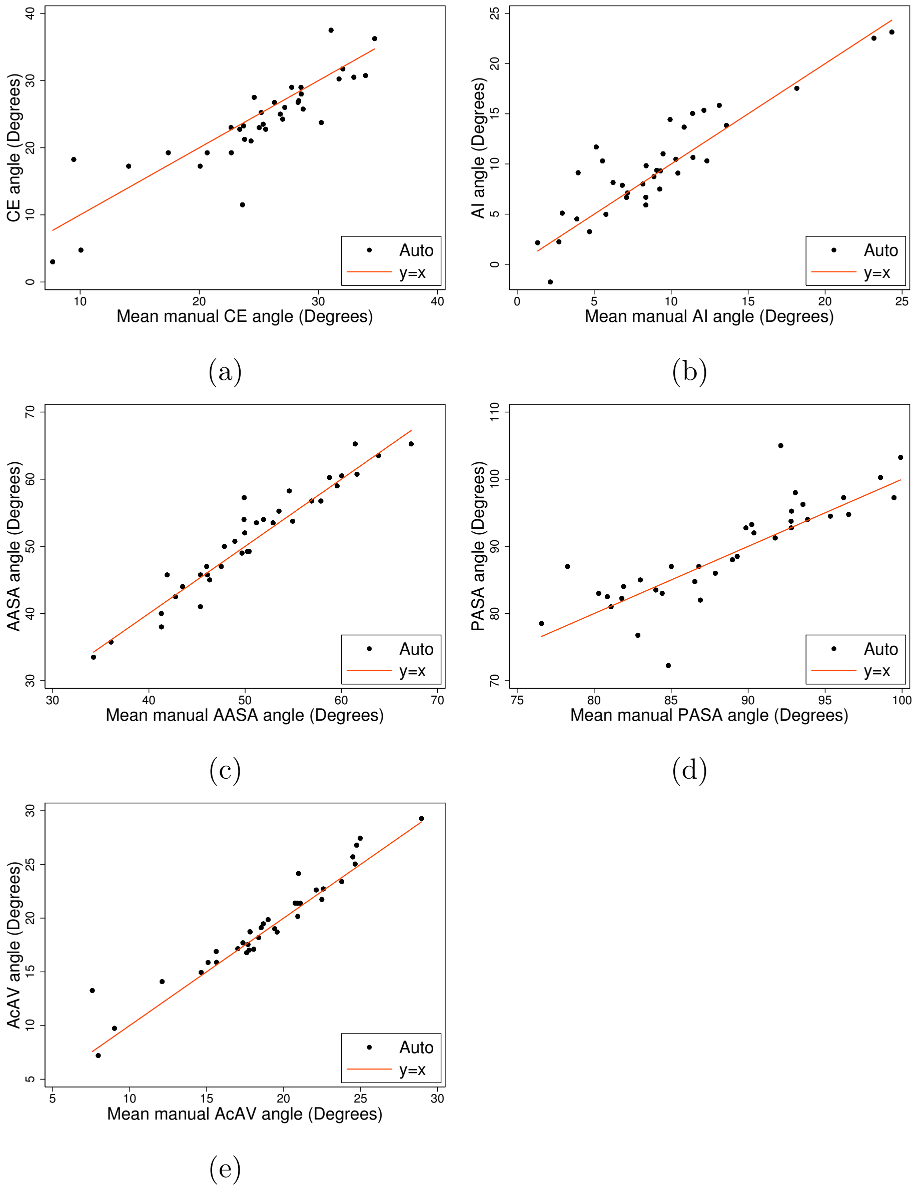

Figure 4-3: Scatter plots of mean manual angle measurement and the automatic method are shown for the center-edge (CE), acetabular index (AI), anterior-sector (AASA), posterior-sector (PASA), and acetabular anteversion (AcAV) angles.

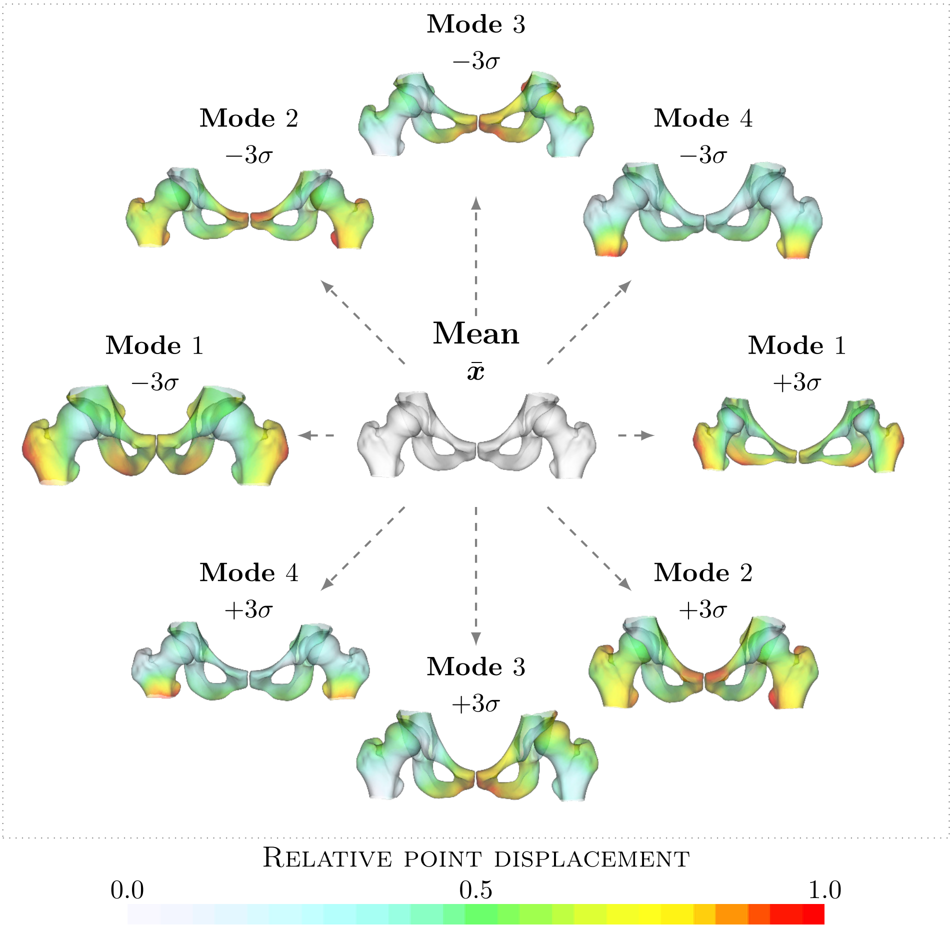

Figure 4-4: Visualization of the complete pelvis and femur model shown as the mean model and the four most significant modes of variation explaining 69% of the total variation in the model. Colors indicate the point displacement normalized by the maximum displacement for a mode.

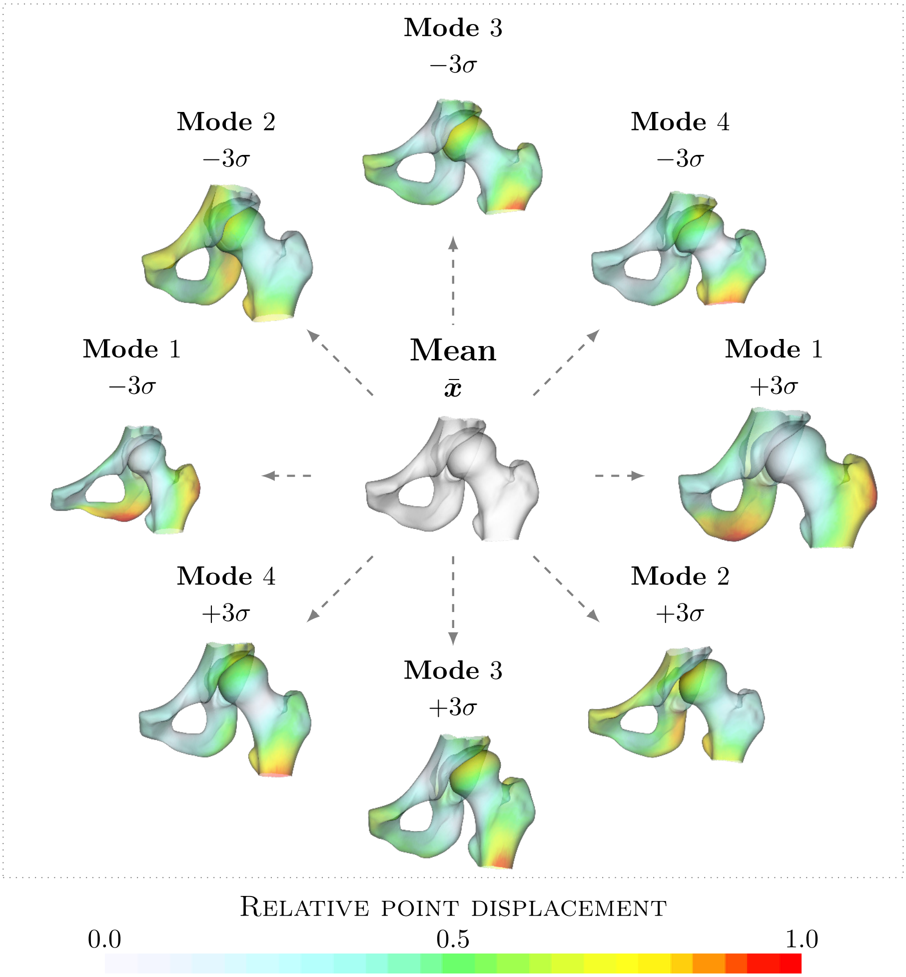

Figure 4-5: Visualization of the mean left pelvic bone and femur model and the four most significant modes explaining 67% of the total variation in the model. Each mode is shown as $\bar{\boldsymbol{x}} \pm 3$ standard deviations. Colors indicate the point displacement normalized by the maximum displacement for a mode.

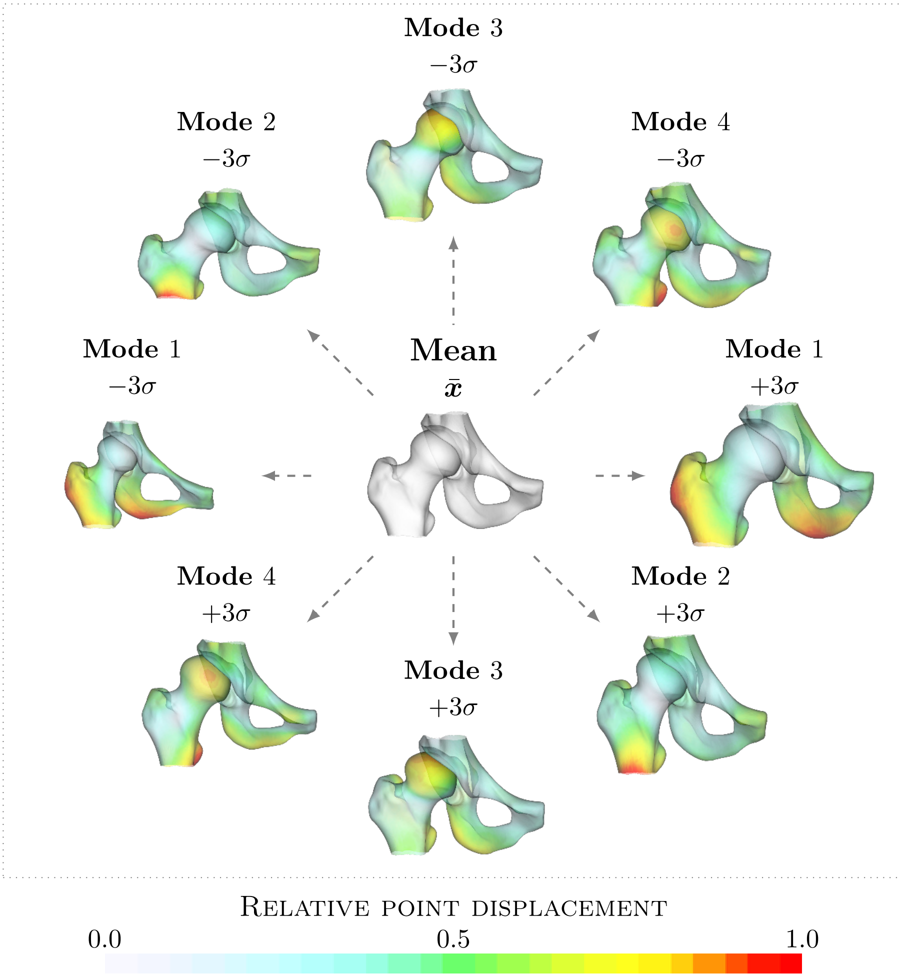

Figure 4-6: Visualization of the mean right pelvic bone and femur model and the four most significant modes explaining 66% of the total variation in the model. Each mode is shown as $\bar{\boldsymbol{x}} \pm 3$ standard deviations. Colors indicate the point displacement normalized by the maximum displacement for a mode.

is shown as 1% and 99% female with a blue and red overlay to highlight the differences in shape.

A clear difference is seen in the shape of the pubic arch. The male shape shows an acute angle, while females show a broad arch shape. In addition, a difference in size of the femurs is observed, with males having a slightly enlarged femur. The area under the curve for predicting gender based on the model was 0.99, demonstrating that the model could accurately predict gender in a leave-one-out cross-validation experiment.

4.2.2 Hip dysplasia

The discriminating direction determined by regularized logistic regression model for hip dysplasia for the left and right hip models is shown Fig. 4-8. The models are shown as 99%, 50%, and 1% dysplastic from a lateral and anterior view. A clear difference in acetabular coverage is apparent. In addition a difference in shape of the femoral head can be observed. The loss of congruency between the femur and acetabulum for the dysplastic hips is a result of the increased steepness of the acetabular roof and the loss of sphericity of the femoral head. This is especially visible in the anterior view of the left dysplastic model.

4.2.3 Diagnostic angle measurements

The association between different angle measurements and shape found by linear regression is shown in Fig. 4-9. Each angle measurement is shown including an overlay to highlight the difference in shape.

The morphological shape change associated with the center-edge angle is concentrated along the superiolateral edge of the acetabulum. With

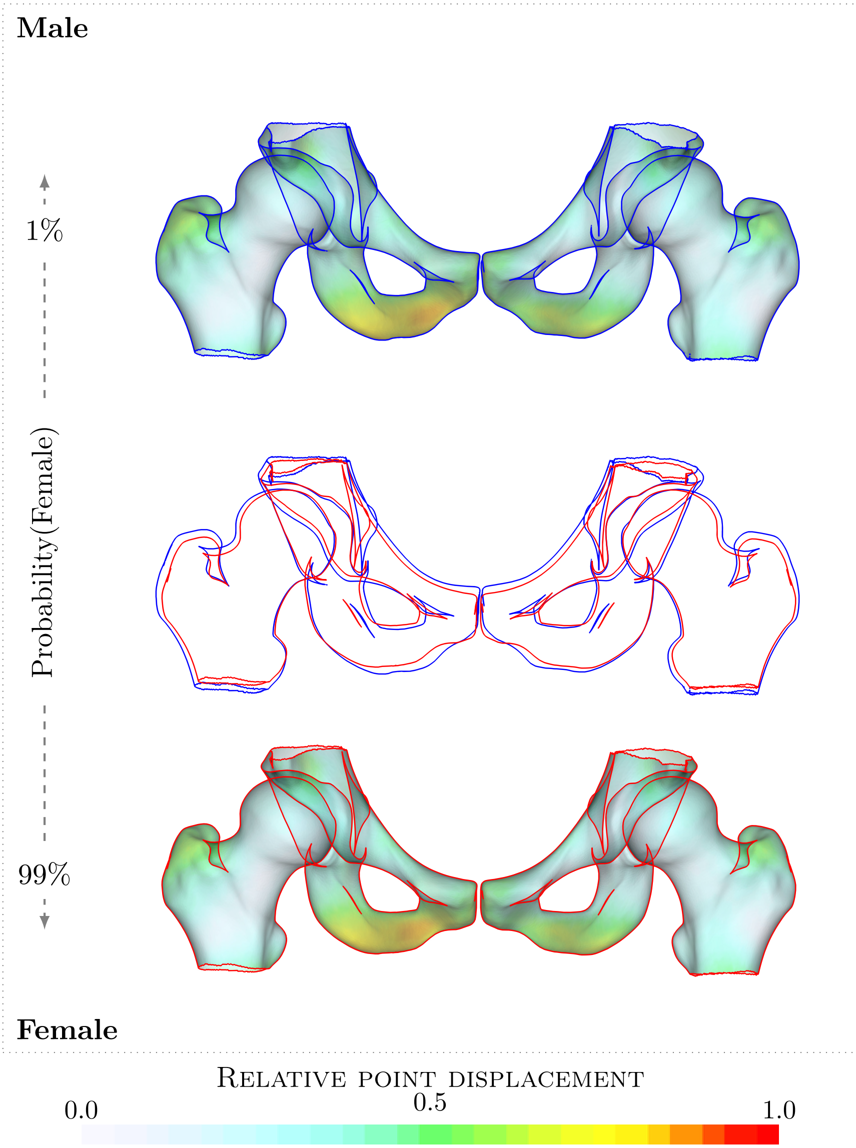

Figure 4-7: Visualization of the characteristic difference in shape between between males and females highlighted by blue and red overlays respectively. A clear difference in the shape of the pubic arch and size of the proximal femur is visible.

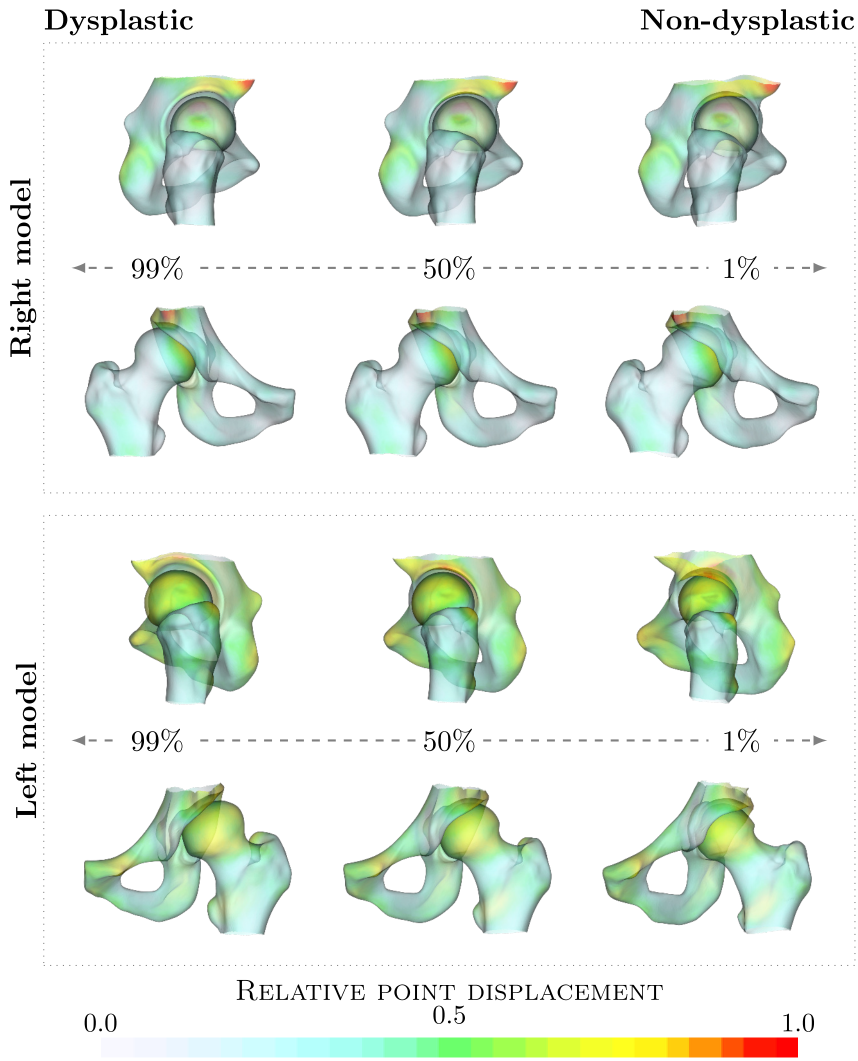

Figure 4-8: Visualization of difference between dysplastic and non-dysplastic hips as described by the discriminating direction found by logistic regression for the right (top) and left (bottom) models. For each model we show the lateral and anterior view. Colors indicate the point displacement normalized by the maximum displacement for a mode.

increasing center-edge angle, the coverage of the femoral head is increased. An increasing center-edge angle is also associated with a medial movement of the femoral head. Similarly, a decrease in acetabular index results in an increased coverage of the femoral head.

The acetabular anteversion angle is predominately determined by the movement of the anterior edge of the acetabulum. An increase of the acetabular anteversion angle results in a decrease in the anterior coverage. Conversely, decreasing acetabular anteversion results in the appearance of the cross-over sign, where the anterior and posterior edge of the acetabulum form a figure eight. In addition, the prominent iliac spine sign can be observed for decreasing acetabular anteversion. From the overlay, it is apparent that the anterior edge remains parallel, which suggests that the movement occurs simultaneously along the complete anterior edge and is not limited to the superior aspect of the acetabulum.

In Fig. 4-10, the results for predicting the angle measurements in leave-one-out experiments is shown. We find a good agreement between the actual and predicted values. The 95% confidence interval for the center-edge and acetabular index is approximately 10 degrees. For the acetabular anteversion angle, the 95% confidence interval is approximately 5 degrees.

4.3 Study III

4.3.1 Intra-operative angle measurements

A good agreement was found between the intra-operative angle measurements and manual measurements, with intraclass correlation coefficients ranging from 0.94 to 0.98. No statistically significant difference was found for the center-edge ($p=0.056$), acetabular index($p=0.212$), or the anterior

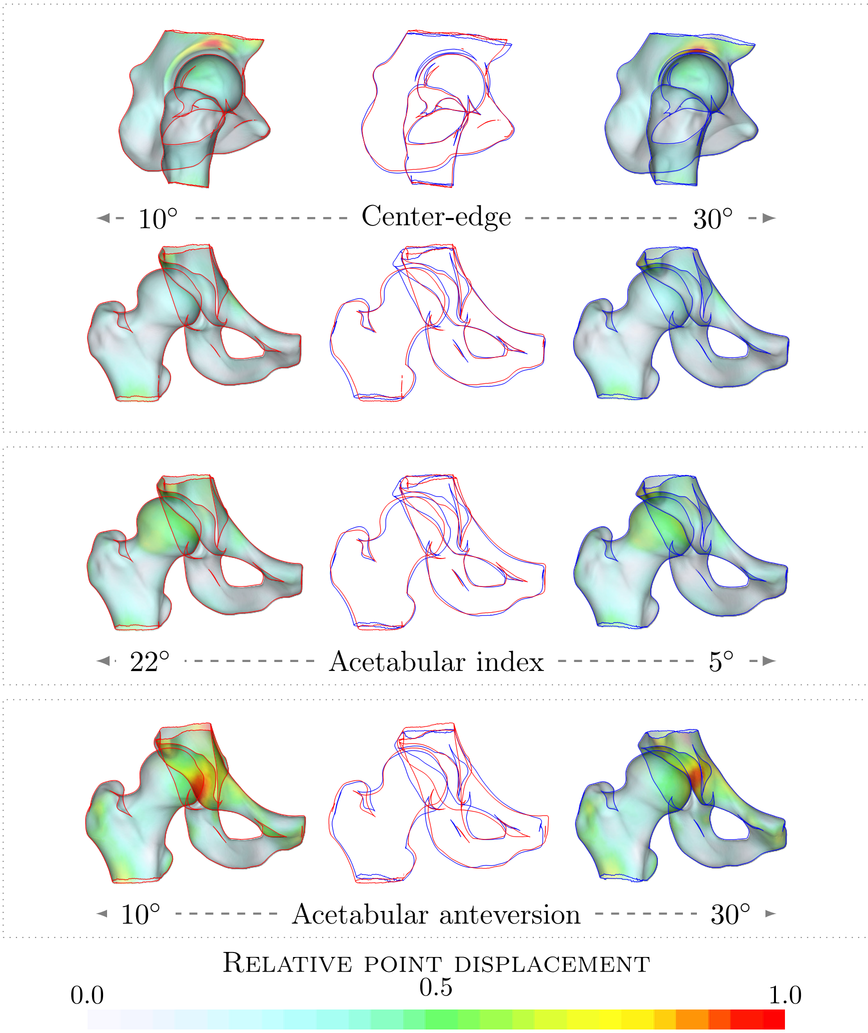

Figure 4-9: Visualization of the shape variation associated with the regression line found by linear regression to predict diagnostic angle measurements. Colors indicate the point displacement normalized by the maximum displacement for a mode.

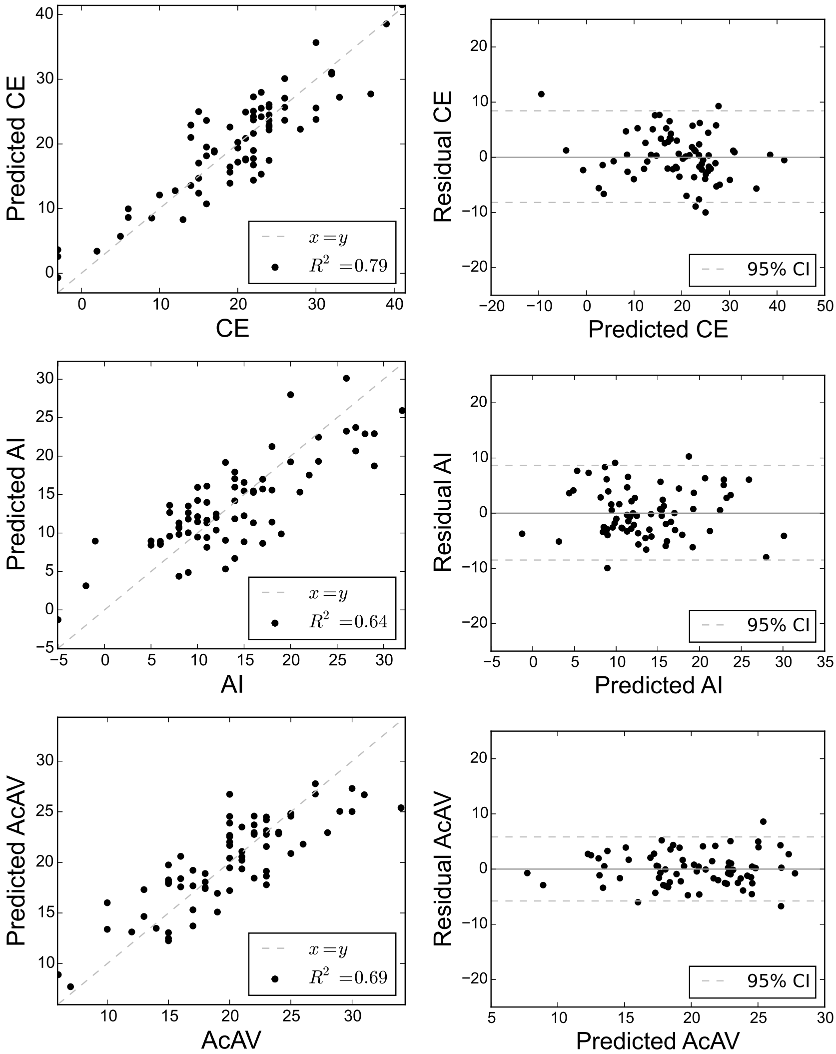

Figure 4-10: Linear regression results predicting angle measurements using the right hip model in leave-one-out experiments. Graphs of predicted values and residuals for center-edge (CE), acetabular index (AI), and acetabular anteversion (AcAV) angles are shown.

Table 4-3: Summary of result comparing between manual and BGS reported angle measurements. Significant differences indicated by ∗.

Angle	ICC	Avg. Diff.	SD	95 % CI		p-value
Center-edge	0.95	0.86	1.88	−0.03	1.74	0.056
Acetabular index	0.98	−0.44	1.54	−1.16	0.28	0.212
Posterior sector	0.94	1.65	1.91	0.75	2.53	0.001*
Anterior sector	0.98	−0.41	2.3	−1.51	0.71	0.452
Acetabular anteversion	0.95	1.24	1.65	0.44	2.03	0.004*

Table 4-4: Summary of result comparing repeated manual measurements. Significant differences indicated by ∗.

Angle	ICC	Avg. Diff.	SD	95 % CI		p-value
Center-edge	0.98	0.42	1.2	−0.14	0.98	0.137
Acetabular index	0.98	−0.14	1.31	−0.75	0.47	0.648
Posterior sector	0.95	0.15	2.07	−0.82	1.12	0.745
Anterior sector	0.99	−0.86	1.26	−1.44	−0.27	0.007*
Acetabular anteversion	0.98	0.01	1.28	−0.59	0.61	0.979

sector (p=0.452) angles. The posterior sector (−0.44°, p=0.001, 95% CI: 0.75, 2.53) and acetabular anteversion (1.24°, p=0.004, 95% CI:0.44, 2.03) angles. The results are summarized in Table 4-3. For comparison, the results for manual measurements are summarized in Table 4-4.

4.3.2 Post-operative peak-pressure

The post-operative peak pressure was decreased by 13% (95% CI: -22%, -4%) and was found to be significantly different (p=0.008). In one patient the post-operative peak-pressure was increased by 5%.

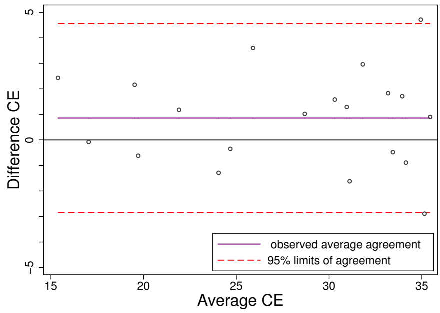

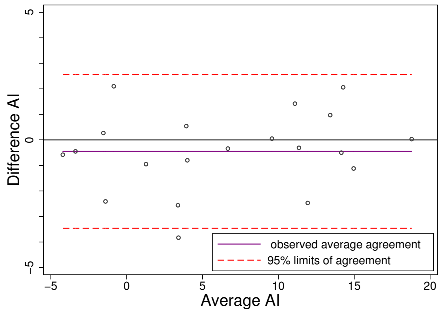

(a)

(b)

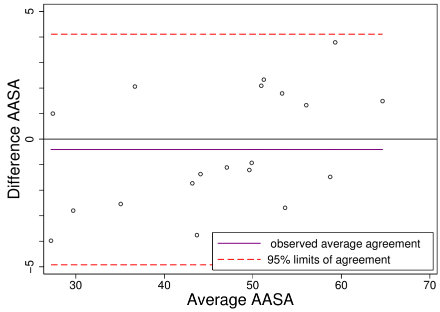

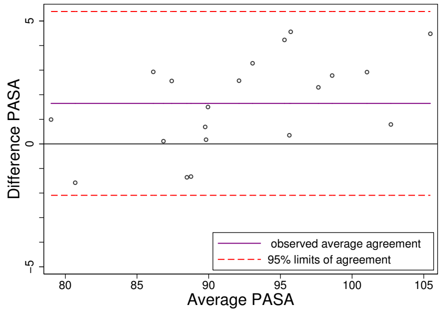

(c)

(d)

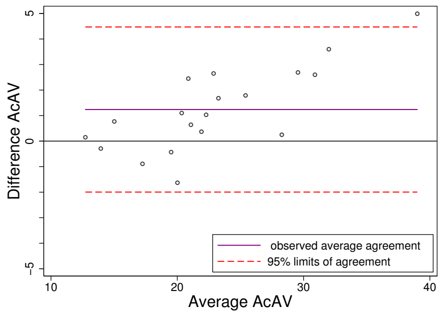

(e)

Figure 4-11: Bland-Altman plots comparing manual measurements to intra-operative computer navigation reported angle measurements for the center-edge (CE), acetabular index (AI), anterior-sector (AASA), posterior-sector (PASA), and acetabular anteversion (AcAV) angles.

5

Discussion

The overall aim of this thesis was to improve the use of the three dimensional information in the diagnosis and treatment of patients with hip dysplasia. Therefore, novel methods were developed to aid clinicians and improve the understanding of different aspects related to hip dysplasia. In the following sections the key findings are summarized and discussed in relation to existing literature. Subsequently the limitations of the studies in this thesis are discussed. Finally, future prospects and possible future research directions are presented.

5.1 Diagnosis and lunate segmentation

In Study I, a completely automated segmentation method for the identification of the lunate surface of the acetabulum was developed. The method uses graph cut segmentation to first identify the bones from CT images and subsequently identify the lunate surface. The lunate surface is segmented using a graph cut with a combined curvature and congruency measure that accurately identifies the lateral and medial edge of the lunate surface. The segmented lunate was subsequently used to automatically measure diagnostic angles commonly used in the diagnosis of hip dysplasia.

The automatic angle measurements were validated in experiments with three manual raters. The experiments investigated both the identification of the landmark points that are used to measure the diagnostic angles and the angle measurements. We found no difference between the automatic landmark detection and the manual raters. The mean distance to the landmarks ranged from 0.92 mm to 1.99 mm. The landmark with the largest mean distance was the medial landmark on the acetabular sourcil. This landmark is used to measure the acetabular index and can be difficult to accurately determine due to an unclear transition from the weight-bearing lunate surface to the acetabular fossa. The validation of the angle measurements found that the automatic method performed similarly to experienced raters and we found an excellent intraclass correlation coefficient for all angle measurements.

No previous work has segmented the lunate surface automatically. However, some work has been conducted on segmenting the outer rim of the acetabulum. In Tan et al.[104] a level-set approach was used to detect the acetabular rim. This method is similar to our approach, however the level-set evolution is an iterative approach and is not guaranteed to converge to the optimal edge. Subburaj et al.[101] used curvature features to identify different regions and landmarks of the pelvis. The acetabular rim was not detected, however as noted by Puls et al.[89] the technique may be suitable to perform automatic detection of the rim. In Puls et al.[89] an automatic method is presented based on an iterative procedure of projecting points from the surface to a plane and calculating a distance map. After processing of the distance map to remove unwanted points, a back-projection is performed to identify the points on the surface. A new plane is fitted to the found points and the procedure is repeated until convergence. A modified version with a different initialization was used in the work by Liu et al.[70]. Similar to the other previous approaches, this method is designed to find the acetabular rim and is not suitable for finding the medial edge of the lunate. Ehrhardt et al.[33] created a manually annotated model for both men and women and subsequently transformed it to a patient scan using image registration. The acetabular rim was then detected using ray-firing. Although not investigated, we note that this method may also be used to determine the lunate surface. The approach of using image registration to establish point correspondences is similar to the group-wise registration approach used in Study II.

The lunate trace method introduced by Armiger et al.[5] was developed for the manual delineation of the lunate surface. The method requires the manual placement of points along the lateral and medial edge of the lunate surface using reformatted images through the center of the femoral head. A similar method has been used in other studies, albeit mainly for the identification of the lateral edge[51,55,72,100,113]. The manual selection of the edge points is however a time consuming process and may suffer from problems with inter- and intra-rater variability similar to the variation seen in angle measurements observed in Study II and previous studies[15,34,65,110].

5.2 Morphology, gender, and hip dysplasia

In Study II, we developed a statistical shape model of the combined femur and acetabulum using CT volumes from symptomatic patients with hip pain, predominately due to hip dysplasia. The model was constructed using a group-wise image registration method to establish point correspondences between subjects, similar to the approach used by Seghers et al.[96]. To correct for pose differences of the femur, a pose correction procedure was developed that ensures that the relationship between the femoral head and acetabulum is maintained. The developed statistical shape model quantifies the variability of the morphology of the hip joint. In addition, we derived the relationship between the shape parameters and the coefficients obtained by regularized linear and logistic regression models. We demonstrated that the derived relationship can be used to visualize the variation associated with a particular dependent variable and can furthermore be used to predict gender and hip dysplasia as well as angle measurements.

No previous work has investigated the relationship between morphology and hip dysplasia with a combined statistical shape model of the pelvis and femur. However, Kainmueller et al.[57] developed a combined statistical shape model of the pelvis and proximal femur for segmentation of images. The method models the rotation and translation between the bones explicitly. They found that the resulting segmentation improved over using individual models. The method used is closely related to the approach introduced in Study II to remove the difference in pose of the femur. By including the variation in position of the femur, the SSM can model differences in pose to improve segmentations. However, to study the relationship between morphology and disease it is important to remove the variation. Harris et al.[45] investigated the difference in shape between patients with FAI with cam deformities and controls. They found that the mean FAI femur shape protruded above the mean control shape by a maximum of 3.3 mm[45]. Chan et al.[14] investigated the relationship between Legg-Calvé-Perthes and slipped capital femoral epiphysis.

An important finding in Study II, was the link between gender and the anteversion of the acetabulum. We found that the female acetabulum was more anteverted than the male acetabulum. This is in agreement with previous studies[16,49,50,102,105]. In males, the decreased anteversion resulted in the appearance of the cross-over sign, similar to that described by Reynolds et al.[90] on radiographs, associated with retroversion of the acetabulum. Since the cross-over sign is located in the cranial 30% of the joint, retroversion is sometimes thought to be a feature of the superior section of the acetabulum[37,109]. However, in the light of the findings presented in Study II, we believe that the cross-over sign is a result of the complete rotation of the acetabulum due to decreased anteversion and not a separate entity on its own. Although the complete rotation was noted by Reynolds et al.[90], the link between gender and acetabular anteversion was not clearly established.

Recognizing the association between gender and acetabular anteversion is important in the treatment of hip dysplasia. Specifically, in males with a retroverted acetabulum, a careful consideration of the amount of correction of the acetabular anteversion should be made. Over correcting the acetabular anteversion may result in abnormal posterior and anterior coverage. However, insufficient correction may lead to the development of risk of impingement. This is supported by previous findings that there is a risk of overcorrection and developing impingement after PAO[82,91,98].

5.3 Treatment and computer assisted PAO

In Study III, we performed a validation study of a computer aided surgery system for the intra-operative measurement of diagnostic angle measurements and joint pressure calculations during periacetabular osteotomy using a minimally invasive transsartorial approach. The system uses pre-operative CT derived bone models and lunate segmentation to determine angle measurements intra-operatively[5,6,78]. In addition, the peak-pressure is calculated using discrete element analysis based on the biomechanics of the hip joint[78,83].

We found a good agreement between manual measurements and the system reported angle measurements, indicating that the angle measurements may be used during surgery to reorient the fragment. In addition, we found that the peak-pressure was reduced after surgery according to the system as is the aim of performing reorientation[39,108]. This is in accordance with what others have found in computer simulations[118] and in previous studies using the same computer assisted surgery system[5,6].

The reduction in peak-pressure has also previously been verified by post-operatively determining the increase in load-bearing surface using stereology[77]. However, we found that the decrease in peak-pressure was less than in previous studies conducted by Armiger et al.[6]. We believe that since the mean pre-operative center-edge angle was larger in our study, the smaller reduction in peak-pressure may be attributed to the patients in our study being less dysplastic. A novel aspect of our study was the use of the computer assisted surgery system with a minimally invasive approach developed at our institute[108]. We found no difficulty when using the approach with the system. Due to an efficient intra-operative work-flow, the actual increase in surgical time was minimized. On average the use of the BGS system increased the surgical time by approximately 5 to 10 minutes.

Together, our findings in Study III, suggest that the use of a computer aided surgery system may be of clinical benefit. The system may be of particular value in patients with a complex dysplasia or for surgeons will less experience. The use of the computer assisted surgery system may help less experienced surgeons while using the minimally invasive approach. As it has been shown that this approach reduces trauma to the soft tissue, blood loss, and total surgery time, the wider adoption may be of clinical benefit to the patient[108]. Furthermore, convenient access to both radiological angle measurements and pressure distributions may help both less experienced and experienced surgeons achieve optimal corrections for each individual patient.

5.4 Limitations

In Study I, we developed and introduced a segmentation method to identify the lunate surface and perform automatic angle measurement aimed to improve the automatic angle measurements. Although the method performed better than previous methods, we continue to find a difference between manual measurements[22]. This difference may be attributed to limitations that warrant further discussion. The first aspect is that the identification of landmark points can be difficult, even for human raters, in cases where the landmark point is not distinct. In the absence of a true gold standard, the experienced radiologist is assumed to be the gold standard. However, as we found in Study I and in previous studies, the variation of even an experienced manual rater is not negligible[110]. However, the method may still be a valuable asset in the clinic since it can be used as a second opinion or to assist the radiologist in diagnosis.

In Study III, the manual lunate trace method was used to segment the lunate surface. Alternatively, the automatic lunate segmentation method developed in Study I could be used obtain the lunate surface. However, the development of the method had not been completed at the start of patient inclusion and therefore it was not part of the study.

In this thesis we have extensively made use of CT imaging to obtain the three dimensional information. However, due to the associated radiation dose of CT imaging, CT imaging is not performed on all patients. Therefore it would be of great interest to extend the methods introduced in this thesis to work without the need for CT imaging. This may be achieved in two ways: (1) the use of three dimensional imaging based on non-ionizing radiation such as MRI or (2) the reconstruction of the three dimensional anatomy from two dimensional projections. Investigation by MRI would offer clear advantages with respect to the ability to identify the cartilage layers of the joint and the labrum, but is less well suited for the analysis of bone morphology. In addition, MRI is not commonly used due to the higher cost, lesser availability, and lower spatial resolution. In recent years, the reconstruction of three dimensional bones from two dimensional projections has gained considerable attention[8,95,114,116,117]. The ability to obtain a three dimensional shape from two dimensional data is of great value in both computer aided diagnosis and surgery applications as used in Study I and Study III. A common approach is the use of statistical shape models, which are used to restrict the reconstructed shape to plausible variation described by the model[8,114,117]. The advantage of the use of x-ray radiographs is the significant reduction in radiation dose to the patient, while providing important three dimensional information. The reconstruction however presents new challenges, especially in cases with pathological changes[95,117]. When pathological changes are present, the used methods may not accurately reconstruct the corresponding deformity if it is not in the model. However, Zheng et al.[117] and Schumann et al.[95] found promising results that suggested that with further development, the methods may be of great value in the clinic.

There were also some limitations with respect to study design in the current thesis. Mainly, that the first two studies used a dataset of CT volumes established based on retrospective collection of CT data. The patients included underwent scanning due to hip symptoms, with the majority being diagnosed with hip dysplasia. In addition, patients had impingement and Legg-Calvé-Perthes diseases. The limitations introduced due to the retrospective study design include the possibility of selection bias. However, the prospective collection of a large database of hip scans is both time consuming, expensive, and presents ethical problems due to the associated radiation dose.

Another limitation with respect to the studied population is the generalizability to other ethnic groups. As ethnicity has been found to effect the incidence of hip dysplasia, it is unclear to what extent the findings of Study II may be generalized. Although information on the ethnicity of the included patients was not available, it can be assumed the ethnicity is predominately white Dane's. In a previous study of the link between ethnicity and hip dysplaisa, Inoue et al.[53] found that hip dysplasia was more common in Japanese women than in French men. In a subsequent study by Lavy et al.[67], it was found that British hips were less dysplastic than Japanese hips, and Malawain hips were less dysplastic than both. In a study of the Sami population of northern Norway, it was found the 38% had hip dysplasia to a certain degree[56].

5.5 General discussion

In the past decade, there has been a growing tendency to centralize the treatment of patients and create specialized units in larger hospitals. The rationalization is that centralizing the treatment allows the treatment by specialist surgeons with a higher volume of patients. This is supported by a number of studies that found worse outcome in lower volume hospitals and increased risk of revision surgery after total hip arthroplasty[7,31,66,84,106].

However, a recent nationwide study performed in Denmark by Kristensen et al.[61], found that higher volume hospitals had a higher 30-day mortality rate and lower quality of treatment after hip fracture. The authors speculate that in higher volume units, the more complicated surgeries may be prioritized over hip fracture patients, resulting poorer outcome. Due to the difficulty of PAO and since it is an elective surgery, this may not be an issue in the patients considered in this thesis. However, the lower standard of care, meaning that patients received less attention assessed by six recommended processes including systematic pain assessment and mobilization within 24 hours may be of concern. A consideration is if the increased volume results in decreased time per patient.

In order to maintain a high standard of care with less time per patient with the same amount of staff, an increased efficiency is required. The use of semi-automated and automated methods, such as were investigated in this thesis, may play an important role in the future in maintaining a high standard of care. By aiding the clinician during the diagnosis and treatment, the workflow can be optimized with the goal to maintain or improve the standard of care. In addition, the methods allow the personalization of the treatment, another important trend within the healthcare sector. This means that the treatment that all patients receive optimal care, which may result in a better outcome for patients.

A major motivation for performing PAO surgery is the normalization of the joint mechanics to delay the early development of osteoarthritis. Patients whom develop osteoarthritis are offered a total hip arthroplasty (THA). However, younger patients who receive a THA have a higher risk of revision surgery after primary THA[88]. Therefore it is clear that delaying the development of osteoarthritis is both beneficial for the patient and society and that methods to improve individual treatment are of great significance.

The gold standard diagnostic measurement for hip dysplasia is considered the center-edge angle introduced by Wiberg[115]. The indication for surgery is based on the threshold of 20° or 25° and systematic hip pain Troelsen et al.[108]. However, studies on predicting the long-term survival of the joint have found that other predictors are important in the prediction of early conversion to THA. An unanswered question of this thesis is if the lunate surface found in Study I or the developed statistical shape model from Study II may predict long term survival of the joint after PAO.

5.6 Future prospects

The graph cut segmentation technique developed in Study I requires the separate segmentation of the bones and the subsequent segmentation of the lunate surface. Due to the congruency of the femur and the acetabulum, an alternative method may attempt to segment the two surfaces in a single procedure. Optimal surface segmentation introduced by Li et al.[69] and later extended by Petersen et al.[87] may be a possible method that could identify the lunate surface in a single segmentation procedure.

The statistical shape model introduced in Study II, included both the femurs and the pelvic bones. In this study the pose of the femur was standardized to remove variation due to differences in femur positioning. In the future, the current model may be extended to an articulated shape model by including a relative transformation between the femur and acetabulum similar to the work of Kainmueller et al. [57]. However, it is unclear how the resulting model may be interpreted and further investigation is needed in the potential benefit.

The work of this thesis was undertaken in order to aid the clinicians. In particular the methods developed for both the manual and automatic analysis in Study I are of great interest to practicing radiologist. However, the use of medical software requires extensive validation as well as documentation of the process used to develop the software. Therefore, prior to introduction in the clinic, the current software would be required to be validated and approved for the use in the clinic. This is prohibitively expensive and is a major barrier for the introduction to the clinic. During the thesis we investigated if the segmentation method introduced in Study I could be patentable in collaboration with the Universities Technology Transfer Office. Although the method was found to be novel and patentable, a decision was made to not proceed due to limited market potential. To increase the market potential, the methods developed could be extended to be relevant for other diseases such as femoroacetabular impingement. In addition, the methods may be extended to other joints such as the knee or the shoulder. In the knee it may for example be of interest to study the changes due to laxity of the anterior cruciate ligament.

The studies of this thesis were based on the three aspects related to hip dysplasia: diagnosis, morphology, and treatment. Together the studies contribute to a better understanding of hip dysplasia. In future studies, the methods should be further developed to offer a streamlined workflow for the diagnosis and, if necessary, treatment of patients. Ideally, this system would ensure that patients are correctly diagnosed and receive the optimal treatment based on quantitative analysis.

6 Bibliography

[1] Agricola, R., Reijman, M., Bierma-Zeinstra, S., Verhaar, J. A. N., Weinans, H., and Waarsing, J. H. (2013). Total hip replacement but not clinical osteoarthritis can be predicted by the shape of the hip: a prospective cohort study (CHECK). *Osteoarthr. Cartil.*, 21(4):559–564.

[2] Anda, S., Terjesen, T., and Kvistad, K. A. (1991a). Computed tomography measurements of the acetabulum in adult dysplastic hips: Which level is appropriate? *Skeletal Radiol*, 20(4):267–271.

[3] Anda, S., Terjesen, T., Kvistad, K. A., and Svenningsen, S. (1991b). Acetabular angles and femoral anteversion in dysplastic hips in adults: CT investigation. *J Comput Assist Tomogr*, 15(1):115–120.

[4] Armand, M., Lepistö, J. V. S., Merkle, A. C., Tallroth, K., Liu, X.,

Taylor, R. H., and Wenz, J. (2004). Computer-aided orthopedic surgery with near-real-time biomechanical feedback. *Johns Hopkins APL Technical Digest (Applied Physics Laboratory)*, 25(3):242–252.

[5] Armiger, R. S., Armand, M., Lepisto, J., Minhas, D., Tallroth, K., Mears, S. C., Waites, M. D., and Taylor, R. H. (2007). Evaluation of a computerized measurement technique for joint alignment before and during periacetabular osteotomy. *Comput. Aided Surg.*, 12(4):215–224.

[6] Armiger, R. S., Armand, M., Tallroth, K., Lepisto, J., and Mears, S. C. (2009). Three-dimensional mechanical evaluation of joint contact pressure in 12 periacetabular osteotomy patients with 10-year follow-up. *Acta Orthop*, 80(2):155–161.

[7] Badawy, M., Badawy, M., Espehaug, B., Espehaug, B., Indrekvam, K., Indrekvam, K., Havelin, L. I., Havelin, L. I., Furnes, O., and Furnes, O. (2014). Higher revision risk for unicompartmental knee arthroplasty in low-volume hospitals. *Acta Orthop*, 85(4):342–347.

[8] Baka, N., Kaptein, B. L., de Bruijne, M., De Bruijne, M., van Walsum, T., Giphart, J. E., Niessen, W. J., and Lelieveldt, B. P. F. (2011). 2D-3D shape reconstruction of the distal femur from stereo X-ray imaging using statistical shape models. *Med Image Anal*, 15(6):840–850.

[9] Barr, R. J., Gregory, J. S., Gregory, J. S., Reid, D. M., Reid, D. M., Aspden, R. M., Aspden, R. M., Yoshida, K., Yoshida, K., Hosie, G., Hosie, G., Silman, A. J., Silman, A. J., Alesci, S., Alesci, S., Macfarlane, G. J., and Macfarlane, G. J. (2012). Predicting OA progression to total hip replacement: Can we do better than risk factors alone using active shape modelling as an imaging biomarker? *Rheumatology (Oxford)*, 51(3):562–570.

[10] Besl, P. J., McKay, N. D., and McKay, N. D. (1992). A method for registration of 3-D shapes. *IEEE Transactions on Pattern Analysis and Machine Intelligence*, 14(2):239–256.

[11] Bland, J. M., Altman, D. G., and Altman, D. G. (1986). Statistical methods for assessing agreement between two methods of clinical measurement. *Lancet*, 1(8476):307–310.

[12] Boykov, Y. and Funka-Lea, G. (2006). Graph Cuts and Efficient N-D Image Segmentation. *Int J Comput Vision*, 70(2):109–131.

[13] Boykov, Y. and Kolmogorov, V. (2004). An experimental comparison of min-cut/max-flow algorithms for energy minimization in vision. *IEEE Transactions on Pattern Analysis and Machine Intelligence*, 26(9):1124–1137.

[14] Chan, E. F., Farnsworth, C. L., Koziol, J. A., Hosalkar, H. S., and Sah, R. L. (2013). Statistical shape modeling of proximal femoral shape deformities in Legg–Calvé–Perthes disease and slipped capital femoral epiphysis. *Osteoarthritis and Cartilage*, 21(3):443–449.

[15] Clohisy, J. C., Carlisle, J. C., Trousdale, R., Kim, Y. J., Morgan, P., Steger-May, K., Schoenecker, P. L., and Millis, M. (2009). Radiographic evaluation of the hip has limited reliability. *Clin. Orthop. Relat. Res.*, 467(3):666–675.

[16] Cobb, J., Logishetty, K., Davda, K., and Iranpour, F. (2010). Cams and Pincer Impingement Are Distinct, Not Mixed: The Acetabular Pathomorphology of Femoroacetabular Impingement. *Clin. Orthop. Relat. Res.*, 468(8):2143–2151.

[17] Cooperman, D. (2013). What is the Evidence to Support Acetabular Dysplasia as a Cause of Osteoarthritis? *Journal of Pediatric Orthopaedics*, 33:S2–S7.

[18] Cooperman, D. R., Wallensten, R., and Stulberg, S. D. (1983). Acetabular dysplasia in the adult. *Clin. Orthop. Relat. Res.*, No. 175(175):79–85.

[19] Cootes, T. F., Taylor, C. J., Cooper, D. H., and Graham, J. (1995). Active Shape Models-Their Training and Application. *Computer Vision and Image Understanding*, 61(1):38–59.

[20] Cremers, D., Rousson, M., and Deriche, R. (2007). A review of statistical approaches to level set segmentation: Integrating color, texture, motion and shape. *Int J Comput Vision*, 72(2):195–215.

[21] De Raedt, S., Achterberg, H. C., Mechlenburg, I., Stilling, M., Rømer, L., Søballe, K., and de Bruijne, M. (2015a). Morphology of the dysplastic hip and the relationship with gender and acetabular version. *Submitted to PLoS One.*

[22] De Raedt, S., De Raedt, S., Mechlenburg, I., Mechlenburg, I., Stilling, M., Stilling, M., Rømer, L., Søballe, K., De Bruijne, M., and de Bruijne, M. (2013). Automated measurement of diagnostic angles for hip dysplasia. In *Proceedings of SPIE - The International Society for Optical Engineering.*

[23] De Raedt, S., Mechlenburg, I., Stilling, M., Rømer, L., Murphy, R. J., Armand, M., Lepisto, J., de Bruijne, M., de Bruijne, M., and Søballe, K. (2015b). Are computer reported measurements during periacetabular osteotomy using a minimally invasive approach reliable? *Submitted to Clinical Orthopedics and Related Research.*

[24] De Raedt, S., Mechlenburg, I., Stilling, M., Rømer, L., Søballe, K., and de Bruijne, M. (2015c). Lunate Extract: Fully automatic acetabular lunate segmentation and hip angle measurements. *Submitted to Medical Image Analysis*.

[25] Decker, S. J., Davy Jow, S. L., Ford, J. M., and Hilbelink, D. R. (2011). Virtual Determination of Sex: Metric and Nonmetric Traits of the Adult Pelvis from 3D Computed Tomography Models. *Journal of Forensic Sciences*, 56(5):1107–1114.

[26] Delaney, L. R. and Karmazyn, B. (2011). Developmental Dysplasia of the Hip: Background and the Utility of Ultrasound. *Seminars in Ultrasound, CT and MRI*, 32(2):151–156.

[27] Delaunay, S., Dussault, R. G., Kaplan, P. A., and Alford, B. A. (1997). Radiographic measurements of dysplastic adult hips. *Skeletal Radiol*, 26(2):75–81.

[28] Descoteaux, M., Audette, M., Chinzei, K., and Siddiqi, K. (2005). Bone enhancement filtering: application to sinus bone segmentation and simulation of pituitary surgery. In *MICCAI*, pages 9–16.

[29] Descoteaux, M., Audette, M., Chinzei, K., and Siddiqi, K. (2006). Bone enhancement filtering: Application to sinus bone segmentation and simulation of pituitary surgery. *Comput. Aided Surg.*, 11(5):247–255.

[30] Dimeglio, A. and Stanitski, C. L. (2001). Growth in pediatric orthopaedics. *Journal of Pediatric Orthopaedics*, 21(4):549–555.

[31] Doro, C., Dimick, J., Wainess, R., Upchurch, G., and Urquhart, A. (2006). Hospital volume and inpatient mortality outcomes of total hip

arthroplasty in the United States. *The Journal of Arthroplasty*, 21(6 Suppl 2):10–16.

[32] Ehrhardt, J., Handels, H., Malina, T., Strathmann, B., Plötz, W., and Pöppl, S. J. (2001). Atlas-based segmentation of bone structures to support the virtual planning of hip operations. *Int J Med Inform*, 64(2-3):439–447.

[33] Ehrhardt, J., Handels, H., Plötz, W., and Pöppl, S. J. (2004). Atlas-based recognition of anatomical structures and landmarks and the automatic computation of orthopedic parameters. *Methods Inf Med*, 43(4):391–397.

[34] Engesæter, I. Ø., Laborie, L. B., Lehmann, T. G., Sera, F., Fevang, J., Pedersen, D., Morcuende, J., Lie, S. A., Engesæter, L. B., and Rosendahl, K. (2012). Radiological findings for hip dysplasia at skeletal maturity. Validation of digital and manual measurement techniques. *Skeletal Radiol*, 41(7):775–785.

[35] Frangi, A. F., Niessen, W. J., Vincken, K. L., and Viergever, M. A. (1998). Multiscale vessel enhancement filtering. In *Lecture Notes in Computer Science*, pages 130–137, Berlin, Heidelberg. Springer Berlin Heidelberg.

[36] Fredensborg, N. and Fredensborg, N. (1976). The CE angle of normal hips. *Acta Orthop Scand*, 47(4):403–405.

[37] Fujii, M., Nakashima, Y., Yamamoto, T., Mawatari, T., Motomura, G., Matsushita, A., Matsuda, S., Jingushi, S., and Iwamoto, Y. (2010). Acetabular retroversion in developmental dysplasia of the hip. *J Bone Joint Surg Am*, 92(4):895–904.

[38] Gade, H. G. (1947). A Contribution to the Surgical Treatment of Osteoarthritis of the Hip-Joint. *Acta Orthop Scand*, 95(Suplementum 120).

[39] Ganz, R., Klaue, K., Vinh, T. S., and Mast, J. W. (1988). A new periacetabular osteotomy for the treatment of hip dysplasias. Technique and preliminary results. *Clin. Orthop. Relat. Res.*, (232):26–36.

[40] Ganz, R., Parvizi, J., Beck, M., Leunig, M., Nötzli, H., and Siebenrock, K. A. (2003). Femoroacetabular impingement: a cause for osteoarthritis of the hip. *Clin. Orthop. Relat. Res.*, (417):112–120.

[41] Gonzalez, R. C. and Woods, R. E. (2008). *Digital Image Processing.* Prentice Hall, New Jersey, third edition.

[42] Gosvig, K. K., Jacobsen, S., Sonne-Holm, S., Palm, H., and Troelsen, A. (2010). Prevalence of malformations of the hip joint and their relationship to sex, groin pain, and risk of osteoarthritis: a population-based survey. *J Bone Joint Surg Am*, 92(5):1162–1169.

[43] Gower, J. C. (1975). Generalized procrustes analysis. *Psychometrika*, 40(1):33–51.

[44] Gray, H. (1918). *Anatomy of the human body.* Lea & Febiger, Philadelphia.

[45] Harris, M. D., Datar, M., Whitaker, R. T., Jurrus, E. R., Peters, C. L., and Anderson, A. E. (2013). Statistical shape modeling of cam femoroacetabular impingement. *J. Orthop. Res.*, 31(10):1620–1626.

[46] Harris, W. H. (1986). Etiology of osteoarthritis of the hip. *Clin. Orthop. Relat. Res.*, No. 213:20–33.

[47] Hartig-Andreasen, C., Troelsen, A., Thillemann, T. M., and Søballe, K. (2012). What Factors Predict Failure 4 to 12 Years After Periacetabular Osteotomy? *Clin. Orthop. Relat. Res.*, 470(11):2978–2987.

[48] Heimann, T. and Meinzer, H.-P. (2009). Statistical shape models for 3D medical image segmentation: a review. *Med Image Anal*, 13(4):543–563.

[49] Hetsroni, I., Dela Torre, K., Duke, G., Lyman, S., and Kelly, B. T. (2013). Sex differences of hip morphology in young adults with hip pain and labral tears. *Arthroscopy*, 29(1):54–63.

[50] Hildebrand, F., Shin, H.-O., Flötotto, L., Krettek, C., and Gerich, T. (2012). The prevalence of reduced acetabular anteversion in asymptomatic patients: a retrospective analysis. *Z Orthop Unfall*, 150(6):601–606.

[51] Hipp, J. A., Sugano, N., Millis, M. B., and Murphy, S. B. (1999). Planning acetabular redirection osteotomies based on joint contact pressures. *Clin. Orthop. Relat. Res.*, (364):134–143.

[52] Hussell, J. G., Rodriguez, J. A., and Ganz, R. (1999). Technical complications of the Bernese periacetabular osteotomy. *Clin. Orthop. Relat. Res.*, (363):81–92.

[53] Inoue, K., Wicart, P., Kawasaki, T., Huang, J., Ushiyama, T., Hukuda, S., and Courpied, J. (2000). Prevalence of hip osteoarthritis and acetabular dysplasia in french and japanese adults. *Rheumatology (Oxford)*, 39(7):745–748.

[54] Jacobsen, S. (2006). Adult hip dysplasia and osteoarthritis. Studies in radiology and clinical epidemiology. *Acta orthopaedica. Supplementum*, 77(324):1–37.

[55] Janzen, D. L., Aippersbach, S. E., Munk, P. L., Sallomi, D. F., Garbuz, D., Werier, J., and Duncan, C. P. (1998). Three-dimensional CT measurement of adult acetabular dysplasia: Technique, preliminary results in normal subjects, and potential applications. *Skeletal Radiol*, 27(7):352–358.

[56] Johnsen, K., Johnsen, K., Goll, R., Goll, R., Reikerås, O., and Reikerås, O. (2008). Acetabular dysplasia in the Sami population: A population study among Sami in north Norway. *International Journal of Circumpolar Health*, 67(1):149–155.

[57] Kainmueller, D., Lamecker, H., Zachow, S., and Hege, H.-C. (2009). An articulated statistical shape model for accurate hip joint segmentation. *Conf Proc IEEE Eng Med Biol Soc*, 2009:6345–6351.

[58] Klaue, K., Durnin, C. W., and Ganz, R. (1991). The acetabular rim syndrome. A clinical presentation of dysplasia of the hip. *J Bone Joint Surg Br*, 73(3):423–429.

[59] Klaue, K., Wallin, A., and Ganz, R. (1988). CT evaluation of coverage and congruency of the hip prior to osteotomy. *Clin. Orthop. Relat. Res.*, (232):15–25.

[60] Krčah, M., Székely, G., and Blanc, R. (2011). Fully automatic and fast segmentation of the femur bone from 3D-CT images with no shape prior. In *ISBI*, pages 2087–2090.

[61] Kristensen, P. K., Kristensen, P. K., Thillemann, T. M., Thillemann, T. M., Johnsen, S. P., and Johnsen, S. P. (2014). Is bigger always better? A nationwide study of hip fracture unit volume, 30-day mortality, quality of in-hospital care, and length of hospital stay. *Med Care*, 52(12):1023–1029.

[62] Langlotz, F., Bächler, R., Bächler, R., Berlemann, U., Nolte, L. P., and Ganz, R. (1998). Computer assistance for pelvic osteotomies. *Clin. Orthop. Relat. Res.*, (354):92–102.

[63] Langlotz, F., Berlemann, U., Ganz, R., and Nolte, L. P. (2000). Computer-assisted periacetabular osteotomy. *Operative Techniques in Orthopaedics*, 10(1):14–19.

[64] Langlotz, F., Stucki, M., Stucki, M., Bächler, R., Bächler, R., Scheer, C., Scheer, C., Ganz, R., Berlemann, U., and Nolte, L. P. (1997). The first twelve cases of computer assisted periacetabular osteotomy. *Comput. Aided Surg.*, 2(6):317–326.

[65] Larson, A. N., Rabenhorst, B., De La Rocha, A., and Sucato, D. J. (2012). Limited Intraobserver and Interobserver Reliability for the Common Measures of Hip Joint Congruency Used in Dysplasia. *Clin. Orthop. Relat. Res.*, 470(5):1414–1420.

[66] Lavernia, C. J. and Guzman, J. F. (1995). Relationship of surgical volume to short-term mortality, morbidity, and hospital charges in arthroplasty. *The Journal of Arthroplasty*, 10(2):133–140.

[67] Lavy, C. B. D., Msamati, B. C., and Igbigbi, P. S. (2003). Racial and gender variations in adult hip morphology. *International Orthopaedics (SICOT)*, 27(6):331–333.

[68] Lepisto, J., Armand, M., and Armiger, R. S. (2008). Periacetabular osteotomy in adult hip dysplasia - developing a computer aided real-time biomechanical guiding system (BGS). *Suom Ortoped Traumatol*, 31(2):186–190.

[69] Li, K., Wu, X., Chen, D. Z., and Sonka, M. (2006). Optimal surface segmentation in volumetric images–a graph-theoretic approach. *IEEE*

Transactions on Pattern Analysis and Machine Intelligence, 28(1):119–134.

[70] Liu, L., Ecker, T., Schumann, S., Siebenrock, K., Nolte, L., and Zheng, G. (2014). Computer assisted planning and navigation of periacetabular osteotomy with range of motion optimization. In *Med Image Comput Comput Assist Interv*, pages 643–650.

[71] Lloyd-Roberts, G. C. (1955). OSTEOARTHRITIS OF THE HIP A Study of the Clinical Pathology. *J Bone Joint Surg Br*, 37-B(1):8–47.

[72] Lubovsky, O., Peleg, E., Joskowicz, L., Liebergall, M., and Khoury, A. (2010). Acetabular orientation variability and symmetry based on CT scans of adults. *Int J Comput Assist Radiol Surg*, 5(5):449–454.

[73] Mast, J. W., Brunner, R. L., and Zebrack, J. (2004). Recognizing Acetabular Version in the Radiographic Presentation of Hip Dysplasia. *Clin. Orthop. Relat. Res.*, (418):48–53.

[74] Mavcic, B., Pompe, B., Antolic, V., Daniel, M., Iglic, A., and Kralj-Iglic, V. (2002). Mathematical estimation of stress distribution in normal and dysplastic human hips. *J. Orthop. Res.*, 20(5):1025–1030.

[75] Mechlenburg, I., Hermansen, F., Thillemann, T., and Søballe, K. (2013). Blood perfusion and bone formation before and after minimally invasive periacetabular osteotomy analysed by Positron Emission Tomography combined with Computed Tomography. *International Orthopaedics (SICOT)*, 37(5):789–794.

[76] Mechlenburg, I., Kold, S., Rømer, L., and Søballe, K. (2007). Safe fixation with two acetabular screws after Ganz periacetabular osteotomy. *Acta Orthop*, 78(3):344–349.

[77] Mechlenburg, I., Nyengaard, J. R., and Søballe, K. (2004). Changes in load-bearing area after Ganz periacetabular osteotomy evaluated by multislice CT scanning and stereology. *Acta Orthop Scand*, 75(2):147–153.

[78] Murphy, R. J., Armiger, R. S., Lepisto, J., Mears, S. C., Taylor, R. H., and Armand, M. (2014). Development of a biomechanical guidance system for periacetabular osteotomy. *Int J Comput Assist Radiol Surg*, pages 1–12.

[79] Murphy, S. B., Ganz, R., and Müller, M. E. (1995). The prognosis in untreated dysplasia of the hip. A study of radiographic factors that predict the outcome. *The Journal of Bone & Joint Surgery*, 77(7):985–989.

[80] Murphy, S. B., Kijewski, P. K., Millis, M. B., and Harless, A. (1990). Acetabular dysplasia in the adolescent and young adult. *Clin. Orthop. Relat. Res.*, (261):214–223.

[81] Murray, R. O. (1965). The aetiology of primary osteoarthritis of the hip. *Br J Radiol*, 38(455):810–824.

[82] Myers, S. R., Eijer, H., and Ganz, R. (1999). Anterior femoroacetabular impingement after periacetabular osteotomy. *Clin. Orthop. Relat. Res.*, (363):93–99.

[83] Niknafs, N., Niknafs, N., Murphy, R. J., Armiger, R. S., Lepisto, J., and Armand, M. (2013). Biomechanical factors in planning of periacetabular osteotomy. *Front Bioeng Biotechnol*, 1:20.

[84] Ogura, K., Yasunaga, H., Horiguchi, H., Ohe, K., Shinoda, Y., Tanaka, S., and Kawano, H. (2013). Impact of hospital volume on postoperative complications and in-hospital mortality after musculoskeletal

tumor surgery: analysis of a national administrative database. *J Bone Joint Surg Am*, 95(18):1684–1691.

[85] Oransky, I. (2004). Sir Godfrey N Hounsfield. *The Lancet*, 364(9439):1032.

[86] Peters, C. L., Erickson, J. A., and Hines, J. L. (2006). Early results of the Bernese periacetabular osteotomy: The learning curve at an Academic Medical Center. *J Bone Joint Surg Am*, 88(9):1920–1926.

[87] Petersen, J., Nielsen, M., Lo, P., Nordenmark, L. H., Pedersen, J. H., Wille, M. M. W., Dirksen, A., and de Bruijne, M. (2014). Optimal surface segmentation using flow lines to quantify airway abnormalities in chronic obstructive pulmonary disease. *Med Image Anal*, 18(3):531–541.

[88] Prokopetz, J. J., Prokopetz, J. J., Losina, E., Losina, E., Bliss, R. L., Bliss, R. L., Wright, J., Wright, J., Baron, J. A., Baron, J. A., Katz, J. N., and Katz, J. N. (2012). Risk factors for revision of primary total hip arthroplasty: A systematic review. *BMC Musculoskelet Disord*, 13(1):251.

[89] Puls, M., Ecker, T. M., Steppacher, S. D., Tannast, M., Siebenrock, K. A., and Kowal, J. H. (2011). Automated detection of the osseous acetabular rim using three-dimensional models of the pelvis. *Comput. Biol. Med.*, 41(5):285–291.

[90] Reynolds, D., Lucas, J., and Klaue, K. (1999). Retroversion of the acetabulum. A cause of hip pain. *J Bone Joint Surg Br*, 81(2):281–288.

[91] Sampson, T. G. (2005). Hip morphology and its relationship to pathology: Dyplasia to impingement. *Operative Techniques in Sports Medicine*, 13(1):37–45.

[92] Sarkalkan, N., Weinans, H., and Zadpoor, A. A. (2014). Statistical shape and appearance models of bones. *Bone*, 60:129–140.

[93] Sato, Y., Nakajima, S., Shiraga, N., Atsumi, H., Yoshida, S., Koller, T., Gerig, G., and Kikinis, R. (1998). Three-dimensional multi-scale line filter for segmentation and visualization of curvilinear structures in medical images. *Med Image Anal*, 2(2):143–168.

[94] Schramm, M., Hohmann, D., Radespiel-Troger, M., and Pitto, R. P. (2003). Treatment of the dysplastic acetabulum with wagner spherical osteotomy: A study of patients followed for a minimum of twenty years. *J Bone Joint Surg Am*, 85(5):808–814.

[95] Schumann, S., Tannast, M., Nolte, L.-P., and Zheng, G. (2010). Validation of statistical shape model based reconstruction of the proximal femur—A morphology study. *Medical Engineering & Physics*, 32(6):638–644.

[96] Seghers, D., D'Agostino, E., Maes, F., Vandermeulen, D., and Suetens, P. (2004). Construction of a brain template from MR images using state-of-the-art registration and segmentation techniques. *Lecture Notes in Computer Science*, 3216(PART 1):696–703.

[97] Sharp, I. K. (1961). ACETABULAR DYSPLASIA The Acetabular Angle. *J Bone Joint Surg Br*, 43-B(2):268–272.

[98] Søballe, K. (2003). Pelvic osteotomy for acetabular dysplasia. *Acta Orthop Scand*, 74(2):117–118.

[99] Steel, H. H. (1973). Triple osteotomy of the innominate bone. *J Bone Joint Surg Am*, 55(2):343–350.

[100] Steppacher, S. D., Steppacher, S. D., Lerch, T. D., Gharanizadeh, K., Liechti, E. F., Werlen, S. F., Puls, M., Tannast, M., and Siebenrock, K. A. (2014). Size and shape of the lunate surface in different types of pincer impingement: theoretical implications for surgical therapy. *Osteoarthritis and Cartilage*, 22(7):951–958.

[101] Subburaj, K., Ravi, B., and Agarwal, M. G. (2008). 3D shape reasoning for identifying anatomical landmarks. *Computer-Aided Design and Applications*, 5(1-4):153–160.

[102] Tallroth, K. and Lepisto, J. (2006). Computed tomography measurement of acetabular dimensions: normal values for correction of dysplasia. *Acta Orthop*, 77(4):598–602.

[103] Tan, C. K. and Wong, W. C. (1990). Absence of the ligament of head of femur in the human hip joint. *Singapore Med J*, 31(4):360–363.

[104] Tan, S., Yao, J., Yao, L., Summers, R. M., and Ward, M. M. (2008). Acetabular rim and surface segmentation for hip surgery planning and dysplasia evaluation. In *Progress in Biomedical Optics and Imaging - Proceedings of SPIE.*

[105] Tannast, M., Pfannebecker, P., Schwab, J. M., Albers, C. E., Siebenrock, K. A., and Büchler, L. (2012). Pelvic morphology differs in rotation and obliquity between developmental dysplasia of the hip and retroversion. *Clin. Orthop. Relat. Res.*, 470(12):3297–3305.

[106] Taylor, H. D., Dennis, D. A., and Crane, H. S. (1997). Relationship between mortality rates and hospital patient volume for Medicare patients undergoing major orthopaedic surgery of the hip, knee, spine, and femur. *The Journal of Arthroplasty*, 12(3):235–242.

[107] Tönnis, D. (1987). *Congenital Dysplasia and Dislocation of the Hip in Children and Adults*. Springer Berlin Heidelberg, Berlin, Heidelberg.

[108] Troelsen, A., Elmengaard, B., and Søballe, K. (2008). A new minimally invasive transsartorial approach for periacetabular osteotomy. *J Bone Joint Surg Am*, 90(3):493–498.

[109] Troelsen, A., Rømer, L., Jacobsen, S., Ladelund, S., and Søballe, K. (2010a). Cranial acetabular retroversion is common in developmental dysplasia of the hip as assessed by the weight bearing position. *Acta Orthop*, 81(4):436–441.

[110] Troelsen, A., Rømer, L., Kring, S., Elmengaard, B., and Søballe, K. (2010b). Assessment of hip dysplasia and osteoarthritis: Variability of different methods. *Acta Radiol*, 51(2):187–193.

[111] Trousdale, R. T. and Cabanela, M. E. (2003). Lessons learned after more than 250 periacetabular osteotomies. *Acta Orthop Scand*, 74(2):119–126.

[112] Waarsing, J. H., Kloppenburg, M., Slagboom, P. E., Kroon, H. M., Houwing-Duistermaat, J. J., Weinans, H., and Meulenbelt, I. (2011). Osteoarthritis susceptibility genes influence the association between hip morphology and osteoarthritis. *Arthritis Rheum.*, 63(5):1349–1354.

[113] Wassilew, G. I., Heller, M. O., Diederichs, G., Janz, V., Wenzl, M., and Perka, C. (2012). Standardized AP radiographs do not provide reliable diagnostic measures for the assessment of acetabular retroversion. *J. Orthop. Res.*, 30(9):1369–1376.

[114] Whitmarsh, T., Humbert, L., De Craene, M., del Río Barquero, L. M., and Frangi, A. F. (2011). Reconstructing the 3D shape and bone

mineral density distribution of the proximal femur from dual-energy X-ray absorptiometry. *IEEE Trans Med Imaging*, 30(12):2101–2114.

[115] Wiberg, G. (1939). Studies on dysplastic acetabula and congenital subluxation of the hip joint. *Acta Orthop Scand*, 83(Supplementum 58).

[116] Zheng, G. (2011). Personalized X-ray reconstruction of the proximal femur via intensity-based non-rigid 2D-3D registration. In *MICCAI*, pages 598–606, Berlin, Heidelberg. Springer Berlin Heidelberg.

[117] Zheng, G., Gollmer, S., Schumann, S., Dong, X., Feilkas, T., and González Ballester, M. A. (2009). A 2D/3D correspondence building method for reconstruction of a patient-specific 3D bone surface model using point distribution models and calibrated X-ray images. *Med Image Anal*, 13(6):883–899.

[118] Zou, Z., Chávez-Arreola, A., Mandal, P., Board, T. N., and Alonso-Rasgado, T. (2013). Optimization of the position of the acetabulum in a ganz periacetabular osteotomy by finite element analysis. *J. Orthop. Res.*, 31(3):472–479.

Paper I

Diagnosis and lunate segmentation

Lunate Extract: Fully automatic acetabular lunate segmentation and hip angle measurements

Sepp De Raedt[a,b], Inger Mechlenburg[a,b], Maiken Stilling[a,c], Lone Rømer[d], Kjeld Søballe[c], Marleen de Bruijne[e,f]

[a]*Department of Clinical Medicine, Aarhus University, Aarhus, Denmark*
[b]*Orthopaedic Research Unit, Aarhus University Hospital, Aarhus, Denmark*
[c]*Deparment of Orthopaedics, Aarhus University Hospital, Aarhus, Denmark*
[d]*Department of Radiology, Aarhus University Hospital, Denmark*
[e]*Department of Computer Science, University of Copenhagen, Denmark*
[f]*Biomedical Imaging Group Rotterdam, Departments of Radiology and Medical Informatics, Erasmus MC Rotterdam, The Netherlands*

Abstract

For the diagnosis and pre-operative planning for patients with hip dysplasia, it is important to obtain an accurate segmentation of acetabular lunate surface. The acetabular lunate is the crescent shaped articulating surface of the hip, which determines the coverage of the femur. The coverage is insufficient in patients with hip dysplasia, often leading to pain and disability. The gold-standard diagnosis is based on manual angle measurement on CT and X-ray images. However, this is time consuming and requires a skilled radiologist.

In this work we present an automatic method which segments the acetabular lunate surface using a two-step process. The first step uses a graph cut based on a sheetness measure cost function to segment the bone boundary from the CT volumes. The second step uses a graph cut based on a combined curvature and congruency cost function to segment the acetabular lunate surface. Subsequently, five landmark points and corresponding diagnostic angle measurements are automatically derived from the lunate surface. The angle measurements quantify the lateral coverage, anterior coverage, posterior coverage, acetabular anteversion, and steepness of the acetabulum.

The method is validated against repeated manual measurements by three raters on a dataset of 18 patients (36 hips). We compare both the accuracy of identifying the landmarks and measuring angles to the manual measurements. We find a good agreement between the manual and the automatic measurements and believe that the method will be invaluable for diagnosis and pre-operative planning for computer assisted corrective surgery.

1. Introduction

The actebular lunate surface is the articulating surface of the hip joint and determines the coverage of the femoral head as shown in Figure 1. The relationship between the lunate surface of the acetabulum and the femoral head plays an important role in the diagnosis of various diseases of the hip such as hip dysplasia and femoroacetabular impingement. Research has shown that an abnormal relationship between the femur and acetabulum is associated with the early development of osteoarthritis and that corrective treatment may be essential to delay or halt the development of osteoarthritis (Harris, 1986; Hipp et al., 1999; Lloyd-Roberts, 1955; Wiberg, 1939; Tönnis and Heinecke, 1999; Agricola et al., 2013).

In patients with hip dysplasia the coverage of the femur by the acetabulum is insufficient and it is believed that this leads to increased peak-pressures resulting in pain and disability (Hipp et al., 1999; Sharp, 1961; Pompe et al., 2000). In clinical practice, the diagnosis is based on physical examination and angle measurements performed on plain radiographs or computed tomography images. Early work used manual measurements on radiographic films to quantify the lateral acetabular coverage by defining the center-edge (CE) angle of Wiberg (1939). The acetabular-index (AI) angle of Tönnis (1987) quantifies the steepness of the acetabular roof. These angles are measured with respect to the medial and lateral edge of the weight-bearing surface. However, due to over projection inherent to x-ray radiographs the edge points can be difficult to identify.

With the introduction of computed tomography (CT) imaging, the center-edge and acetabular-index can be measured on a coronal slice through the center of the femoral heads. In addition, the acetabular-anteversion (AcAV), posterior-sector (PASA), and anterior-sector (AASA) angles were defined by Anda et al. (1991) to quantify the anterior and posterior coverage. The five angle measurements are illustrated in Figure 1. Together, these angle measurements have become the gold standard for diagnosis of hip related diseases. However, manual measurements of angles are a time consuming task and previous studies have found large variation in inter- and intra-observer agreement(Clohisy et al., 2009; Troelsen et al., 2010; Larson et al., 2012). In order to accurately measure the angles automatically, it is necessary to segment the lunate surface.

Previous work on segmenting the lunate surface of the acetabulum is limited to manual and semiautomated methods.

Email address: `sepp.de.raedt@clin.au.dk` (Sepp De Raedt)

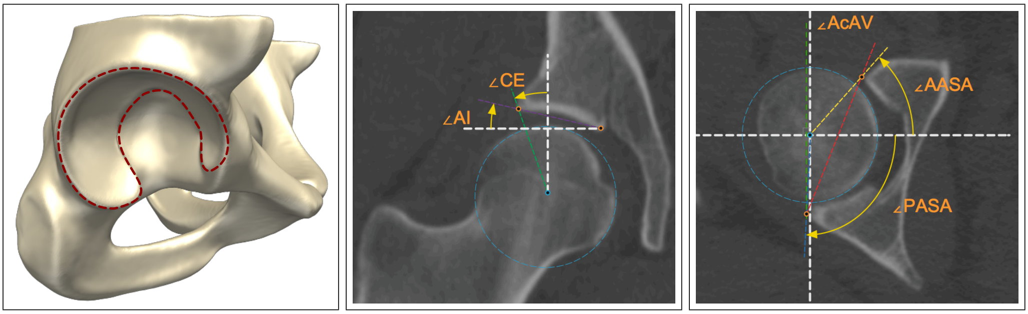

(a) (b) (c)

Figure 1: (a) Outline of the acetabular lunate surface. (b)) The center-edge (CE) and acetabular-index (AI) angle are measured in the coronal plane. (c) The acetabular-anteversion (AcAV), posterior-sector (PASA), and anterior-sector (AASA) angles are defined in the axial plane. The anatomical landmark points are indicated by circles.

Klaue et al. (1988) presented a manual method of outlining the contour of the acetabulum on CT slices to quantify the coverage. In later work, the cartilage zone of the acetabulum was defined by indicating the edges of the cartilaginous zone on each slice and fitting a sphere to the resulting points (Armand et al., 2004). Armiger et al. (2007) later introduced their method named Lunate trace. This method extracts a rectangular volume around the manually indicated center of the femoral head and subsequently the medial and lateral edge are manually delineated on radial slices. In a study by Wassilew et al. (2012) to determine the retroversion of the acetabulum, points were manually placed along the lateral edge of the acetabular rim. In Steppacher et al. (2014) the lunate surface was manually segmented from magnetic resonance imaging (MRI) arthrography.

Previous automatic methods have focused on segmenting only the lateral edge of acetabular rim (Puls et al., 2011; Tan et al., 2008). These methods aimed to determine the acetabular opening plane to measure the retroversion of the acetabulum. Puls et al. (2011) detect the rim by iteratively projecting points from the surface of the acetabulum to an initially placed plane and identifying the contour of the projected points. The contour points are then projected back to the surface and the plane is fit to the new points until the process converges (Puls et al., 2011). Tan et al. (2008) use a level set approach to find the rim of the acetabulum using a cost function based on curvature. These methods do not however guarantee to find the global optimum and do not find the medial edge of the lunate.

In De Raedt et al. (2013), we previously presented an automatic method using CT volumes for measuring diagnostic angles using sphere-fitting and ray-firing. The method first automatically segmented the femur and acetabulum and subsequently fit spheres to the femoral head and acetabular surface. The assumption of a spherical acetabular surface is however not always valid in the dysplastic hip and we found that the method had limited accuracy when finding the medial edge of lunate surface. In addition, this method did not identify the lunate surface which is of interest for the simulation of pressure distributions. This may for example be used in pre-operative planning and intra-operative surgical guidance systems (Armiger et al., 2009).

The method introduced in this paper introduces a two step procedure to segment the lunate surface from CT volumes. First, the pelvis and femur bones are segmented using a graph cut segmentation and each bone is identified. In the second step, the lunate surface is segmented from the pelvis mesh using a graph cut with different cost functions. We introduce three cost-functions based on the curvature, congruency, and combined measure and perform validation with manual measurements by three observers. The method makes no assumptions on the shape of the acetabulum and the graph cut optimization guarantees that the global optimum is found. Using the resulting surface, automatic angle measurements can be calculated.

2. Bone and lunate segmentation

In Section 2.1 we briefly summarize the common graph cut segmentation framework and notation which will subsequently be used to introduce the bone and lunate segmentation in Sections 2.2 and 2.3 respectively.

2.1. Graph cut

Graph cut based segmentation methods are widely applied in different domains and can be used to solve a wide variety of problems (Boykov and Kolmogorov, 2004). The method is based on the construction of a graph $\mathcal{G} =< \mathcal{V}, \mathcal{E} >$ with nodes $\mathcal{V}$ and edges $\mathcal{E}$ connecting neighboring nodes. In the current work, nodes represent either voxels in a volume or vertices of a mesh and the edges represent the connection between neighboring nodes. Two additional nodes are introduced, a terminal node S (source) and T (sink). The globally optimal segmentation can then be found by minimizing an energy function defined on the nodes:

$$E(A) = \sum_{p \in \mathcal{V}} R_p(A_p) + \lambda \sum_{(p,q) \in \mathcal{N}} B(p,q) \cdot \delta(A_p \neq A_q), \quad (1)$$

where the solution corresponds to the maximum flow/minimum cut for the flow from the source to the sink on the graph $\mathcal{G}$ which completely separates S from T (Boykov and Kolmogorov, 2004). The term $R(A)$ is a regional term, $B(A)$ is the boundary term and λ determines the importance of two terms with respect to each other. The regional term assigns a cost $R_p(A_p)$ for assigning label A_p to node p. The boundary term defines the penalty for assigning neighboring nodes p and q the labels A_p and A_q respectively. The term $\delta_{A_p \neq A_q}$ is 1 if $A_p \neq A_q$ and 0 otherwise. The energy function is minimized using the min-cut/max-flow algorithm (Boykov and Kolmogorov, 2004).

2.2. Bone segmentation

The segmentation method introduced in this section is a modified version of the method of Krčah et al. (2011) and used in our previous work (De Raedt et al., 2013). It incorporates improvements in the boundary term. The method consists of an initial graph cut using a sheetness based cost function to obtain a binary segmentation of the bones. Subsequently, connected component analysis is used to identify the individual bones. The different steps are shown in Figure 2.

2.2.1. Image pre-proccessing

To improve the contrast of edges, the input image is first filtered according to $I_e = I + k(I - I * G_s)$, where I is the input image, k is a scaling parameter determining the weight of the filtered image, and G_s and $*$ are a Gaussian kernel with variance s^2 and the convolution operator respectively.

2.2.2. Boundary term

The boundary term is commonly defined as a function of the difference in intensity values (Boykov and Kolmogorov, 2004; Krčah et al., 2011). However, this commonly fails in areas with low contrast, such as near bone boundaries with weak edges or if bones are in close proximity. Therefore it is necessary to include additional information. In previous work, second order information has been used to effectively segment blood vessels, bronchi, and the sinus bone (Sato et al., 1998; Descoteaux et al., 2006; Frangi et al., 1998). Krčah et al. (2011) introduced a sheetness measure to enhance the sheet-like structure of bone boundaries. Specifically, we require a high response for the sheet-like and tube-like structures of the bone surface and a low response for blob-like and noise-like structures. Given the eigenvalues and ordered by absolute magnitude such that $|\lambda_1| \leq |\lambda_2| \leq |\lambda_3|$, we introduce the following four ratios of eigenvalues:

$$R_{sheet} = \frac{|\lambda_2|}{|\lambda_3|} \tag{2}$$

$$R_{tube} = \frac{|\lambda_1|}{\sqrt{|\lambda_2||\lambda_3|}} \tag{3}$$

$$R_{blob} = (2|\lambda_3| - |\lambda_2| - |\lambda_1|)/|\lambda_3| \tag{4}$$

$$R_{noise} = (|\lambda_1| + |\lambda_2| + |\lambda_3|)/T, \tag{5}$$

where T is defined as the average of the sum of the absolute eigenvalues. The value of R_{sheet} and R_{tube} will be low for the corresponding structure and high when the structure is absent. In contrast with Krčah et al. (2011), we choose to take the square root of the denominator in R_{tube} to make the measure dimensionless and allow for unbiased scale selection. Furthermore, this ensures that the value is bounded when the second eigenvalue is small as noted by Frangi et al. (1998). In addition we include R_{blob} as defined by Descoteaux et al. which will be low for blob like structure (Descoteaux et al., 2006). Finally, the value of R_{noise} will be small for areas with little structure and small corresponding eigenvalues. The sheetness score $S(x)$ for a voxel x is defined as the product of these terms and is given by:

$$\begin{aligned} S(x) = \underset{\sigma\in\Sigma}{\operatorname{argmax}}\, S_\sigma(x) = -\, sgn(\lambda_3)\cdot& \\ &\left(\exp\left\{-\frac{R_{sheet}^2}{2\alpha^2}\right\}\right)\cdot \\ &\left(\exp\left\{-\frac{R_{tube}^2}{2\beta^2}\right\}\right)\cdot \\ &\left(1-\exp\left\{-\frac{R_{blob}^2}{2\eta^2}\right\}\right)\cdot \\ &\left(1-\exp\left\{-\frac{R_{noise}^2}{2\gamma^2}\right\}\right), \end{aligned} \tag{6}$$

where α, β, η, and γ are constant scaling parameters that control the sensitivity of the response. In order to increase the contrast near the bone boundary, we include the sign of the largest eigenvalue. By using a multi-scale approach, structures at different sizes can be detected. The maximum response for each voxel over all scales $\sigma \in \Sigma$ is used. The sheetness measure is discontinuous near the bone boundary and can therefore be used to define a cost function for the boundary term, as:

$$B(p,q) \propto \begin{cases} \exp\left\{-\frac{|S(p)-S(q)|}{\sigma_s}\right\}, & \text{for } S(p) \geq S(q), \\ 1, & \text{otherwise,} \end{cases} \tag{7}$$

where $S(p)$ and $S(q)$ are the sheetness score evaluated at voxel p and q respectively and σ_s is a constant scaling factor. Boykov and Funka-Lea (2006), show that using directed graphs with an asymmetric cost function allows for more accurate boundary segmentation. Specifically, this encourages the graph cut to favor transitions from high sheetness to low sheetness.

2.2.3. Regional term

The regional term $R_p(A_p)$ is used to initialize the segmentation by defining two regions that can be confidently considered to belong to bone or background. The region for bone can be found by thresholding the intensity values. However, the close proximity of bones in joints and possible partial volume may lead to the incorrect inclusion of voxels. By discarding voxels

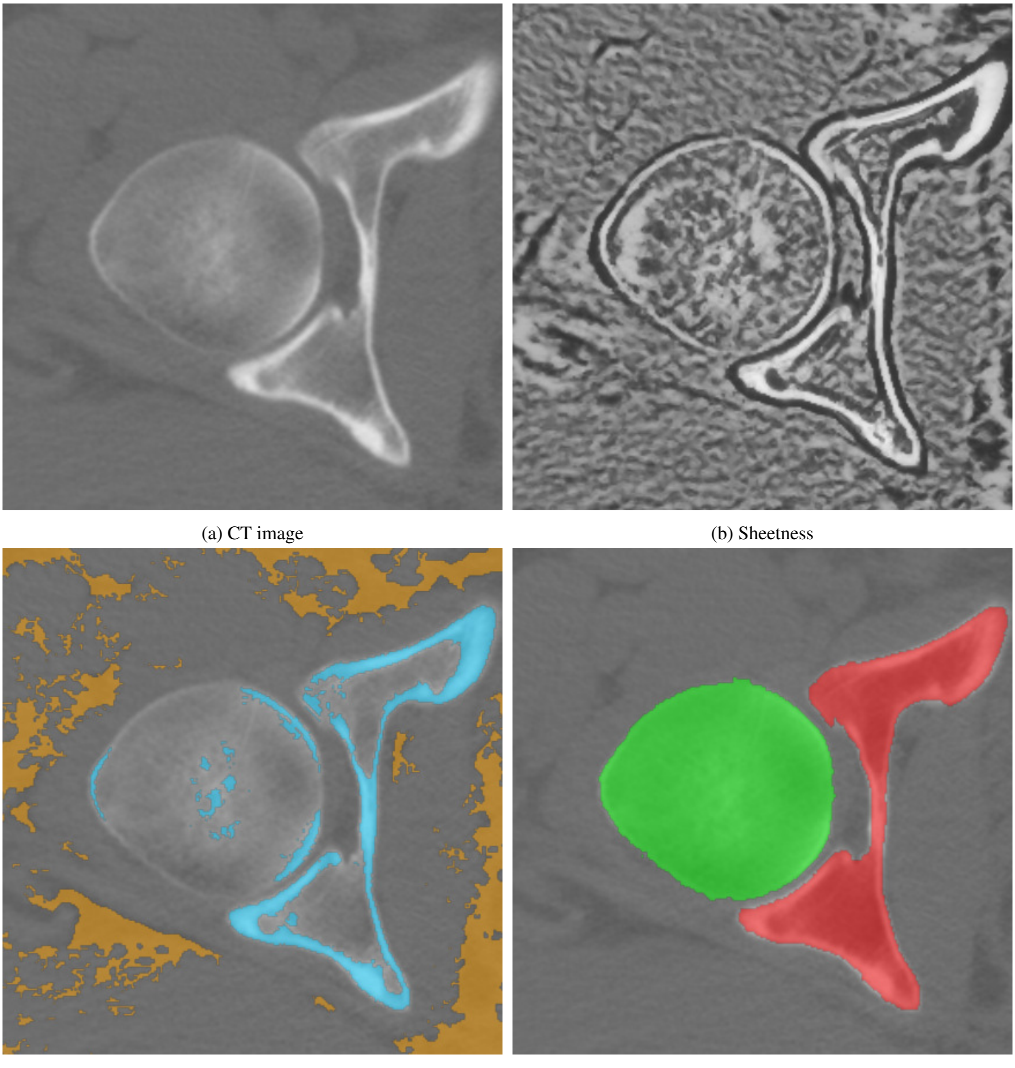

(a) CT image (b) Sheetness

(c) Initialization (d) Segmentation

Figure 2: The (a) input CT image is segmented by calculating (b) the sheetness measure in the boundary term and estimating (c) the initial regions for the regional term. Optimization of the graph cut results in (d) the final segmentation.

with a small response, this can be avoided. The background region is found by thresholding with a low value. We define the two regions as:

$$E_{bone} = x \in \Omega | \mathcal{I}(x) \geq 400HU \wedge S(x) > 0,$$
$$E_{bkg} = lcc(x \in \Omega | \mathcal{I}(x) < -50HU),$$

where lcc is the largest connected component of the thresholded input image. This ensures that low intensity voxels in trabecular bone are not included in the background. The regional term is then defined as:

$$R_p(A_p) \propto \begin{cases} 1, & \text{if } A_p = \text{"}Bone\text{" and } p \in E_{bkg}, \\ 1, & \text{if } A_p = \text{"}Bkg\text{" and } p \in E_{bone}, \\ 0, & \text{otherwise,} \end{cases}$$

where *Bone* and *Bkg* are the labels for bone and background respectively. This term penalizes a voxel that is assigned the label associated with the opposite region. No extra cost is introduced for voxels without an initial label.

2.2.4. Post-processing

To identify individual bones, a connected component analysis is applied to the resulting binary segmentation and each bone is assigned a unique label. Although the bones are correctly separated in most cases, post-processing of the resulting segmentation may be needed in cases where the bones are in close proximity and are not completely separated from each other. In these cases, the bones are assumed to be connected through a small number of voxels and can be separated by performing a second graph cut.

First, a morphological erosion is applied with a spherical element with radius R to the region C and the disconnected regions D and E are detected by connected component analysis, where $D, E \subset C$. If no disconnected regions are found, C is assumed to be a single bone. The goal is to find disjoint sets $D', E' \subset C$ such that $D' \cup E' = C$, $D \subset D'$, $E \subset E'$ where we would like to simultaneously minimize the number of voxels on the boundary between the two sets. These constraints can be incorporated by defining the following regional and boundary terms. The regional term is defined such that:

$$\forall p \in C : R_p(A_p) \propto \begin{cases} \infty, & \text{if } A_p = \text{"}D\text{" and } p \in E, \\ \infty, & \text{if } A_p = \text{"}E\text{" and } p \in D, \\ 0, & \text{otherwise.} \end{cases}$$

The boundary term is defined as a uniform cost such that $B(p, q) = B(q, p) = 1$. Minimizing Eq. 1 will result in a minimal number of voxels on the boundary between the two sets. If more than two regions are detected after the morphological erosion, the above procedure is repeated for each region. Finally, the bone surfaces can be extracted using the marching cubes algorithm (Lorensen and Cline, 1987).

2.3. Lunate segmentation

The procedure in the previous subsection results in two surfaces describing the pelvic bone and the femur for each hip. In the following section we introduce our method to segment the lunate surface from the obtained surface of the pelvic bone using a graph cut on the mesh. The motivation for our method is the knowledge that the edge of the lunate surface is characterized by high curvature and the articulating surface is congruent to the femur surface. We therefore propose to use a graph cut with boundary and regional terms based on the surface curvature and congruency of the surfaces. The input, resulting cost function, regional initialization, and resulting segmentation are shown in Figure 3.

2.3.1. Boundary term

Here we introduce three alternative boundary terms, to be used in identifying the lunate surface. The first two terms are based on the curvature and the congruency of the surfaces as explained below. In addition, we introduce a combined boundary term.

Surface curvature on a discrete mesh can be approximated by various methods (Surazhsky et al., 2003). Given the surface curvature κ, the curvature cost is defined as:

$$B_\kappa(p, q) \propto \begin{cases} \exp\left\{-\frac{\kappa(p)^2}{\sigma_\kappa^2}\right\}, & \text{for } \kappa(p) > \kappa(q), \\ 1, & \text{otherwise,} \end{cases} \tag{8}$$

where $\kappa(p)$ is the curvature at point p and σ_κ is a constant scaling value that regulates the curvature cost. We choose to use the maximum curvature for κ in the cost term, as we are interested in extracting the boundary along the line of maximal curvature. We use an asymmetric cost function to encourage cuts from high curvature to low curvature as in Equation 7.

The congruency between the pelvic bone and femur is quantified by a simple and intuitive congruency measure between the two surfaces. For each point on the surface of the mesh, the closest point on the adjacent surface is found and the congruency is then defined as the dot product of the surface normals i.e. $R_\theta = < N_p, N_q >$, where N_p and N_q are the normals of the points p and q. Subsequently, the congruency cost is defined as:

$$B_\theta(p, q) \propto \left(1 - \exp\left\{-\frac{(R_\theta(p) + \theta_c)^2}{\sigma_\theta^2}\right\}\right), \tag{9}$$

where σ_θ is a constant scaling value that regulates the congruency cost and θ_c is a constant that enables the shifting of the boundary. For values of $\theta_c \neq 0$, the maximum value of B_θ will be along the boundary where $R_\theta(p) = \theta_c$.

Finally, we introduce a combined cost defined as:

$$B_{combined}(p, q) \propto B_\kappa(p, q) \cdot B_\theta(p, q). \tag{10}$$

A surface plot of the combined cost function is shown in Figure. 4.

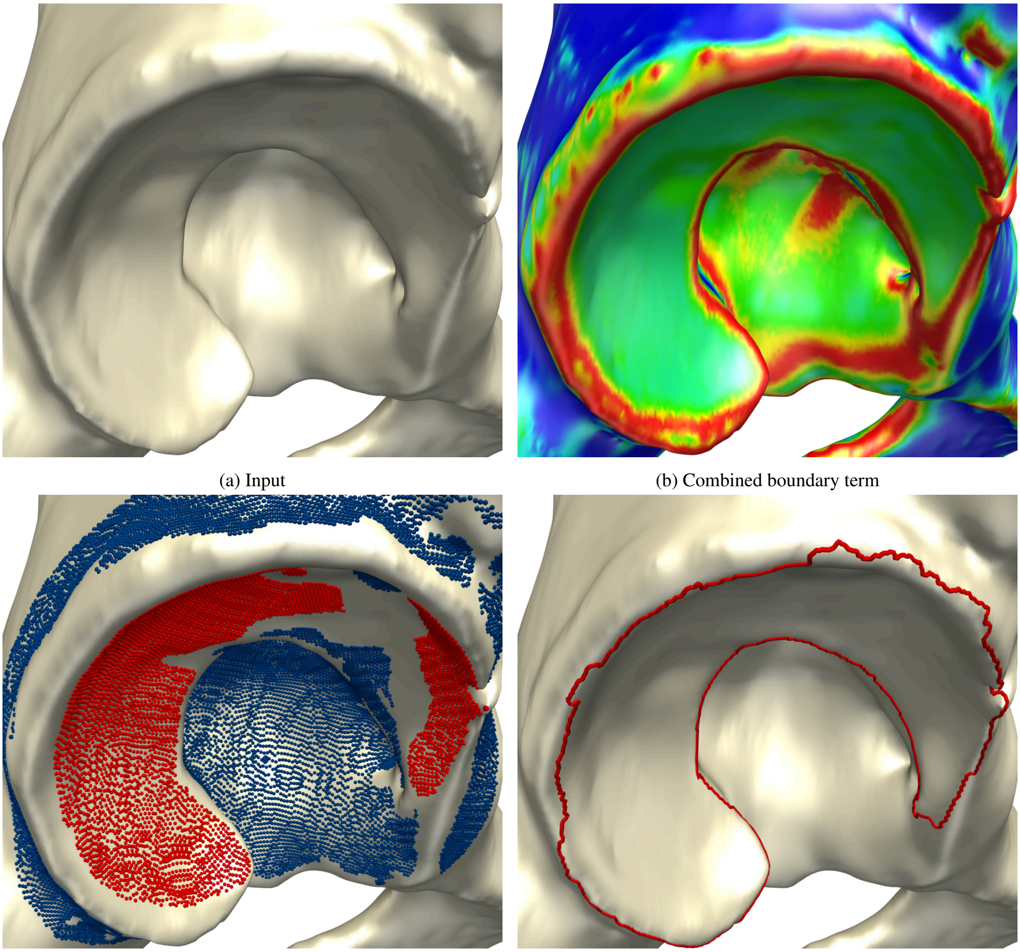

(a) Input

(b) Combined boundary term

(c) Regional term

(d) Segmentation

Figure 3: Lunate surface segmentation. (a) shows an example input surface. (b) shows the (undirected) combined boundary term visualized on the surface. Red regions introduce a low cost and blue high cost. In (c) the points defining E_{lunate} and E_{other} are shown in respectively red and blue. Note that some points on the lunate surface are incorrectly initialized, however the resulting segmentation is correct as shown in (d).

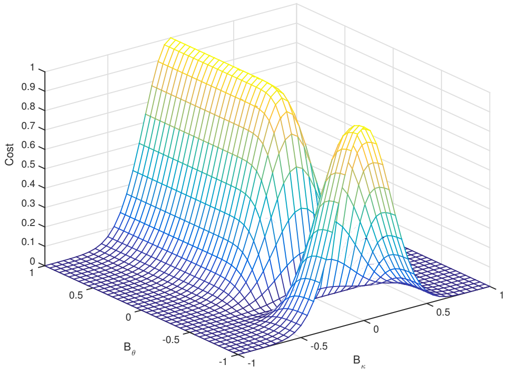

Figure 4: Surface plot of combined cost function for lunate extraction. The minimum for B_θ is displaced by an amount $\theta_c = 0.5$. The cost is lower for higher values of $|B_\kappa|$. The value of σ_κ and σ_c determine the steepness of the peak of the surface.

2.3.2. Regional term

The regional term defines two regions of the surface. The first region identifies points on the mesh $\mathcal{M}$, that can be confidently assumed to be part of the lunate surface. These points are located within a threshold distance from $d_{\min}$ the adjacent surface and have normals that have an angle of more than $\theta_{\min}$. The second region consists of points that are more than a threshold distance $d_{\max}$ from the adjacent surface and have low curvature. These conditions are stated as:

$$E_{lunate} = p \in \mathcal{M} | D(p) < d_{\min} \wedge R_\theta(p) > \theta_{\min}, \tag{11}$$

$$E_{other} = p \in \mathcal{M} | D(p) > d_{\max} \wedge R_\kappa(p) < \kappa_{\max}, \tag{12}$$

where $D(p)$ is the minimal distance to the adjacent surface for point p and the regional term is defined as:

$$R_p(A_p) \propto \begin{cases} 1, & \text{if } A_p = \text{"}lunate\text{" and } p \in E_{other}, \\ 1, & \text{if } A_p = \text{"}other\text{" and } p \in E_{lunate}, \\ 0, & \text{otherwise.} \end{cases}$$

The lunate surface is then found by minimizing Eq. 1 and extracting the corresponding surface.

3. Landmark detection and angle measurement

The diagnosis of hip dysplasia is based on angle measurements between anatomical landmark points. The points are identified on orthogonal slices through the center of the femoral heads. To compensate for patient positioning, the volume must be reformatted to align with the femoral heads. Subsequently the the lateral and medial edge of the sourcil can be identified in the coronal plane and the anterior and posterior points in the axial plane. Together with the center point of the femur, these points allow the calculation of the angle measurements described in the introduction and shown in Figure 1. Specifically, the center-edge, acetabular index, acetabular anteversion, anterior-actetabular sector, and posterior-acetabular sector angle.

For the validation of the automatic lunate extract method, we developed an application to manually identify the landmark points needed to calculate the angle measurements. The method and workflow are introduced in the following section. Subsequently, we present an automatic method based on the lunate segmentation.

3.1. Manual landmark placement

The manual measurement procedure was performed as a standardized workflow to aid reproducibility. The workflow consisted of three steps: (1) determining the center of the femoral heads, (2) automatically aligning the centers of the femoral heads, and (3) placing of the landmark points.

Raters placed a landmark approximately at the center point of the right femoral head. A sphere was then automatically placed at the indicated point with an initial radius of 25 mm. The outline of the sphere aids the rater in finding the center of the femoral head. The rater then adjusted the radius of the sphere and the placement of the center if necessary. The same process was repeated for the left femoral head. In cases where the femoral head is not perfectly spherical, the sphere is aligned as best as possible with the high intensity cortical bone of the femoral head.

The image was subsequently resampled such that the axial and coronal planes pass through both centers. If necessary the center points may be adjusted and the axis is recalculated. Once satisfied, the rater locked the image planes to prevent further changes.

The rater consecutively placed the lateral and medial points on the right and left hip in the coronal slice. Subsequently, the rater place the anterior and posterior points for the right and left hip in the axial slice.

3.2. Automatic landmark detection

To perform automatic landmark detection, the lunate segmentation from Sec. 2.3 was used. The center of the femur was detected by performing sphere fitting to the proximal femur as described in De Raedt et al. (2013). Briefly, first the points

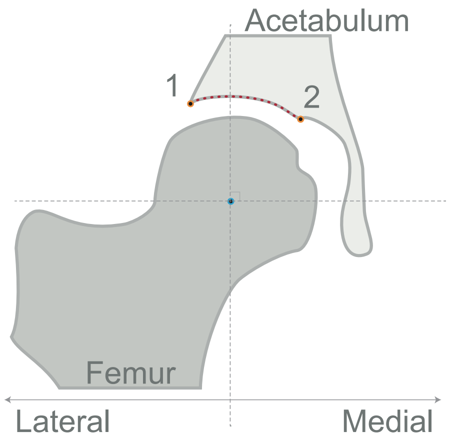

Figure 5: Illustration of the automatic landmark detection procedure. The red dotted line illustrates the segmented lunate surface. The green arrows indicate rays from the center of the femur that intersect the lunate surface. The ray is rotated until the medial edge is detected. The procedure is then repeated for the lateral, anterior, and posterior edges.

on the articulating surface of the femur are detected by finding points that are both within a threshold distance d_{th} to the acetabular surface and for which the angle between the corresponding normals is greater than γ_n. A sphere is fit to the detected points using the method of least squares.After the centers have been detected, the axis through the centers of the femoral head is calculated and the image is resampled. The anatomical landmarks are detected using the lunate surface mesh and an iterative ray-firing procedure. For each landmark, a ray is fired from the center point of the femur in the direction of the reference axis. The reference axis is defined for each angle measurement for which the angle would be equal to zero. If the ray intersects the lunate surface mesh, the ray is rotated around the axis perpendicular to the plane and a new ray is fired. This procedure is repeated until the ray no longer intersects the mesh. The final landmark position is the last intersection point. The procedure is illustrated in Figure 5.

4. Data

For the experiments we retrospectively collected preoperative CT volumes for patients who underwent investigative scanning after being referred to the department of radiology with hip related symptoms. Patient characteristics are shown in Table 1. In the following subsections we describe the data acquisition and parameter optimization procedure which will be used in the experiments outlined presented in the following section.

4.1. Scan acquisition

Patients were positioned according to a standard protocol with the patient in a supine position with their legs in a neutral position. Image slices were acquired from below the trochanter minor until above the acetabulum. Datasets were acquired on a Philips Mx8000, Philips Brilliance 40, or Philips Brilliance 64 (Philips Medical Systems, Best, The Netherlands) with a resolution of 768x768 pixels. Most scans were acquired with pixel spacing of 0.45 mm and the between slice spacing was 1.25 mm. For some scans, the pixel spacing ranged between 0.38 mm and 0.52 mm and the between slice spacing ranged between 1.25 mm and 1.6 mm. No ethical approval or informed consent were needed for a retrospective study in accordance with our institutional guidelines.

Table 1: Patient characteristics for patients that underwent CT investigation (N=96).

Parameter	Value
Age (Years)	
Median	36
Range	13 to 65
Sex	
Female	63 (67.7%)
Male	33 (34.3%)
Indication for CT investigation	
Dysplasia	73 (76%)
Impingement	7 (7.3%)
Legg-Calvé-Perthes	2 (2%)
Other	14 (14%)

4.2. Manual landmark annotation

Manual measurements on 18 patients (36 hips) were performed by three raters with at least one month between measurements using the method described in Sec. 3. Prior to the start of the study, the senior radiologist demonstrated the correct identification of the landmark points. Measurements were performed independently and blinded from previous measurements. The raters are in order of experience (1) a senior radiologist (LR), (2) a biomedical engineer (SDR), and (3) a radiologist in training (LS).

4.3. Lunate extract parameter optimization

Parameter optimization for the lunate extract method was performed using an independent training set with manual annotations by one rater (SDR). The optimized criteria was the sum of the squared distances between automatic and manual reference points. A grid-search was performed to find the parameters that minimized the criterium. A fixed penalty of 1000, was used when no intersection with the extracted lunate surface was found. Optimization of the parameters was performed on 23 patients. The values for $\theta_{\min}$ and $\kappa_{\max}$ were set to 160 and 0.15 respectively.

The optimized parameters are listed in Table 2. The combined cost function performed the best of the three proposed cost functions, followed by the curvature and congruency based cost functions respectively. As intended, the combined cost function ensures that in areas of low curvature, the graph cut follows the edge of the congruent surface. This is important due to the smooth transition on the anterior side of the lunate surface as seen in Figure 1(a).

5. Experiments and results

To evaluate the performance of the automatic lunate extract method, we evaluate both the landmark placement and resulting angle measurements. We compare the manual raters ability to repeat a measurement and the accuracy with which a landmark identified or angle measured. Differences between measurements were evaluated graphically and by analysis of variance (ANOVA). ANOVA results were corrected for multiple comparisons with Box's conservative epsilon. Significant differences between raters were determined with the Tukey HSD *post-hoc* test and are reported as mean differences, p-value, and 95% confidence intervals. Significance was set at $p \leq 0.05$. Non-normally data was log transformed before analysis. All analysis was performed with STATA 13 (StataCorp, College Station, USA).

5.1. Segmentation evaluation

Automatic segmentation was performed according to the method described in Sec. 2.2. Segmentation parameters were set to: $k = 10$, $s = 1$, $\lambda = 5$, $\alpha = \beta = \eta = \gamma = 0.5$, $\sigma_s = 0.2$, $\Sigma = [0.6, 0.8]$. Segmentation accuracy was visually verified and segmentation parameters were adjusted if necessary due to noise or artifacts. Five patients were excluded due to segmentation failure attributed to narrow joint space caused by joint degeneration. Segmentation failed due to streaking artifacts from the metal gonad shield in four patients. If possible, the region of interest was adjusted to exclude the metal and the segmentation was redone, resulting in satisfactory segmentations.

5.2. Landmark placement

To determine the accuracy of the landmark identification of both manual and the automatic method, we performed two sub-experiments. The first experiment aimed to quantify the raters ability to identify the same point on repeated readings. Therefore, the euclidean distance between the manual raters first and second measurement for a subject were determined for each landmark point. The results are shown in Figure 6(a). The distance to the mean landmark was non-normally distributed. Analysis found no difference between raters for the center (p=0.17), anterior (p=0.17), and posterior (p=0.9) landmark points. A statistically significant difference was found between rater 3 and both rater 1 (1.46, p=0.014, 95% CI:1.07,2.00) and rater 2 (1.55, p=0.004, 95% CI:1.14,2.13) for the lateral landmark point. For the medial point, a statistically significant difference was found between rater 3 and rater 2 (1.69, p=0.001, 95% CI:1.22,2.34).

The second experiment aimed to quantify automatic method and the raters ability to identify the correct landmark position. Therefore, the mean landmark (geometric average) for the raters first measurement of a subject was calculated for each landmark. In the absence of a true gold standard, the mean landmark is assumed to be the agreed upon correct landmark position. Subsequently, the distance between the mean landmark and the raters second measurement and the automatic method was calculated. In Figure 6(b), the distance to the mean landmark is shown for each rater and the automatic method. The distance to the mean landmark was non-normally distributed. Analysis found no difference between raters and the automatic method for the center (p=0.18), anterior (p=0.55), posterior (p=0.18), lateral (p=0.13), and medial (p=0.12) landmark points. In Table 3 we present the mean, standard deviation, minimum and maximum distance to the mean landmark point over all raters.

Table 3: Summary statistics for the distance (mm) to the mean landmark position for raters and the automatic method.

Landmark	Mean	SD	Min	Max
Center	0.92	0.58	0.17	3.58
Anterior	1.06	0.54	0.26	3.42
Posterior	1.41	0.99	0.12	5.91
Lateral	1.37	0.95	0.23	6.1
Medial	1.99	1.98	0.07	10.8

5.3. Angle measurement

To determine the accuracy of measuring the diagnostic angles, we performed two sub-experiments. The first experiment aimed to determine a raters ability to measure the same angle on repeated readings. The difference between raters first and second measurement were calculated and analyzed. The results are shown in Figure 7(a). Analysis found no statistically significant difference between raters for the difference in measurement of the CE (p=0.32), AASA (p=0.08), and PASA (p=0.09) angles. A statistically significant difference was found between rater 3 and rater 2 for both the AI (-1.8, p=0.004, 95% CI:-3.1,-0.49) and the AcAV (1.1, p=0.001, 95% CI:0.37,1.75) angle.

The second experiment aimed to measure the correct angle. The correct angle measurement was defined as the mean of the first measurement of the manual raters for a subject. Subsequently, the difference between the mean angle measurement and the raters second measurement and the automatic measurement were compared. The results are shown in Figure 7(b). Analysis found no statistically significant differences between raters and the automatic method for the AASA (p=0.1) and PASA (p=0.08) angles. For the CE angle, a statistically significant difference was found between the automatic method and rater 3 (2.44, p=0.001, 95% CI:0.84, 4.03). For the AI angle, a statistically significant difference was found between rater 3 and rater 2 (1.54, p=0.031, 95% CI:0.1,3.0) and the automatic method and rater 3 (-2.23, p=0.001, 95% CI:-3.68,-0.79). For the AcAV angle, a statistically significant difference was found between the automatic method and rater 2 (-0.78, p=0.004, 95% CI:-1.38,-0.19).

Finally, the intraclass correlation coefficient was calculated using a two-way random effects model. Here we assume that the subjects are randomly selected from the population and are rated by the same k raters, including the automatic method,

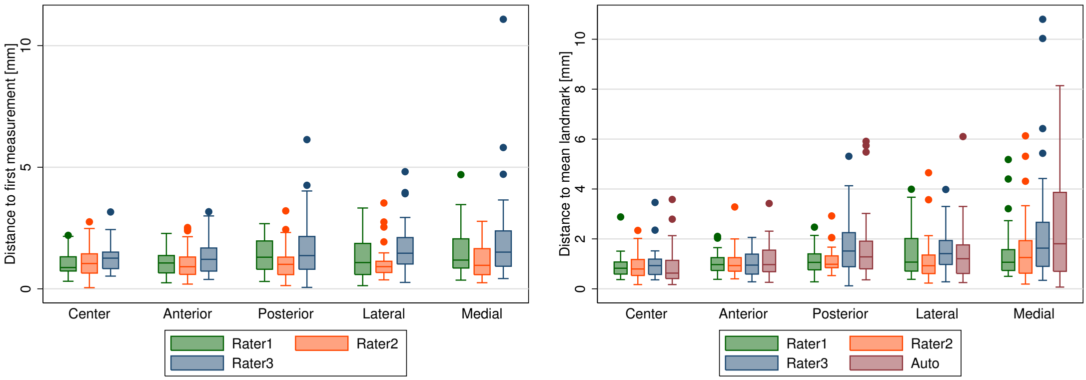

(a)

(b)

Figure 6: Comparison of the distance to the respective mean landmark point for the landmark points and each rater.

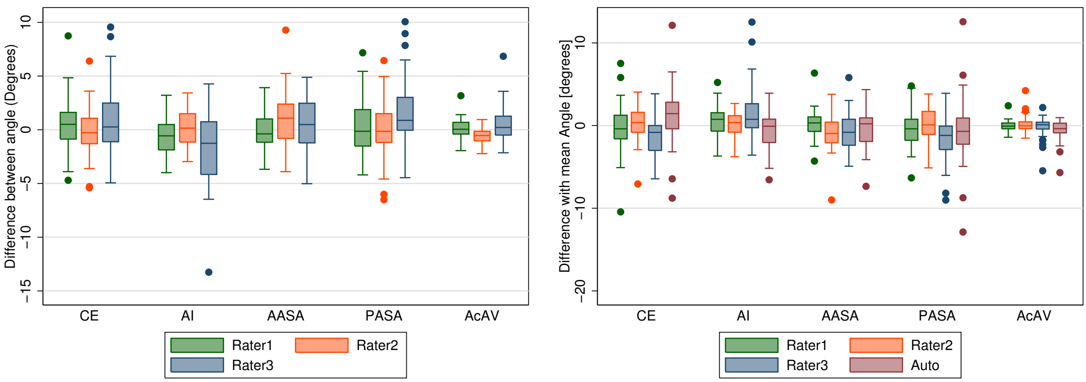

(a)

(b)

Figure 7: Comparison of the angles for each rater.

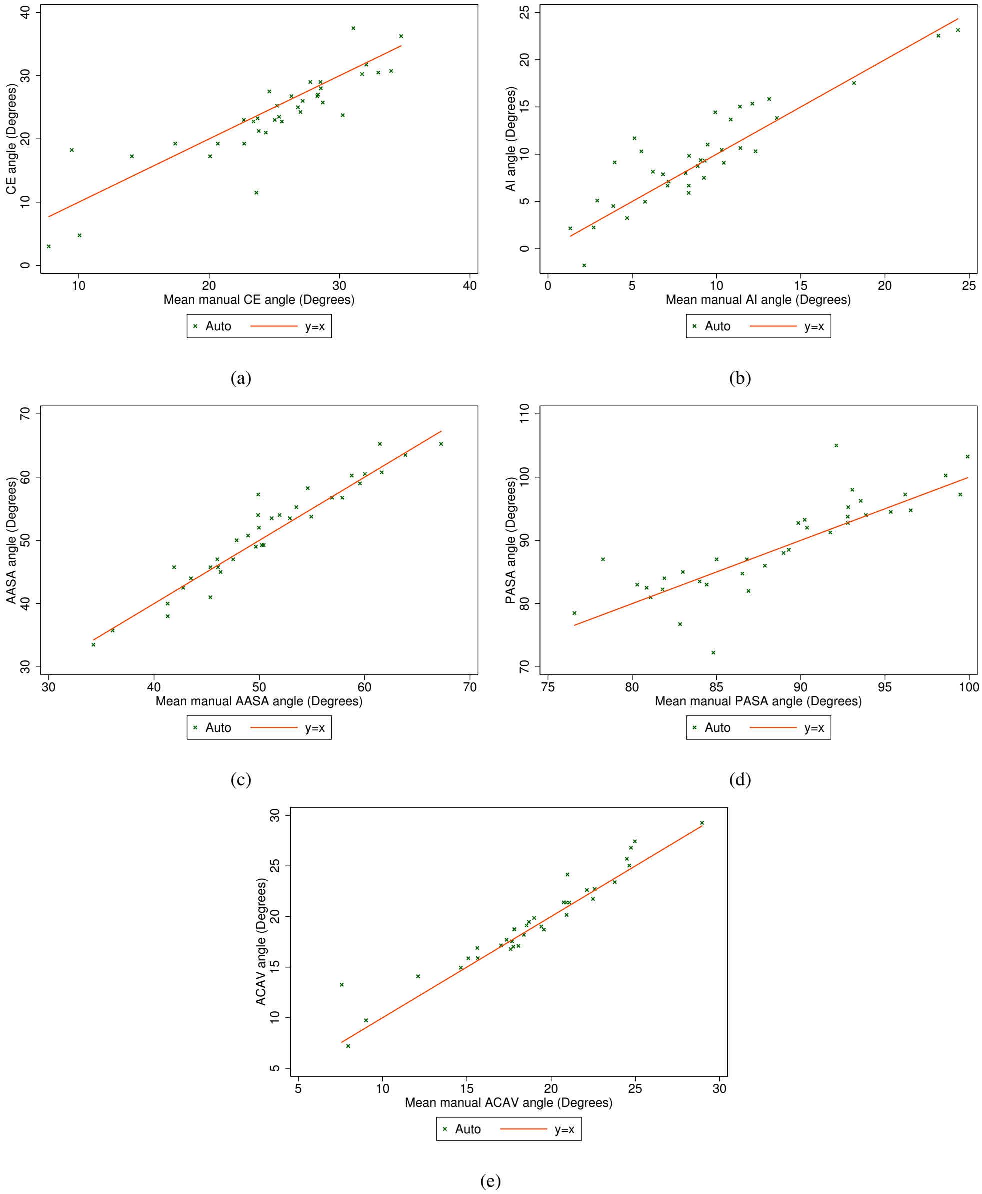

Figure 8: Scatter plots of mean manual angle measurement and the automatic method are shown.

Table 2: Optimized parameters per method. Parameters were varied with a fixed step between the minimum and maximum values.

Parameter	Description	Range	Curvature	Congruency	Combined
Center point					
d_{th}	Thresh. distance	0.1, 0.9	0.6	0.6	0.7
γ_n	Min. normal angle	0, 180	165	150	165
Lunate extract					
σ_κ	Curvature weight	0.1, 0.9	0.1	-	0.3
σ_θ	Congruency weight	0.1, 0.9	-	0.2	0.2
θ_c	Normal offset	0.1, 0.9	-	0.8	0.8
$d_{\min}$	Min. distance	0.1, 0.9	0.6	0.6	0.6
$d_{\max}$	Max. distance	0.1, 0.9	0.8	0.8	0.8
$\theta_{\min}$	Min. normal offset	-	160	160	160
$\kappa_{\max}$	Max. curvature	-	0.15	0.15	0.15
λ	Cost trade-off	1, 9	5	7	7
Criteria			842.2	1232.2	776.7

Table 4: Intraclass correlation coefficient for each angle measurement and 95% confidence interval.

Angle	ICC	95% CI
CE	0.96	0.93, 0.98
AI	0.94	0.89, 0.96
AASA	0.99	0.98, 0.99
PASA	0.96	0.94, 0.98
ACAV	0.99	0.98, 0.99

which corresponds to the ICC(A,k) model. We find an excellent ICC for all angle measurements, varying between 0.94 and 0.99 as shown in Table 4. Scatter plots of mean angle measurements and automatic method are shown in Figure 8.

6. Discussion

In this work we presented a completely automated method for acetabular lunate surface segmentation using CT images. We demonstrate the use of the resulting lunate surface to identify landmark points and calculate corresponding angle measurements used in the diagnosis of hip dysplasia. Finally, we validated the detected landmarks and measured angles against repeated measures by three raters with varying degrees of experience.

We found that the automatic identified landmark points were identified with similar accuracy as manual raters for all landmark points (center, anterior, posterior, medial, and lateral). In Figure 6(b) it is apparent that the medial landmark showed a larger mean difference and standard deviation than other landmark points. In Figure 6, we show two examples of cases where the raters disagreed in the correct landmark position. These cases illustrate the difficulty of selecting the landmark points and show that the automatic method produces reasonable results in the absence of a clear edge.

Manual landmark identification is a difficult and time consuming task and previous studies have found varying agreement between raters. We found that a less experienced rater performed statistically significantly worse than more experienced raters in identifying the lateral and medial landmarks in repeated measurements. This may be attributed to the difficulty of identifying the landmark points and identifying the limits of the lunate surface. The discrepancy between raters suggests that increased training is important to obtain reliable landmark positions.

The accurate selection of landmark points is especially difficult in three dimensions when selecting points on orthogonal or oblique slices. In this study, the points were selected on slices through the centers of the femoral heads. Errors in the selection of the center point will therefore influence the accuracy of selecting the remaining landmark points (Armiger et al., 2007). This is supported by our finding that the mean distance for both the intra- and inter-observer studies was found for the center point.

Another aspect is the limited resolution of the CT images, especially in the longitudinal axis, which may inhibit the correct identification of the landmark points. As both the medial and lateral point are selected on the coronal plane, this may have negatively contributed to the achievable accuracy. Increased resolution and iso-tropic voxel sizes would be an obvious improvement. Alternatively, allowing the raters to select the points on the bone surfaces extracted from the segmentation, as shown in Figure 9, may also contribute to improved accuracy in landmark placement.

To our knowledge, no previous study has investigated the accuracy of the placement of the acetabular landmarks in a similar study. Ehrhardt et al. (2004) use registration to transfer landmark points on a pelvis atlas to subjects. As validation, two raters placed 26 landmarks and repeated the measurements five times. They found that the average deviation of the manually determined landmarks was 2.5 mm and the maximum deviation was approximately 4 mm. Therefore no further analysis on the distances between automatically determined landmarks and manual landmarks was performed. In comparison to the current study, we found a mean of less than 2 mm. This may however be attributed to the lower resolution of their resampled images 2 mm^3 (originally 0.7 mm × 0.7 mm × 4.0 mm) compared to 0.45 mm × 0.45 mm × 1.25 mm used in the current study.

For angle measurements, we found that the automatic method performed similarly to the experienced raters with exception of the AcAV angle. However, the difference with rater 2 was less than one degree and within the variation expected and therefore not deemed clinically significantly different (Troelsen et al., 2010). A significant difference was found between the automatic method and rater 3 for both the CE and AI angle. For the CE angle, a slight bias can be seen with respect to the manual raters. For the AI angle, the automatic method does not show significant bias.

When comparing repeated measurements, the least experienced rater had a statistically significant difference for the AI and AcAV angles. Comparing the angle measurements to the mean angle measurement, we found that the third rater also showed a statistically significant difference with rater 2 for the AI angle. However, overall we found a good agreement between raters and excellent ICCs (ICC≥0.94) for all angle measurements.

In comparison to our previous method presented in De Raedt et al. (2013), we have removed any assumption regarding the shape of the acetabulum. As a result, the current method can locate the medial landmark in cases where the acetabulum is not spherical. However, in difficult cases we continue to find a difference between the manual raters and the automatic method. This may be in part explained by the fact that we compare to an imperfect standard (average of manual raters), evidenced by the outliers and larger standard deviation of manual measurements when identifying medial landmarks as described in the previous subsection.

Due to the variation in hip anatomy, some patients have less congruent joint surfaces anteriorly. In two cases this lead to the anterior lunate surface not extending to the level of the center of the femoral head. In these cases no anterior point can be found and the AASA and AcAV angles are undefined. In these cases, adjusting the minimum (d_{min}) and maximum (d_{max}) distances used for the initialization, led to the correct segmentation of the lunate surface.

As the method is completely automatic, the segmentation and analysis can be performed offline. Subsequently, the results can be verified by a radiologist. The complete processing can be performed in approximately five minutes. This may be significant advantage as the work pressure increases and the time per patient decreases.

We compared several variants of a cost function for the mesh segmentation and optimized the parameters using manual measurements. An extensive grid search over all sphere-fitting and lunate segmentation parameters was performed. As intuitively expected, the curvature based cost function performed better than the congruency cost function. However, a combined cost function out performed both methods. A limitation of the parameter optimization was that the error function was based on the distance between the five landmark points and not the complete lunate outline. Training on manual annotations of the lunate may result in more accurate segmentation along the outline.

For the detection of the center point of the femur, we assume that the head of the femur is spherical. However, in patients with Legg-Calvé-Perthes, the femoral head is often deformed and the identification of the center point is less difficult. In our manual experiments, we found that human raters also had difficulty in finding the center of the femoral head in cases with Legg-Calvé-Perthes. To improve the automatic center point detection, an ovoid may be fit to the surface. Finally, the fitting error may be used to alert a radiologist to any possible problems.

In the current study, we have focused on the measurement of angles relevant for the diagnosis of hip dysplasia. However, the resulting lunate surface may also be used for detection of the acetabular opening plane and measurement of the retroversion of the acetabulum such as in (Puls et al., 2011; Subburaj et al., 2008; Tan et al., 2008). In addition the method may be used to produce surface meshes for the analysis of pressure distributions as used in (Armiger et al., 2009).

7. Conclusions

In summary, we have presented an automatic method for lunate surface segmentation with an extensive validation using manual measurements. We found that manual and automatic detected landmark points were found with similar accuracy. Finally, we found that angle measurements showed excellent agreement with manual angle measurements. The technique is of clinical relevance and in the future may be used in for both diagnosis and surgical planning, with the potential to greatly reduce the time used for analysis per patient.

References

Agricola, R., Heijboer, M.P., Roze, R.H., Reijman, M., Bierma-Zeinstra, S., Verhaar, J.A.N., Weinans, H., Waarsing, J.H., 2013. Pincer deformity does not lead to osteoarthritis of the hip whereas acetabular dysplasia does: Acetabular coverage and development of osteoarthritis in a nationwide prospective cohort study (CHECK). Osteoarthritis and Cartilage 21, 1514–1521.

Anda, S., Terjesen, T., Kvistad, K.A., 1991. Computed tomography measurements of the acetabulum in adult dysplastic hips: Which level is appropriate? Skeletal Radiol 20, 267–271.

Armand, M., Lepistö, J.V.S., Merkle, A.C., Tallroth, K., Liu, X., Taylor, R.H., Wenz, J., 2004. Computer-aided orthopedic surgery with near-real-time biomechanical feedback. Johns Hopkins APL Technical Digest (Applied Physics Laboratory) 25, 242–252.

Armiger, R.S., Armand, M., Lepisto, J., Minhas, D., Tallroth, K., Mears, S.C., Waites, M.D., Taylor, R.H., 2007. Evaluation of a computerized measurement technique for joint alignment before and during periacetabular osteotomy. Comput. Aided Surg. 12, 215–224.

Armiger, R.S., Armand, M., Tallroth, K., Lepisto, J., Mears, S.C., 2009. Three-dimensional mechanical evaluation of joint contact pressure in 12 periacetabular osteotomy patients with 10-year follow-up. Acta Orthop 80, 155–161.

Boykov, Y., Funka-Lea, G., 2006. Graph Cuts and Efficient N-D Image Segmentation. Int J Comput Vision 70, 109–131.

Boykov, Y., Kolmogorov, V., 2004. An experimental comparison of min-cut/max-flow algorithms for energy minimization in vision. IEEE Transactions on Pattern Analysis and Machine Intelligence 26, 1124–1137.

Clohisy, J.C., Carlisle, J.C., Trousdale, R., Kim, Y.J., Morgan, P., Steger-May, K., Schoenecker, P.L., Millis, M., 2009. Radiographic evaluation of the hip has limited reliability. Clin. Orthop. Relat. Res. 467, 666–675.

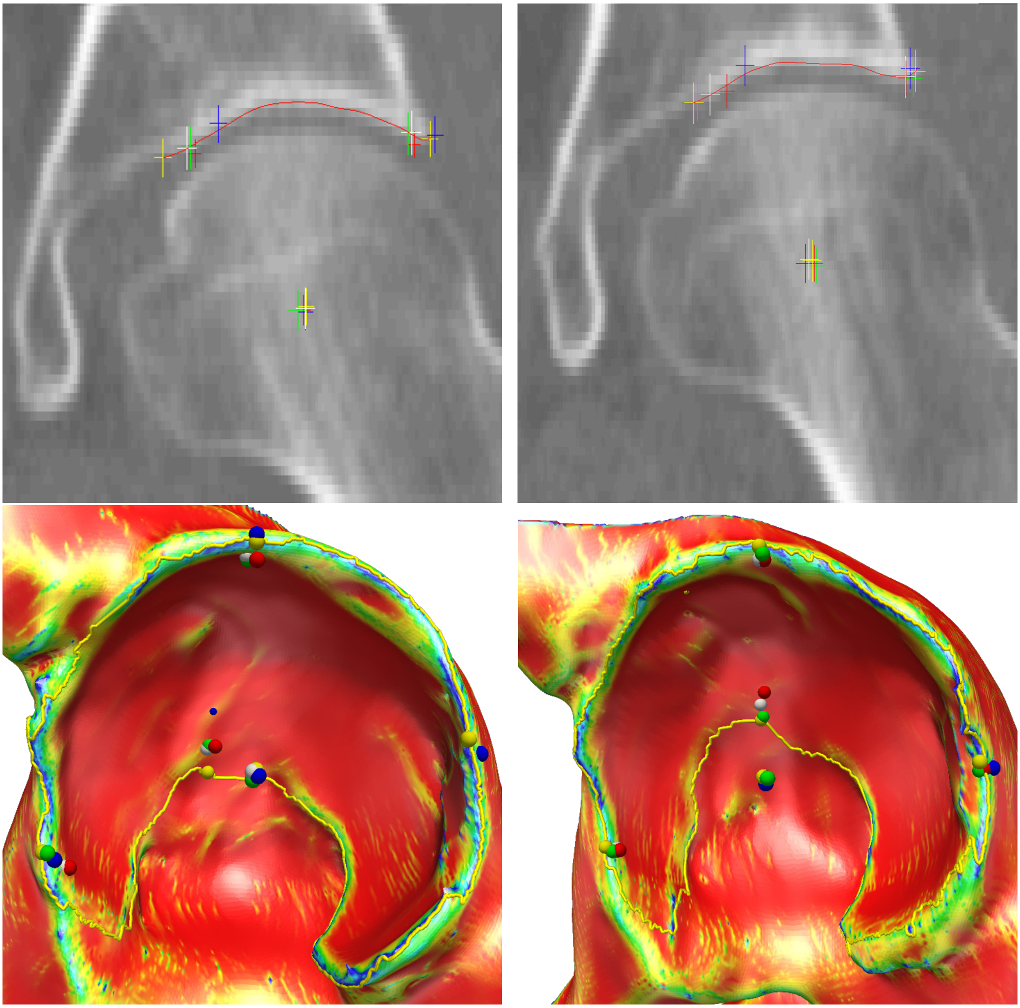

(a) (b)

Figure 9: Comparison of the distance to the respective mean landmark point for the landmark points and each rater. We show points for Rater 1 (red), Rater 2 (green), Rater 3 (blue), Mean (white), and the automatic (yellow). In the coronal slice we show the segmented lunate surface in red. In the 3D we show the resulting outline of the lunate surface in yellow.

De Raedt, S., Mechlenburg, I., Stilling, M., Rømer, L., Søballe, K., de Bruijne, M., 2013. Automated measurement of diagnostic angles for hip dysplasia, in: Proceedings of SPIE - The International Society for Optical Engineering.

Descoteaux, M., Audette, M., Chinzei, K., Siddiqi, K., 2006. Bone enhancement filtering: Application to sinus bone segmentation and simulation of pituitary surgery. Comput. Aided Surg. 11, 247–255.

Ehrhardt, J., Handels, H., Plötz, W., Pöppl, S.J., 2004. Atlas-based recognition of anatomical structures and landmarks and the automatic computation of orthopedic parameters. Methods Inf Med 43, 391–397.

Frangi, A.F., Niessen, W.J., Vincken, K.L., Viergever, M.A., 1998. Multi-scale vessel enhancement filtering, in: Lecture Notes in Computer Science, Springer Berlin Heidelberg, Berlin, Heidelberg. pp. 130–137.

Harris, W.H., 1986. Etiology of osteoarthritis of the hip. Clin. Orthop. Relat. Res. No. 213, 20–33.

Hipp, J.A., Sugano, N., Millis, M.B., Murphy, S.B., 1999. Planning acetabular redirection osteotomies based on joint contact pressures. Clin. Orthop. Relat. Res. , 134–143.

Klaue, K., Wallin, A., Ganz, R., 1988. CT evaluation of coverage and congruency of the hip prior to osteotomy. Clin. Orthop. Relat. Res. , 15–25.

Krčah, M., Székely, G., Blanc, R., 2011. Fully automatic and fast segmentation of the femur bone from 3D-CT images with no shape prior, in: ISBI, pp. 2087–2090.

Larson, A.N., Rabenhorst, B., De La Rocha, A., Sucato, D.J., 2012. Limited Intraobserver and Interobserver Reliability for the Common Measures of Hip Joint Congruency Used in Dysplasia. Clin. Orthop. Relat. Res. 470, 1414–1420.

Lloyd-Roberts, G.C., 1955. OSTEOARTHRITIS OF THE HIP A Study of the Clinical Pathology. J Bone Joint Surg Br 37-B, 8–47.

Lorensen, W.E., Cline, H.E., 1987. MARCHING CUBES: A HIGH RESOLUTION 3D SURFACE CONSTRUCTION ALGORITHM. Computer Graphics (ACM) 21, 163–169.

Pompe, B., Antolic, V., Iglic, A., Kralj-Iglic, V., Mavcic, B., Smrke, D., 2000. Evaluation of biomechanical status of dysplastic human hips. Pflugers Arch. 440, R202–3.

Puls, M., Ecker, T.M., Steppacher, S.D., Tannast, M., Siebenrock, K.A., Kowal, J.H., 2011. Automated detection of the osseous acetabular rim using three-dimensional models of the pelvis. Comput. Biol. Med. 41, 285–291.

Sato, Y., Nakajima, S., Shiraga, N., Atsumi, H., Yoshida, S., Koller, T., Gerig, G., Kikinis, R., 1998. Three-dimensional multi-scale line filter for segmentation and visualization of curvilinear structures in medical images. Med Image Anal 2, 143–168.

Sharp, I.K., 1961. ACETABULAR DYSPLASIA The Acetabular Angle. J Bone Joint Surg Br 43-B, 268–272.

Steppacher, S.D., Lerch, T.D., Gharanizadeh, K., Liechti, E.F., Werlen, S.F., Puls, M., Tannast, M., Siebenrock, K.A., 2014. Size and shape of the lunate surface in different types of pincer impingement: theoretical implications for surgical therapy. Osteoarthritis and Cartilage 22, 951–958.

Subburaj, K., Ravi, B., Agarwal, M.G., 2008. 3D shape reasoning for identifying anatomical landmarks. Computer-Aided Design and Applications 5, 153–160.

Surazhsky, T., Magid, E., Soldea, O., Elber, G., Rivlin, E., 2003. A comparison of Gaussian and mean curvatures estimation methods on triangular meshes, in: Proceedings - IEEE International Conference on Robotics and Automation, pp. 1021–1026.

Tan, S., Yao, J., Yao, L., Summers, R.M., Ward, M.M., 2008. Acetabular rim and surface segmentation for hip surgery planning and dysplasia evaluation, in: Progress in Biomedical Optics and Imaging - Proceedings of SPIE.

Tönnis, D., 1987. Congenital Dysplasia and Dislocation of the Hip in Children and Adults. Springer Berlin Heidelberg, Berlin, Heidelberg.

Tönnis, D., Heinecke, A., 1999. Acetabular and femoral anteversion: Relationship with osteoarthritis of the hip. J Bone Joint Surg Am 81, 1747–1770.

Troelsen, A., Rømer, L., Kring, S., Elmengaard, B., Søballe, K., 2010. Assessment of hip dysplasia and osteoarthritis: Variability of different methods. Acta Radiol 51, 187–193.

Wassilew, G.I., Heller, M.O., Diederichs, G., Janz, V., Wenzl, M., Perka, C., 2012. Standardized AP radiographs do not provide reliable diagnostic measures for the assessment of acetabular retroversion. J. Orthop. Res. 30, 1369–1376.

Wiberg, G., 1939. Studies on dysplastic acetabula and congenital subluxation of the hip joint. Acta Orthop Scand 83.

Paper II

Morphology, gender, and hip dysplasia

Morphology of the dysplastic hip and the relationship with gender and acetabular version

Sepp De Raedt[1,2,*], Hakim C. Achterberg[3], Inger Mechlenburg[1,2], Maiken Stilling[1,4], Lone Rømer[5], Kjeld Søballe[4], Marleen de Bruijne[3,6],

1 Dept. of Clinical Medicine, Aarhus University, Aarhus, Denmark
2 Orthopaedic Research Unit, Aarhus University Hospital, Aarhus, Denmark
3 Depts. of Radiology and Medical Informatics, Erasmus MC Rotterdam, Rotterdam, The Netherlands
4 Dept. of Orthopaedics, Aarhus University Hospital, Aarhus, Denmark
5 Dept. of Radiology, Aarhus University Hospital, Aarhus, Denmark
6 Dept. of Computer Science, University of Copenhagen, Copenhagen, Denmark

*** sepp.de.raedt@clin.au.dk**

Abstract

The dysplastic hip is characterized by a shallow socket and a steep roof, resulting in the incomplete coverage of the femoral head. However, the morphological variation of the hip joint is diverse and clear differences exist between males and females. The exact relationship between morphology, gender, and hip dysplasia has not previously been described. The aim of the study was therefore to investigate the relationship between the morphology of the hip, gender, and hip dysplasia using a three dimensional model.

Statistical shape models of the combined femur and pelvic bones were created from bilateral hips of 75 patients. Using manual angle measurements and regression analysis, the characteristic shape differences associated with gender and hip dysplasia were determined. We developed a novel method to visualize the characteristic shape differences found by regression analysis. The model showed clear differences associated with gender and hip dysplasia. We found that the acetabular anteversion in females was significantly higher ($p=< 0.0001$) than males and no significant difference in acetabular anteversion was found between normal and dysplastic hips ($p=0.1137$). The model showed that decreased acetabular anteversion resulted in the appearance of the cross-over sign and the prominent ischial spine sign commonly associated with retroversion. In leave-one-out experiments, it was found that gender could be

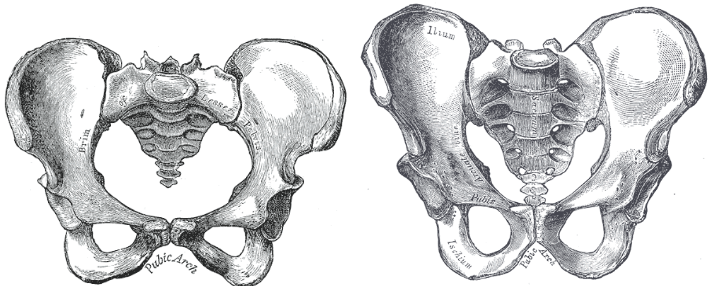

(a) Female (b) Male

Figure 1. Reference figures of the male and female pelvis. Indicative gender differences are the difference in angle of the pubic arch, shape of the pelvic inlet, and the width and height of the pelvis (Henry Vandyke Carter [Public domain], via Wikimedia Commons).

predicted with an area under the curve of 0.99 and hip dysplasia could be predicted with an area under the curve of ≥ 0.73.

Our findings suggest that retroversion is a result of decreased anteversion of the acetabulum and is primarily associated with gender. This finding is of clinical relevance and should be taken into account during the reorientation of the acetabulum in periacetabular osteotomies.

Introduction

The morphology of the hip joint and its relationship with hip diseases and gender is not well understood. In clinical practice, it is apparent that there is a wide spectrum of acetabular configurations and subtle variations and combinations of different deformities are often observed. In diseases such as hip dysplasia and femoroacetabular impingement (FAI), the pathological bone morphology leads to an abnormal biomechanic relationship between the femur and acetabulum causing pain and disability.

In hip dysplasia, the acetabulum is characterized by a shallow socket with a steep roof resulting in lacking global coverage of the femur [1, 2, 3]. In FAI, with a pincer deformity, the acetabulum is described to be deep with over-coverage of the femoral head leading to risk of impingement of the labrum [4]. In FAI, with a cam deformity, a bump at the neck-head junction of the proximal femur results in increased risk of impingement with the anterior rim of the acetabulum [5]. In between the two extremes described by hip dysplasia and FAI, there are varying degrees and combinations with both pathological and normal morphological variation of the acetabulum and femur.

Another important morphological variation of the pelvis is the direction of the acetabular opening, which is described by the version of the acetabulum [6]. On conventional radiographs, the version is judged by examining the shadows of the lateral edge of the anterior and posterior walls [6]. In an anteverted acetabulum the opening points anteriorly and the posterior wall remains lateral to the anterior wall. In retroverted acetabula, the opening is orientated more posteriorly and the posterior and anterior walls cross-over forming a figure eight [6, 7]. Although it is generally thought that hip dysplasia is associated with an anteverted acetabulum, previous work has found that up to one third of dysplastic hips are retroverted [6, 8, 9]. During the treatment of hip dysplasia, it is important to take into account the version of the acetabulum to normalize the anterior and posterior coverage [6, 8]. It is therefore important to understand how the version of the acetabulum varies with respect to normal and dysplastic hips.

The dimorphism of the pelvis with respect to gender is well established [10]. In addition, it is also known that the incidence of symptomatic hip dysplasia is up-to four times higher in females than in males [11, 12]. Conversely, it has also been found that cam impingement is more common in males [4]. It is however unclear if the difference in shape of the pelvis may be associated with the difference in incidence of the two diseases. In this work we therefore aim to obtain a better understanding of the relationship between the shape variation of the hip and gender.

Statistical shape modeling is a common technique that can be used to study the morphological variation and the association with different characteristics [13, 14]. Statistical shape models capture the mean shape of a set of shapes and the main modes of variation based on principle component analysis (PCA) [15]. In previous work, the two-dimensional morphology of the femur and acetabulum have been investigated based on AP radiographs. Various studies have used two-dimensional statistical shape models to predict the development of OA and risk of total hip replacement [16, 17, 18]. Three-dimensional studies on the proximal femur have investigated the relationship between shape and Legg-Calvé-Perthes and FAI with a cam deformity [19, 20]. However, no previous work has studied the three dimensional shape variation in a combined pelvis and femur model and the association with hip dysplasia and gender.

In this study, we therefore aimed to study the association between morphology, gender, and hip dysplasia in order to better understand the morphology of the hip. We created combined models of the the pelvic bones and femurs and used them to study the association by regression analysis. In the following section we will first introduce the process used to construct the statistical shape model. We also introduce a novel method to visualize the relationship between linear regression models and the shape parameters associated with the dependent variable. In experiments, we first introduce the data used and demonstrate the use of the developed method to determine the difference in pelvis shape between genders. Subsequently, we study the association between hip dysplasia and acetabular version using individual left and right hip models.

Methods

In this work we make use of a statistical shape model commonly referred to as a point distribution model (PDM). This statistical shape model introduced by Cootes et al. [15], represents shapes as a collection of points and models the mean shape and the variation of the shapes observed in a set of example shapes. The construction of the PDM requires that each shape consists of corresponding points across shapes.

In the following section we detail the method used to establish the point correspondences in the current study. Subsequently, we briefly introduce the method used to construct the statistical shape model. Since we would like to visualize the characteristic differences found by regression analysis, we derive a relationship between the shape parameters and the regression coefficients of regression models. This derivation is introduced in the final subsection.

Point correspondence

Corresponding points are points that represent the same point on each shape [13, 14, 15]. In this work shapes represent bones and the set of shapes is formed by the same bone from each of the included subjects. Therefore, corresponding points represent anatomical landmark points on a bone such as the anterior inferior iliac spine or the most anterior superior point on the pubic symphysis. In two dimensions and for small datasets, corresponding points can be placed by hand by an experienced operator. However, in three-dimensions and for a large number of subjects this becomes labor intensive and prohibitively difficult. Therefore, automatic techniques are commonly used to automatically establish corresponding points [13, 14, 21].

In this work we use non-rigid group-wise image registration to establish point correspondences similar to the atlas construction method introduced by Seghers et al. [22]. A schematic overview of the used procedure is illustrated in Figure 2. We first perform preprocessing of the CT images and subsequently use the images and resulting masks for image registration to obtain individual shapes with corresponding points for each subject. The procedure is repeated for each femur and pelvic bone for both left and right hips separately. In the following description we therefore refer to a bone as a single bone from a subject, such as left femur, and the set of bones is the collection of left femur bones from all subjects.

Prior to image registration, we performed preprocessing as shown in Figure 2. We first segmented all bones from the CT image using an automatic graph cut segmentation method that uses a sheetness based cost function to find the optimal separation between areas estimated to be bone and background such as soft-tissue, skin, etc. [23, 24, 25]. The individual left and right femur and pelvic bones were identified and consistently labeled, resulting in binary segmentations $\mathtt{B}_{i,j}$. Where i is the subject identifier and j is the bone identifier. For input to the registration process, pairs of mask images $\mathtt{M}_{i,j}$ were created. The binary bone segmentation was dilated and used as a fixed image mask in the registration. Soft masks were created by smoothing

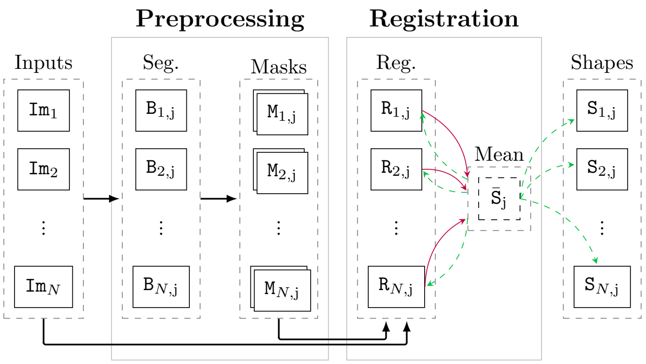

Figure 2. Schematic overview of pipeline used to obtain individual shapes with point correspondences from N input images, using image segmentation and group-wise registration. Each input image $\mathtt{Im}_i$ is segmented, producing a binary segmentation $\mathtt{B}_{i,j}$ for subject i and bone j. The mask images $\mathtt{M}_{i,j}$ and input images are then used to perform pairwise registrations $\mathtt{R}_{i,j}$. $\bar{\mathtt{S}}_j$ is the mean shape obtained from the mean soft mask image and $\mathtt{S}_{i,j}$ are the individual shapes.

the distance transform of the binary segmentation using the Q-function in order to reduce aliasing effects, similar to the method used by Metz et al. [26]. This ensures that the isolevel is preserved and a smooth transition occurs at the boundary.

As described by Seghers et al. [22], the registration procedure requires the pairwise registration of each of the bones from all subjects. The individual registrations consisted of three consecutive registrations. Initial alignment was established with a rigid and affine transformation using the previously created softmasks. Subsequently, a non-rigid B-spline registration was performed with the CT grey-scale images and masks for the fixed image. A final non-rigid B-spline registration using the soft-masks was performed to refine the alignment of the contours of the bones. All registrations were performed using the sum of squared differences similarity metric. The resulting pairwise transformations were subsequently averaged to obtain the mean transformation, which maps points from the individual subject space to the mean space. To transform images from the subject space to the mean space, the inverse transform must be found. Therefore, the inverse transformation was found by performing an affine and B-spline registration with a displacement magnitude metric [27]. Finally, after transforming the softmask to the mean space for each subject, a voxel wise averaging is performed to obtain a mean softmask. The mean shape $\bar{\mathtt{S}}_j$ can then be extracted from the mean softmask image using the marching cubes algorithm [28].

The resulting mesh is the mean bone shape and consists of points and polygons. To obtain the bone shape for each of the individual subjects, the mean shape is then non-rigidly transformed from the mean space to the patient space by the previously found inverse transformation.

Shape alignment and pose correction

Prior to the construction of the PDMs, it is necessary to align the individual shapes in order to remove variation caused by differences in pose and scale. In this work we use Generalized Procrustes Analysis (GPA) [29]. However, as we are interested in a combined model of the pelvic bones and femurs, a modified procedure is used. Due to differences in positioning at the time of scanning, the femur pose with respect to the acetabulum may vary significantly between subjects. Therefore, we perform pose correction of the femurs to a mean pose while preserving the location of the center of the head. Maintaining the position of the center of the head preserves the relationship between the femur and acetabulum and allows the evaluation of for example subluxation and congruency of the joint.

The shape alignment procedure started with the alignment of the combined left and right pelvic bones using GPA with scaling. This establishes the alignment of the pelvic bones and removes size differences. The same transformation was then applied to the femur bones and the centers of the individual femoral heads were calculated using sphere fitting [24]. Subsequently, the left and right femurs were separately aligned using only rotations and translations to remove pose differences of the femur between subjects. To restore the position of the head, the individual femurs were then translated such that the center of the femoral head coincided with the initial center point. The translation was calculated as the vector from the transformed center to the original center of the femoral head. The pose correction procedure was then repeated until convergence and no points moved.

Point distribution model

The PDM can be constructed using the set of aligned shapes obtained from the previous steps. The set of shapes used for the construction of shape model are commonly referred to as training shapes. Each of the N shapes with n points is represented as a vector of $3n$ concatenated point coordinates such that the i^{th} shape is represented as $\boldsymbol{x}_i = [x_{i,1}, y_{i,1}, z_{i,1}, \ldots, x_{i,n}, y_{i,n}, z_{i,n}]$. The mean shape can then be calculated as:

$$\bar{\boldsymbol{x}} = \frac{1}{N}\sum_{i=1}^{N}\boldsymbol{x}_i. \tag{1}$$

The deviation of individual shapes from the mean can then be quantified as $d\boldsymbol{x}_i = \boldsymbol{x}_i - \bar{\boldsymbol{x}}$. The displacement vectors $d\boldsymbol{x}_i$ represent the displacement of individual points from the mean shape for each shape and can be used to calculate the covariance matrix $\boldsymbol{S}$ defined as:

$$\boldsymbol{S} = \frac{1}{N}\sum_{i=1}^{N} d\boldsymbol{x}_i d\boldsymbol{x}_i^T. \tag{2}$$

Performing principle component analysis of the covariance matrix, results in the eigenvectors and eigenvalues describing the main modes of variation, commonly referred to as modes, of the included shapes. The k^{th} eigenvector is denoted $\boldsymbol{\phi}_k$ and the associated eigenvalue as λ_k, where the magnitude of the eigenvalue is the amount of variance explained by the mode. The eigenvalues are sorted in descending order such that $\lambda_k \geq \lambda_{k+1}$. The statistical shape model can then be represented as:

$$\boldsymbol{x} = \bar{\boldsymbol{x}} + \Phi \boldsymbol{b}, \tag{3}$$

where Φ is the matrix of eigenvectors and $\boldsymbol{b}$ are the shape parameters. The shape parameters weigh the contribution of each eigenvector and can be varied to obtain a new shape. Varying the shape parameters between appropriate limits, results in plausible variation described by the statistical shape model.

Regression analysis

Regression analysis is a powerful, but simple method to establish the relationship between dependent and independent variables. In this work, the aim is to find a regression model to find the characteristic difference in shape associated with dependent variables such as gender, dysplasia, or angle measurements. In this section, we derive an expression in order to visualize the characteristic shape differences using the resulting models. We first derive the relationship for logistic regression and subsequently for linear regression. The logistic function is defined as:

$$P(Y = y|\boldsymbol{\beta}, \boldsymbol{b}) = \frac{1}{1 + e^{-(\beta_0 + \sum_{i=1}^{t} \beta_i b_i)}}, \tag{4}$$

where P is the probability associated with the dependent variable Y and a given set of shape parameters $\boldsymbol{b} = [b_1, ..., b_t]$ and regression coefficients $\boldsymbol{\beta} = [\beta_0, ..., \beta_t]$ from a shape model with t modes. y is a binary indicator for the dependent variable, where for example $y = 1$ for female and $y = 0$ for male. A regression model can then be found by optimizing:

$$\boldsymbol{\beta}^* = \underset{\boldsymbol{\beta}}{\operatorname{argmax}} \left(\ln \left[\prod_j P(y^j | \boldsymbol{b}^j, \boldsymbol{\beta}) \right] - \lambda \sum_{i>0} \beta_i^2 \right), \tag{5}$$

where the first term is the likelihood of the model and the second term provides regularization to constrain the size of the weights [30] and j is an indicator for the dependent variable. The regularization is known as ridge regression and is based on the $l2$ norm [31]. The strength of the regularization term is determined by λ which is found by leave-one-out or generalized cross-validation [32, 33]. After optimization of the logistic regression model, the values of the regression coefficients $\boldsymbol{\beta}$ determine the direction associated with the dependent variable of the logistic regression model, where β_0 is the intercept term and β_i is the regression coefficient associated with mode i for $i > 0$. The intercept term is the log of the odds associated with the prevalence of the dependent variable.

To visualize the characteristic shape differences related to the outcome Y, we choose to visualize the mean shape deformed along the discriminating direction. In the experiments we will show that selecting a point on the regression line, results in shapes describing the characteristic shape associated with a certain value of P. We now rewrite the logistic function in terms of the logit function, such that we obtain:

$$logit(p) = log(\frac{p}{1-p}) = \beta_0 + \sum_{i=1}^{t} \beta_i b_i, \tag{6}$$

where for brevity we have introduced p, which is taken to be $P(Y = 1|\boldsymbol{\beta}, \boldsymbol{b})$. The resulting expression is a linear function of the shape parameters and regression coefficients. We now propose to take $\boldsymbol{b} = c\boldsymbol{\beta}$, where c is a scaling factor determining the position on the regression line. Rearranging (6) we obtain:

$$\sum_{i=1}^{t} \beta_i b_i = log(\frac{p}{1-p}) - \beta_0. \tag{7}$$

Now we substitute the $c\beta_i$ for b_i, where c is the scaling parameter to be determined and obtain:

$$c\sum_{i=1}^{t} \beta_i^2 = log(\frac{p}{1-p}) - \beta_0, \tag{8}$$

which can subsequently be rewritten as:

$$c(p, \boldsymbol{\beta}) = \frac{log(\frac{p}{1-p}) - \beta_0}{\sum_{i=1}^{t} \beta_i^2}, \tag{9}$$

to obtain an expression for c for a given probability p and $\boldsymbol{\beta}$. With the derived equation, we can calculate the model coefficients $\boldsymbol{b}$ associated with a certain probability as $\boldsymbol{b} = c\boldsymbol{\beta}$. For linear regression, a similar equation can be derived as:

$$c(y, \boldsymbol{\beta}) = \frac{y - \beta_0}{\sum_{i=1}^{t} \beta_i^2}. \tag{10}$$

Experiments

Data

In this retrospective study, 75 patients were identified that underwent CT investigation of the hip between January 2006 and October 2008. Patients were referred to scanning due to symptomatic hip pain, most commonly due to suspected primary or secondary hip dysplasia. Scans were acquired according to a standardized protocol with the patient in a supine position and legs in a neutral position. The scan volume ranged from superior to the acetabulum to approximately below the lesser trochanter.

Scans were acquired on a Philips Mx8000, Philips Brilliance 40, or Philips Brilliance 64 (Philips Medical Systems Best, Best, The Netherlands) scanner. Scan resolution and spacing varied, but the mean voxel size was $0.45\,\text{mm} \times 0.45\,\text{mm} \times 1.25\,\text{mm}$. In-plane voxel size ranged from 0.38 mm to 0.52 mm

Table 1. Summary statistics for angle measurements combined for left and right sides. One patient had missing angle measurements and was excluded from analysis. P-values for differences with respect to gender and dysplasia are shown. See text for details.

Angle	**Total** (N=74)		**Male** (N=24)		**Female** (N=50)		**Gender**	**Dysplasia**
	Mean	SD	Mean	SD	Mean	SD	p-value	p-value
CE	20.4	9.4	20.6	10.1	20.4	9.1	0.7174	< 0.0001
AI	13.5	8.2	13.6	7.7	13.5	8.4	0.5928	< 0.0001
AcAV	20.1	5.4	16.2	4.1	22.1	5.0	< 0.0001	0.1137
AASA	49.3	9.0	52.7	8.4	47.7	8.9	0.0060	< 0.0001
PASA	90.1	8.3	86.0	6.9	92.1	8.2	< 0.0001	0.0013
HASA	139.5	13.3	138.7	12.6	139.8	13.7	0.3831	< 0.0001

and the out-of-plane voxel size ranged from 1.25 mm to 1.6 mm.

Manual angle measurements

An experienced radiologist (LR) performed manual measurements on a Philips PACS workstation (Philips Medical Systems, Best, Netherlands). The radiologist measured the center-edge (CE) angle of Wiberg [34] and acetabular index (AI) of Tonnis [35] in the coronal slice passing through the centers of the femur. In the axial slice passing through the centers of the femur, the anterior-sector (AASA) and posterior-sector (PASA) angles and the acetabular anteversion (AcAV) angle were measured according to the standard definition [36]. The horizontal-sector (HASA) angle was calculated as the sum of the anterior-sector and posterior-sector angles [36]. A positive diagnosis of hip dysplasia was defined as a center-edge angle less than 25° [37]. Differences in angle measurements were analyzed by a two-way mixed effects analysis of variance (ANOVA) model with one within-subject factor (left and right side) and two between-subject terms for gender and hip dysplasia with interaction between side and both between-subject terms. A p-value of less than 0.05 was found to be statistically significant. All analysis was performed with Stata 13 (StataCorp, College Station, USA).

Median age was 36 (Range:13 and 65) years and there was no significant difference in age with respect to gender (p=0.55) or hip dysplasia (p=0.15). Angle measurements and analysis results are summarized in Table 1. No significant interactions were found between side and the between-subject factors. No significant difference was found with respect to gender for the CE, AI, and the HASA angles. Meaning that the lateral and total anterior and posterior coverage was similar between men and women. A significant difference with respect to gender was found for the AcAV, AASA, and PASA. Meaning that the version of the acetabulum and the posterior and anterior coverage differed by gender. All angle measurements, except for AcAV were significantly different between non-dysplastic and dysplastic hips.

Model building

Using the procedure described in the methods section, three statistical shape models were constructed using the above described data. Segmentations were performed using an automatic graph cut segmentation method [25]. Masks for image registration were created by dilating the segmentation by 5 voxels and excluding areas of the adjacent bone. Softmasks were created using the Q function with a mean of 0 and standard deviation of 1. All images in the registration were cropped to contain the bone of interest including a margin of 10 voxels on all sides. All image registration was performed with `elastix` 4.7 [38]. Each registration was performed on three levels with a Gaussian pyramid with smoothing and down-sampling [39]. Final grid-spacing for the initial grey-scale B-spline registration was 10 mm and 5 mm for the final softmask registration. The inverse transformation was calculated with a final grid-spacing of 5 mm. The used parameter files will be made publicly available. The mean bone shapes were extracted, smoothed and simplified to approximately 10,0000 points using VTK [40]. The alignment of the pelvis was performed and the femur pose was corrected. The pose correction converged to within machine precision in 5 iterations.

Individual models were created by concatenating individual bones together. First a combined model of the complete pelvis and femur was constructed. This model preserves the orientation between the left and right pelvic bones. In addition, two models of the individual left and right pelvic bones and femur were constructed. The PDM models were created using a custom application based on the open source framework for statistical shape modeling Statismo [41].

Finally, the regression models were created. Due to the number of modes and to prevent over-fitting of the model, we retain the number of modes that explain 95% of the variation of the model and perform regularization during the optimization of the regression models. We used the $l2$ norm for regularization for all experiments. The regularization parameter λ was determined by 10 fold cross-validation with 100 values evenly spaced on the log scale. The minimum and maximum values were selected to ensure that the global optimum was found by visual inspection of the deviance versus λ plot. For logistic regression a stratified cross-validation was performed and the criteria was the negative log-likelihood. For linear regression, the R^2 coefficient of determination was used as cross-validation metric. Each model was built using a leave-one-out cross-validation, in order to obtain a true estimate of the predictive value of the model. All regression models were created with Scikit-learn [42].

Complete model

The resulting complete pelvis and femur model is shown in Figure 3. The first four modes are illustrated for each model. Each mode is shown as the mean shape $\bar{\boldsymbol{x}}$ perturbed by 3 standard deviations. To facilitate interpretation and highlight differences, the model points are colored by the point displacements, normalized by the maximum point displacement within the mode. Points on the model that move

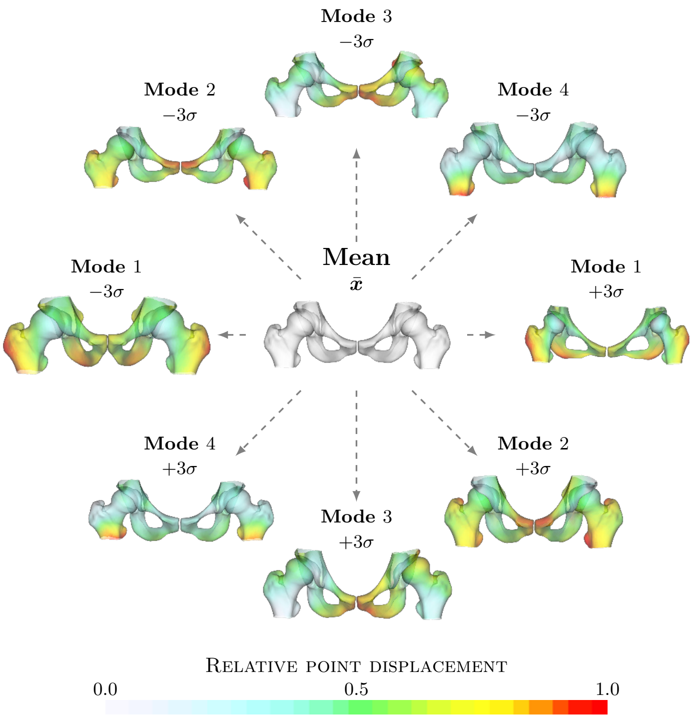

Figure 3. Visualization of the mean pelvis and femur model and the four most significant modes explaining 69% of the total variation in the model. Each mode is shown as $\bar{\boldsymbol{x}} \pm 3$ standard deviations. Colors indicate the point displacement normalized by the maximum displacement for a mode.

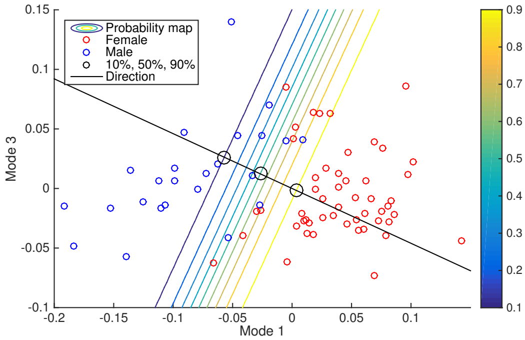

Figure 4. Scatter plot of coefficients for mode 1 and 3 showing male and female patients. The derived discriminating direction found by logistic regression and a contour plot showing the probability of a patient being female are shown.

the furthest are indicated by red and points that do not move are grey.

The first mode describes a difference in size of the pelvis and in the angle between the pubic bones (pubic arch). This difference may intuitively be attributed to the difference between genders. The angle is wider in females and forms an inverted u shape while it is acute (<90°) in males as can be seen in Figure 1 [10]. The second and third modes also show some difference in size of the pelvis. In addition, a clear variation of the coverage of the femoral head by the acetabulum is visible, which is characteristic of hip dysplasia. The transition from a steep roof to a horizontal acetabular roof is especially visible in the third mode. The fourth mode, describes variation of the length of the femoral neck and shaft.

Gender differentiation

In the first regression experiment we will demonstrate the use of the complete pelvis and femur model to differentiate between gender and therewith clarify the main differences between male and female pelvis shape.

To demonstrate the interpretation of the discriminating direction found by logistic regression, we first create a regression model using the two modes that show the best separation between gender found by visual inspection of the coefficients. The scatter plot and direction discriminating between gender are shown in Figure 4. It is apparent that the derived direction optimally separates the patients by gender. The large circles indicate the points along the regression line through the mean shape associated with a probability of 10, 50, and 90 percent probability of being female.

In Figure 5 we show the resulting model discriminating between gender using 28

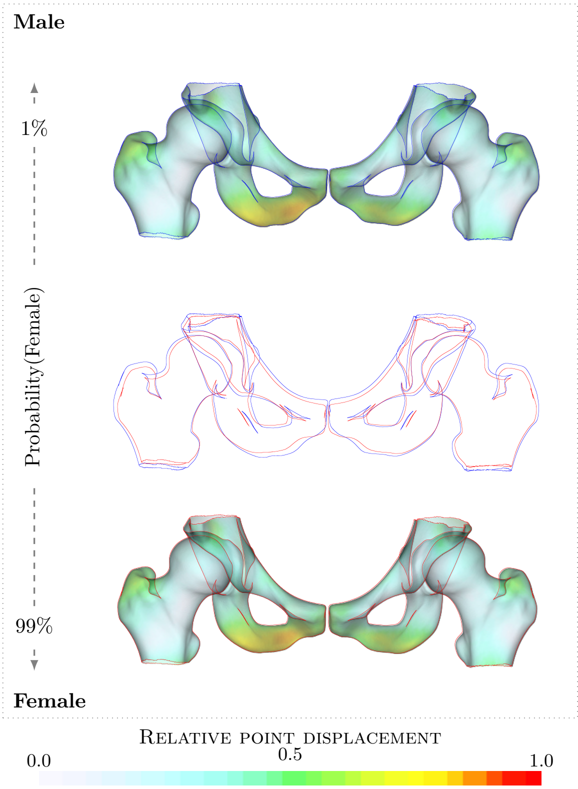

Figure 5. Visualization of difference between male and female pelvis and femur model as described by the discriminating direction found by logistic regression. An overlay of extracted contours is shown with the female (red) and male (blue). An overall difference in size and in the shape of the pubic arch can be seen.

modes which explain 95% of the total variance in the model. The model is visualized as 1% female and 99% female and an overlay of the outlines of the two is shown. The main differences between gender are a difference in size, with male being slightly larger than females and a difference in shape of the ischium highlighted by a relative point displacement of more than 0.75. In addition, the characteristic difference in shape of the pubic arch is visible. In leave-one-out cross validation, we found an area under the curve of 0.99 for predicting gender based on the logistic regression model, showing that the model has excellent predictive capabilities.

Left and right hip model

The left and right hip models are shown in Figure 6 and Figure 7 respectively. Each model is shown with the four most significant modes. Similar to the previous complete pelvis and femur model, the largest variation in the first mode is a difference in scaling. In addition a clear difference in shape of the femur is shown and the acetabulum version is changed. In other modes, variation describes changes in neck-shaft angle and in femoral coverage. In addition, it is apparent that there is a difference in head shape and subluxation of the femur.

Diagnosis of hip dysplasia

To investigate the relationship between hip dysplasia and shape, we use the individual left and right pelvic bone and femur models. The resulting models are visualized in Figure 8. The depicted variation is characteristic of hip dysplasia, showing a transition from well covered femur to a steep roof. A difference in head shape and position of the head center can also be seen. In the dysplastic hip, the head loses the spherical shape and subluxation is found. This is especially visible in the left model, where the femur moves laterally and the change is more pronounced. Leave-one-out experiments predicting hip dysplasia resulted in an area under the curve of 0.73 for the left model and 0.84 for the right model.

Diagnostic angles

In the final experiments, we demonstrate the ability to use linear regression to determine angle measurements and the associated shape variation. In Figure 9, we show the associated variation for different angle measurements for the right hip. For the center-edge angle we see that points along the lateral acetabular rim are highlighted in the lateral view. In the anterior view, it is apparent that the coverage of the femur increases with increasing center-edge angle. The overlay shows a that the main differences are present at the superiolateral edge of the acetabulum and the position of the head. The center of the femoral head moves medially for an increasing center-edge angle. Similar variation is observed for the acetabular index angle.

To study the morphological variation with respect to the version of the acetabulum, we investigate the relationship between the acetabular anteversion angle

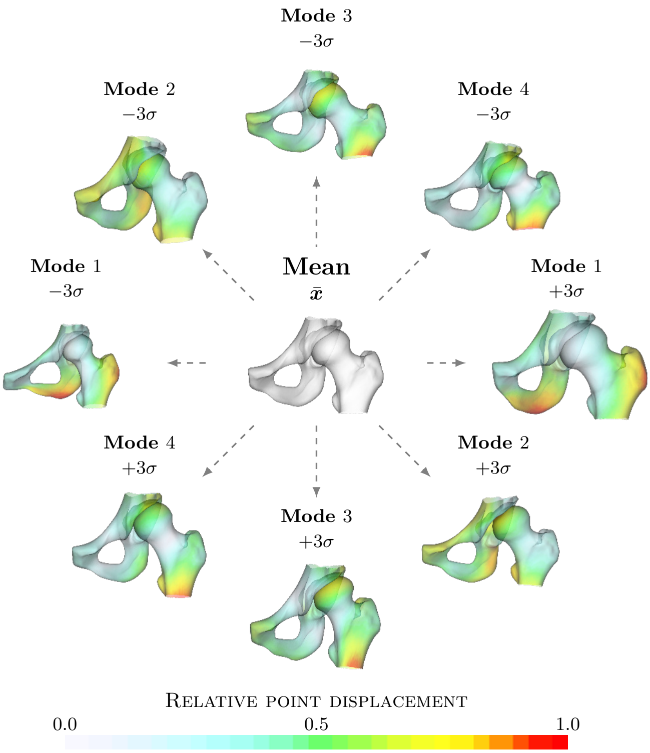

Figure 6. Visualization of the mean left pelvic bone and femur model and the four most significant modes explaining 67% of the total variation in the model. Each mode is shown as $\bar{\boldsymbol{x}} \pm 3$ standard deviations. Colors indicate the point displacement normalized by the maximum displacement for a mode.

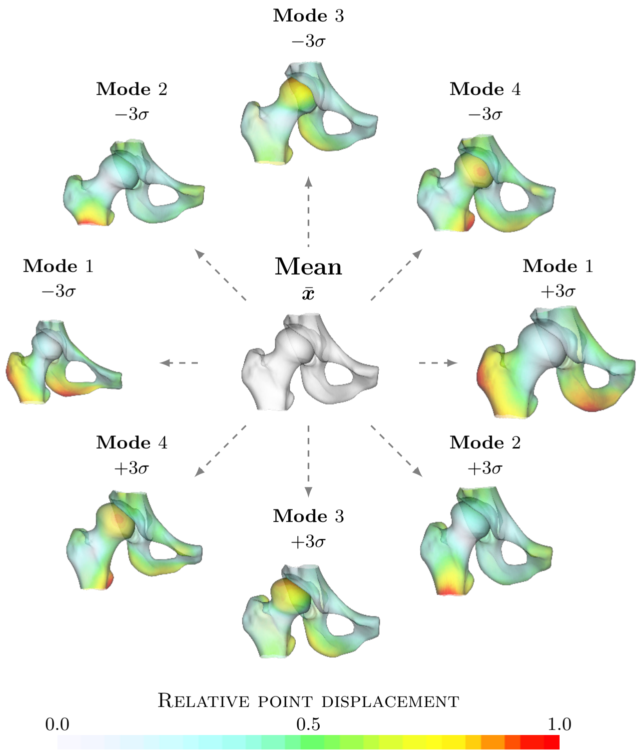

Figure 7. Visualization of the mean right pelvic bone and femur model and the four most significant modes explaining 66% of the total variation in the model. Each mode is shown as $\bar{\boldsymbol{x}} \pm 3$ standard deviations. Colors indicate the point displacement normalized by the maximum displacement for a mode.

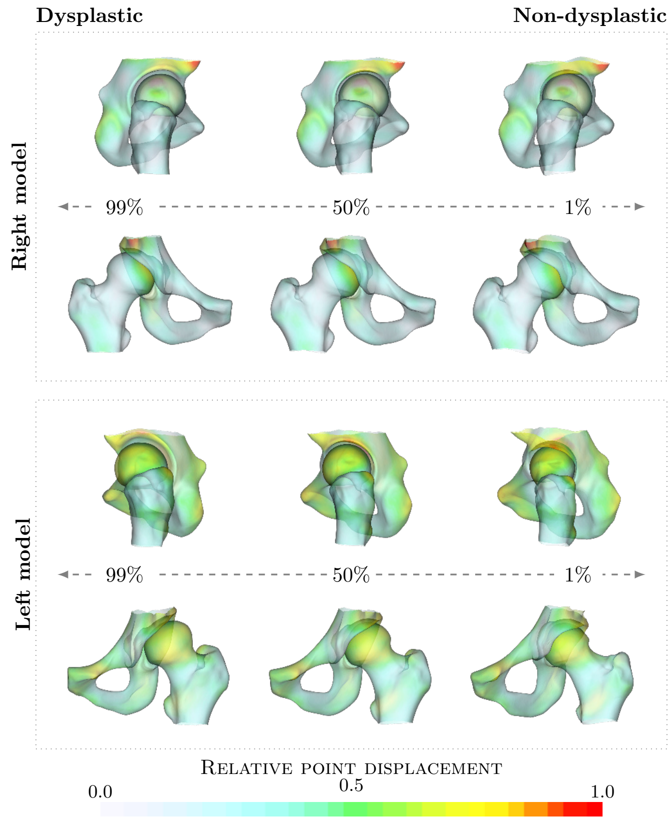

Figure 8. Visualization of difference between dysplastic and non-dysplastic hips as described by the discriminating direction found by logistic regression for the right (top) and left (bottom) models. For each model we show the lateral and anterior view. Colors indicate the point displacement normalized by the maximum displacement for a mode.

and the shape model. A strong variation along the anterior edge of the acetabulum is shown in Figure 9. Increasing acetabular anteversion results in less anterior coverage of the femur. Decreasing acetabular anteversion results in the cross-over of the lateral edge of the anterior and posterior walls of the acetabulum as well as the appearance of the prominent ischial spine sign. In the overlay of the two models, it is apparent that the anterior edge is shifted laterally along the whole height of the acetabulum, with the lines remaining approximately parallel. This is in contrast to the the variation observed for the center-edge angle and acetabular index angle, for which the change is mainly located in the superior aspect of the acetabulum. This suggests that the version influences the complete acetabulum and not only the superior aspect of the acetabulum.

In Figure 10, we show the results for the leave-one-out cross-validation experiments predicting angle measurements based on shape parameters. We find that angle measurements can be predicted within a 95% confidence interval of 10° for the center-edge and acetabular index angle. For the acetabular index, the angle can be predicted within a 95% confidence interval of approximately 5°. The small confidence interval may be due to the significant association between gender and the acetabular anteversion angle and the small standard deviation of the angle.

Discussion

In this work we presented combined statistical shape models of the symptomatic pelvis and femur. The main modes of variation describe both the difference in shape due to gender and the varying degrees of hip dysplasia. Using logistic regression, we demonstrated that the statistical shape models can be used to differentiate between gender and both dysplastic and non-dysplastic hips with an area under the curve of 0.99 and ≥ 0.73 respectively. In addition, we showed that the resulting regression model can be used to visualize the shape variation associated with the predicted dependent variables such as hip dysplasia, gender, and different angle measurements.

We found that the variation associated with gender described by the combined model was in accordance with previous findings by Decker et al. [10]. A general difference in size was observed between males and females. In females, the width of the pubic opening was observed to be larger than in males. This difference may be attributed to the extra space needed for the passage of the fetus during childbirth. The shape of the pubic arch was also different between males and females, with males having a smaller angle similar to the findings of Decker et al. [10]. The femur was larger in males than in females.

We found that the variation associated with hip dysplasia was in agreement with the typical description of the dysplastic acetabulum. The roof was steep and the coverage of the femur was incomplete. We found that the shape of the femoral head was less spherical with increasing probability of hip dysplasia. Analysis of manual angle measurements showed that the coverage of the dysplastic hip was significantly

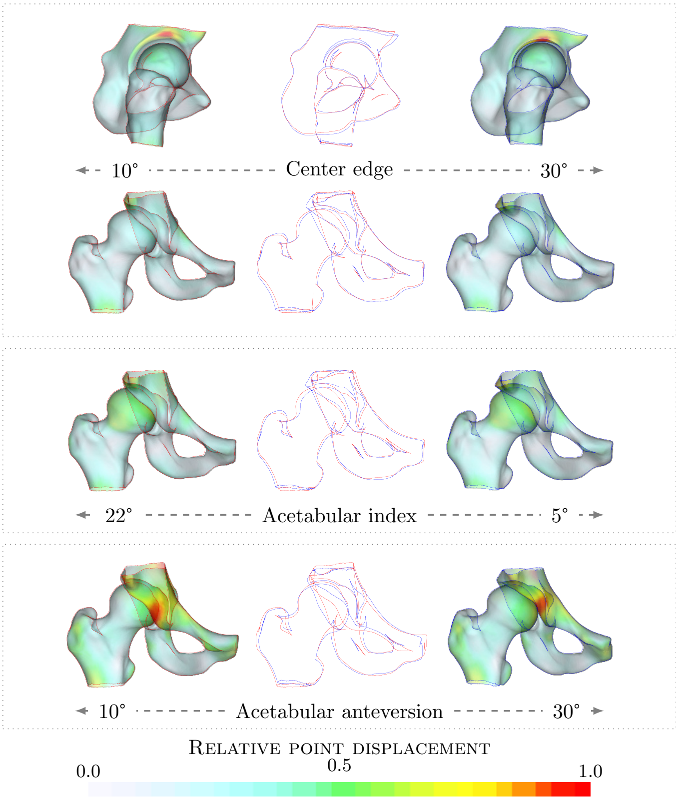

Figure 9. Visualization of the shape variation associated with the regression line found by linear regression to predict diagnostic angle measurements. Colors indicate the point displacement normalized by the maximum displacement for a mode.

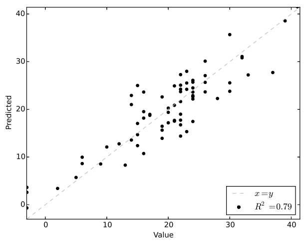

(a) Predicted CE

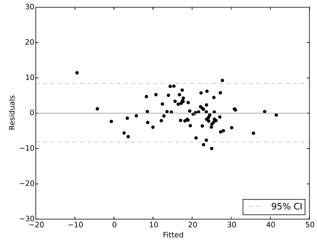

(b) Residual CE

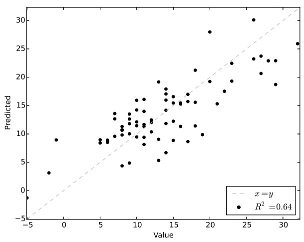

(c) Predicted AI

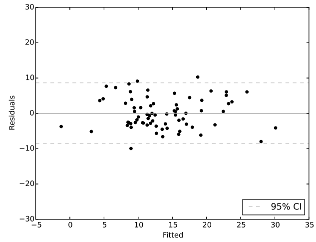

(d) Residual AI

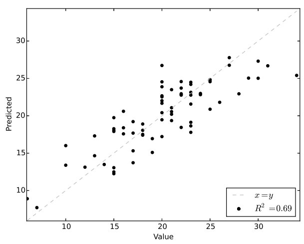

(e) Predicted AcAV

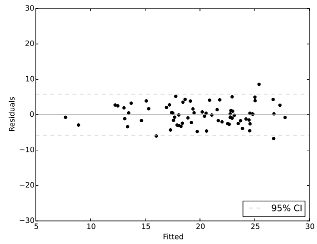

(f) Residual AcAV

Figure 10. Linear regression results predicting angle measurements using the right hip model in leave-one-out experiments. Graphs of predicted values and residuals for each angle measurement are shown.

reduced globally in agreement with the findings of Murphy et al. [1].

An interesting clinical observation is that we found that the female acetabulum is significantly more anteverted than in males. Furthermore, we found that reduced anteversion resulted in the appearance of the cross-over sign and the prominent ischial spine sign as described by [43] in a study of retroversion. Similar to previous studies [7, 43, 44], we find that the version of the acetabulum affects the whole acetabulum and is not limited to the superior aspect. This supports the suggestion by Kalberer et al [43], that appearance of the prominent ischial spine is a result of the complete rotation of the acetabulum. Larson et al. [45], also found that the cross-over sign and posterior wall sign were a frequent finding and were more common in males than in females in a asymptomatic cohort. They concluded that retroversion might be a normal variation.

In a recent study by Steppacher et al. [46], they investigated the difference in shape of the lunate surface in patients with various hip diseases. They also found similar results and concluded that the retroversion of the acetabulum was the result of malorientated acetabulum. This is in further agreement with previous two dimensional studies using radiographs [9, 47].

We found no association between hip dysplasia and acetabular anteversion. We therefore believe that the version of the acetabulum is a separate morphological variation independent of hip dysplasia. This finding is also supported by the fact that we find similar values for the acetabular anteversion angle for males and females as in normal measurements [48, 49, 50, 51] as well as in previous studies of the dysplastic hip [36, 52]. The clinical relevance of this finding may have important implications for the treatment of patients with hip dysplasia. More specifically, it may be important to consider the amount of correction applied for retroversion of the acetabulum when performing periacetabular osteotomies on male patients.

Taken together, our findings suggest that there may be an interesting explanation for the difference in observed incidence of hip dysplasia and FAI between genders. As increased retroversion is associated with increased risk of impingement [4] and males are more retroverted, it may be plausible that together they result in an increased incidence of FAI in males. Conversely, the increased incidence of hip dysplasia in females with a deficient anterior coverage may be related to the increased anteversion of the acetabulum in females.

To our knowledge, no previous study has shown the relationship between regression coefficients and the shape parameters of the statistical shape model for visualization purposes. An interesting finding was that the resulting models showed that the relative point displacement was spatially localized with areas associated with the variation. For example, the largest relative point displacements were found to be along the acetabular rim in both hip dysplasia and changes in center-edge and acetabular index angles. Although intuitive in our study, this method may be used in studies of other anatomical shapes where the link may be less clear. This method may be an alternative to methods that aim to obtain spatially localized modes or sparse modes by rotation of the PCA basis [53, 54, 55]. A clear advantage of our method compared to their methods, is that no distance metric has to be defined and the optimization of linear regression models is fast and relatively easy with standard software.

Due to the varying degree of dysplasia for patients and the fact that some patients may have a non-dysplastic contra-lateral side, it is expected that the model describes both normal and dysplastic variation to a certain extent. However, a limitation of the current study was that no normal volunteers were included in the model, but only the contralateral side of patients with unilateral hip dysplasia. In future work, we aim to create a combined model using data collected from volunteers with normal hip morphology. However, as the angle measurements in the normal hips were consistent with previous studies of the normal angles [36, 48], we believe our normal hips are representative for normal hips.

During the model building the femur position was standardized in order to remove variation due to the difference in pose of the femur. However, the difference in pose of the femur may also play a role in gender and disease morphological differences. For example, Anda et al. [36] found that the femoral anteversion was greater in dysplastic hips. However, it is also known that the femur is more anteverted in females [52]. Therefore, future investigations may develop methods to include both the shape and pose variability of the femur.

In future work, it may be interesting to investigate the relationship between morphology and outcome after treatment of hip dysplasia. For example if particular shape characteristics are predictive of conversion to a total hip arthroplasty. Since a lack of joint congruency has been associated with the early conversion to total hip arthroplasty [12], it may be of interest to explicitly model the congruency between the acetabulum and femur. In the current study only the shape parameters were used as predictors in regression model. However, it may be interesting to determine if adding additional clinical information may result in better models. Another possible direction for future work may be to use the shape model created in this study as a starting point to create patient specific three-dimensional models from pre-opertive x-rays or intra-operative fluoroscopy images using a method as described by Zheng et al. [56]. Since the current model was created based on patients with hip dysplasia, the model may be better suited to reconstruct the anatomy of the dysplastic patient. This would eliminate the need for pre-operative CT scans for use with surgical guidance systems and reduce the radiation dose to the patient.

References

1. Murphy SB, Kijewski PK, Millis MB, Harless A. Acetabular dysplasia in the adolescent and young adult. Clin Orthop Relat Res. 1990 Dec;(261):214–223.

2. Lloyd-Roberts GC. OSTEOARTHRITIS OF THE HIP A Study of the Clinical Pathology. J Bone Joint Surg Br. 1955 Feb;37-B(1):8–47.

3. Sharp IK. ACETABULAR DYSPLASIA The Acetabular Angle. J Bone Joint Surg Br. 1961 May;43-B(2):268–272.

4. Ganz R, Parvizi J, Beck M, Leunig M, Nötzli H, Siebenrock KA. Femoroacetabular impingement: a cause for osteoarthritis of the hip. Clin Orthop Relat Res. 2003 Dec;(417):112–120.

5. Ito K, Minka-II MA, Leunig M, Werlen S, Ganz R. Femoroacetabular impingement and the cam-effect. The Journal of Bone & Joint Surgery. 2001 Mar;83(2):171–176.

6. Mast JW, Brunner RL, Zebrack J. Recognizing Acetabular Version in the Radiographic Presentation of Hip Dysplasia. Clin Orthop Relat Res. 2004;(418):48–53.

7. Reynolds D, Lucas J, Klaue K. Retroversion of the acetabulum. A cause of hip pain. J Bone Joint Surg Br. 1999 Mar;81(2):281–288.

8. Li PLS, Ganz R. Morphologic features of congenital acetabular dysplasia: one in six is retroverted. Clin Orthop Relat Res. 2003 Nov;416(416):245–253.

9. Tannast M, Pfannebecker P, Schwab JM, Albers CE, Siebenrock KA, Büchler L. Pelvic morphology differs in rotation and obliquity between developmental dysplasia of the hip and retroversion. Clin Orthop Relat Res. 2012;470(12):3297–3305.

10. Decker SJ, Davy Jow SL, Ford JM, Hilbelink DR. Virtual Determination of Sex: Metric and Nonmetric Traits of the Adult Pelvis from 3D Computed Tomography Models. Journal of Forensic Sciences. 2011 Sep;56(5):1107–1114.

11. Ganz R, Klaue K, Vinh TS, Mast JW. A new periacetabular osteotomy for the treatment of hip dysplasias. Technique and preliminary results. Clin Orthop Relat Res. 1988 Jul;(232):26–36.

12. Hartig-Andreasen C, Troelsen A, Thillemann TM, Søballe K. What Factors Predict Failure 4 to 12 Years After Periacetabular Osteotomy? Clin Orthop Relat Res. 2012 Nov;470(11):2978–2987.

13. Heimann T, Meinzer HP. Statistical shape models for 3D medical image segmentation: a review. Med Image Anal. 2009 Aug;13(4):543–563.

14. Sarkalkan N, Weinans H, Zadpoor AA. Statistical shape and appearance models of bones. Bone. 2014;60:129–140.

15. Cootes TF, Taylor CJ, Cooper DH, Graham J. Active Shape Models-Their Training and Application. Computer Vision and Image Understanding. 1995 Jan;61(1):38–59.

16. Agricola R, Reijman M, Bierma-Zeinstra S, Verhaar JAN, Weinans H, Waarsing JH. Total hip replacement but not clinical osteoarthritis can be predicted by the shape of the hip: a prospective cohort study (CHECK). Osteoarthr Cartil. 2013 Apr;21(4):559–564.

17. Waarsing JH, Kloppenburg M, Slagboom PE, Kroon HM, Houwing-Duistermaat JJ, Weinans H, et al. Osteoarthritis susceptibility genes influence the association between hip morphology and osteoarthritis. Arthritis Rheum. 2011 May;63(5):1349–1354.

18. Barr RJ, Gregory JS, Gregory JS, Reid DM, Reid DM, Aspden RM, et al. Predicting OA progression to total hip replacement: Can we do better than risk factors alone using active shape modelling as an imaging biomarker? Rheumatology (Oxford). 2012;51(3):562–570.

19. Chan EF, Farnsworth CL, Koziol JA, Hosalkar HS, Sah RL. Statistical shape modeling of proximal femoral shape deformities in Legg–Calvé–Perthes disease and slipped capital femoral epiphysis. Osteoarthritis and Cartilage. 2013 Mar;21(3):443–449.

20. Harris MD, Datar M, Whitaker RT, Jurrus ER, Peters CL, Anderson AE. Statistical shape modeling of cam femoroacetabular impingement. J Orthop Res. 2013;31(10):1620–1626.

21. Cates J, Fletcher PT, Styner M, Hazlett HC, Whitaker R. Particle-based shape analysis of multi-object complexes. In: Metaxas D, Axel L, Fichtinger G, Székely G, editors. Med Image Comput Comput Assist Interv. Scientific Computing and Imaging Institute, Univ. Utah, Salt Lake City, UT, USA.. Berlin, Heidelberg: Springer Berlin Heidelberg; 2008. p. 477–485.

22. Seghers D, D'Agostino E, Maes F, Vandermeulen D, Suetens P. Construction of a brain template from MR images using state-of-the-art registration and segmentation techniques. Lecture Notes in Computer Science. 2004;3216(PART 1):696–703.

23. Krčah M, Székely G, Blanc R. Fully automatic and fast segmentation of the femur bone from 3D-CT images with no shape prior. In: ISBI; 2011. p. 2087–2090.

24. De Raedt S, Mechlenburg I, Stilling M, Rømer L, Søballe K, de Bruijne M. Automated measurement of diagnostic angles for hip dysplasia. In: Proceedings of SPIE - The International Society for Optical Engineering; 2013. .

25. De Raedt S, Mechlenburg I, Stilling M, Rømer L, Søballe K, de Bruijne M. Lunate Extract: Fully automatic acetabular lunate segmentation and hip angle measurements. Submitted. 2015;.

26. Metz CT, Baka N, Kirisli H, Schaap M, Klein S, Neefjes LA, et al. Regression-Based Cardiac Motion Prediction From Single-Phase CTA. Medical Imaging, IEEE Transactions on. 2012 May;31(6):1311–1325.

27. Metz CT, Klein S, Schaap M, van Walsum T, Niessen WJ. Nonrigid registration of dynamic medical imaging data using nD + t B-splines and a groupwise optimization approach. Med Image Anal. 2011 Apr;15(2):238–249.

28. Lorensen WE, Cline HE. MARCHING CUBES: A HIGH RESOLUTION 3D SURFACE CONSTRUCTION ALGORITHM. Computer Graphics (ACM). 1987;21(4):163–169.

29. Gower JC. Generalized procrustes analysis. Psychometrika. 1975;40(1):33–51.

30. Hoerl AE, Kennard RW. Ridge Regression: Biased Estimation for Nonorthogonal Problems. Technometrics. 1970 Feb;12(1):55–67.

31. Golub GH, Hansen PC, O'Leary DP. Tikhonov Regularization and Total Least Squares. SIAM J Matrix Anal & Appl. 1999 Jan;21(1):185–194.

32. Golub GH, Heath M, Wahba G. Generalized Cross-Validation as a Method for Choosing a Good Ridge Parameter. Technometrics. 1979 May;21(2):215–223.

33. de Bruijne M, Lund MT, Tankó LB, Pettersen PC, Nielsen M. Quantitative vertebral morphometry using neighbor-conditional shape models. Med Image Anal. 2007 Oct;11(5):503–512.

34. Wiberg G. Studies on dysplastic acetabula and congenital subluxation of the hip joint. Acta Orthop Scand. 1939;83(Supplementum 58).

35. Tönnis D. Congenital Dysplasia and Dislocation of the Hip in Children and Adults. Berlin, Heidelberg: Springer Berlin Heidelberg; 1987.

36. Anda S, Terjesen T, Kvistad KA, Svenningsen S. Acetabular angles and femoral anteversion in dysplastic hips in adults: CT investigation. J Comput Assist Tomogr. 1991;15(1):115–120.

37. Troelsen A, Rømer L, Kring S, Elmengaard B, Søballe K. Assessment of hip dysplasia and osteoarthritis: Variability of different methods. Acta Radiol. 2010;51(2):187–193.

38. Klein S, Staring M, Murphy K, Viergever MA, Pluim JPW. elastix: a toolbox for intensity-based medical image registration. IEEE Trans Med Imaging. 2010 Jan;29(1):196–205.

39. Shamonin DP, Bron EE, Lelieveldt BPF, Smits M, Klein S, Staring M, et al. Fast parallel image registration on CPU and GPU for diagnostic classification of Alzheimer's disease. Front Neuroinform. 2013;7:50.

40. Martin K, Lorensen B. The Visualization Toolkit. An Object-oriented Approach to 3D Graphics. Ingram; 2006.

41. Albrecht T, Gass T, Goksel O, Lüthi M. Statismo-A framework for PCA based statistical models. Insight. 2012;.

42. Pedregosa F, Varoquaux G, Gramfort A, Michel V, Thirion B, Grisel O, et al. Scikit-learn: Machine learning in Python. Journal of Machine Learning Research. 2011;12:2825–2830.

43. Kalberer F, Kalberer F, Sierra RJ, Sierra RJ, Madan SS, Madan SS, et al. Ischial spine projection into the pelvis: A new sign for acetabular retroversion. Clin Orthop Relat Res. 2008;466(3):677–683.

44. Fujii M, Nakashima Y, Sato T, Akiyama M, Iwamoto Y. Pelvic deformity influences acetabular version and coverage in hip dysplasia. Clin Orthop Relat Res. 2011 Jun;469(6):1735–1742.

45. Larson CM, Moreau-Gaudry A, Kelly BT, Thomas Byrd JW, Tonetti J, Lavallee S, et al. Are Normal Hips Being Labeled as Pathologic? A CT-based Method for Defining Normal Acetabular Coverage. Clin Orthop Relat Res. 2014;.

46. Steppacher SD, Lerch TD, Gharanizadeh K, Liechti EF, Werlen SF, Puls M, et al. Size and shape of the lunate surface in different types of pincer impingement: theoretical implications for surgical therapy. Osteoarthritis and Cartilage. 2014 Jul;22(7):951–958.

47. Jamali AA, Mladenov K, Meyer DC, Martinez A, Beck M, Leunig M. Anteroposterior pelvic radiographs to assess acetabular retroversion: high validity of the "cross-over-sign". J Orthop Res. 2007 Jun;25(6):758–765.

48. Tallroth K, Lepisto J. Computed tomography measurement of acetabular dimensions: normal values for correction of dysplasia. Acta Orthop. 2006 Aug;77(4):598–602.

49. Köhnlein W, Ganz R, Impellizzeri FM, Leunig M. Acetabular morphology: implications for joint-preserving surgery. Clin Orthop Relat Res. 2009 Mar;467(3):682–691.

50. Nakahara I, Takao M, Sakai T, Nishii T, Yoshikawa H, Sugano N. Gender differences in 3D morphology and bony impingement of human hips. J Orthop Res. 2011 Mar;29(3):333–339.

51. Murtha PE, Hafez MA, Jaramaz B, DiGioia AM. Variations in acetabular anatomy with reference to total hip replacement. J Bone Joint Surg Br. 2008 Mar;90(3):308–313.

52. Hetsroni I, Dela Torre K, Duke G, Lyman S, Kelly BT. Sex differences of hip morphology in young adults with hip pain and labral tears. Arthroscopy. 2013 Jan;29(1):54–63.

53. Van De Giessen M, De Raedt S, Stilling M, Hansen TB, Maas M, Streekstra GJ, et al. Localized component analysis for arthritis detection in the trapeziometacarpal joint. In: MICCAI. Berlin, Heidelberg: Springer Berlin Heidelberg; 2011. p. 360–367.

54. Alcantara D, Carmichael O, Delson E, Harcourt-Smith W, Sterner K, Frost S, et al. Localized components analysis. Inf Process Med Imaging. 2007;20:519–531.

55. Alcantara DA, Carmichael O, Harcourt-Smith W, Sterner K, Frost SR, Dutton R, et al. Exploration of shape variation using localized components analysis. IEEE Transactions on Pattern Analysis and Machine Intelligence. 2009;31(8):1510–1516.

56. Zheng G, Gollmer S, Schumann S, Dong X, Feilkas T, González Ballester MA. A 2D/3D correspondence building method for reconstruction of a patient-specific 3D bone surface model using point distribution models and calibrated X-ray images. Med Image Anal. 2009 Dec;13(6):883–899.

Paper III

Treatment and computer assisted PAO

Clin Orthop Relat Res manuscript No.
(will be inserted by the editor)

Are computer reported measurements during periacetabular osteotomy using a minimally invasive approach reliable?

Sepp De Raedt · Inger Mechlenburg · Maiken Stilling · Lone Rømer · Ryan J. Murphy · Mehran Armand · Jyri Lepisto · Marleen de Bruijne · Kjeld Søballe

Abstract *Introduction* Periacetabular osteotomy is the treatment of choice for younger patients with developmental hip dysplasia. The procedure aims to normalize the joint configuration, reduce the peak-pressure, and delay the development of osteoarthritis. However, the surgical procedure is technically demanding and surgeons may benefit from intra-operative computer navigation assistance especially with minimally invasive surgery. No previous study has validated the use of computer navigation with a minimally invasive transsartorial approach.

Questions/purposes Therefore we investigated if (1) intra-operative computer navigation reported angle measurements agree with manual angle measurements and if (2) peak-pressure decrease post-operatively?

Methods Computer assisted periacetabular osteotomy (PAO) was performed on ten patients. Patients underwent pre- and post-operative computed tomography (CT) scanning with a standardized protocol. Preoperative preparation consisted of outlining the lunate surface and segmenting the pelvis and femur from CT data. The Biomechanical Guidance System was used intra-operatively to automatically calculate diagnostic angles and peak-pressure measurements. The reorientation was performed under fluoroscopy guidance. Manual diagnostic angle measurements were performed based on pre- and post-operative CT. Differences in angle measurements were investigated with summary statistics, intraclass correlation coefficient, and Bland-Altman plots. The percentage post-operative change in peak-pressure was calculated.

Results Intra-operative reported angle measurements show a good agreement with manual angle measurements with intraclass correlation coefficient in the range of 0.94 to 0.98. Computer navigation reported angle measurements were significantly higher for the posterior sector angle (1.65°, $p=0.001$) and the acetabular anteversion angle (1.24°, $p=0.004$). No significant difference was found for the center-edge ($p=0.056$), acetabular index ($p=0.212$), and anterior sector angle ($p=0.452$). Peak-pressure decreased by a mean of 13% and was significantly different (95% CI: 4% to 22%, $p=0.008$).

Conclusions In this work, we have shown that computer navigation can reliably be used with a minimally invasive transsartorial approach periacetabular osteotomy. Angle measurements agree with manual measurements and peak-pressure was shown to decrease

Sepp De Raedt · Inger Mechlenburg · Maiken Stilling
Dept. of Clinical Medicine, Aarhus University, Aarhus, Denmark
E-mail: Sepp.De.Raedt@clin.au.dk

Sepp De Raedt · Inger Mechlenburg
Orthopaedic Research Unit, Aarhus University Hospital, Aarhus, Denmark

Maiken Stilling · Kjeld Søballe
Dept. of Orthopaedics, Aarhus University Hospital, Aarhus, Denmark

Løne Romer
Dept. of Radiology, Aarhus University Hospital, Aarhus, Denmark

Ryan J. Murphy · Mehran Armand
Dept. of Research and Engineering Development,Johns Hopkins University Applied Physics Laboratory, Laurel, MD, USA
Dept. of Mechanical Engineering, Johns Hopkins University, Baltimore, MD, USA

Jyri Lepisto
Orton Orthopaedic Hospital, Helsinki, Finland

Marleen de Bruijne
Depts. of Radiology and Medical Informatics, Erasmus MC Rotterdam, Rotterdam, The Netherlands
Dept. of Computer Science, University of Copenhagen, Copenhagen, Denmark

post-operatively. With further development, the system will become a valuable tool in the operating room for both experienced and less experienced surgeons performing PAO. Further studies with a larger cohort and follow-up will allow us to investigate the association with peak-pressure and post-operative outcome and pave the way to clinical introduction.

1 Introduction

In patients with developmental hip dysplasia, the coverage of the femur by the acetabulum is insufficient, leading to pain, disability, and early development of osteoarthritis [6, 20, 21, 22, 25]. For patients, without any development of osteoarthritis, a joint preserving periactabular osteotomy (PAO) has become the treatment of choice [15, 26]. During the procedure, the acetabulum is cut free, while leaving the posterior pelvic column intact, and repositioned, normalizing the joint configuration in order to reduce the peak-pressure and increase the lateral coverage [26, 9]. This is thought to delay the onset of osteoarthritis and improve the survival of the natural joint [11, 27]. However, PAO is a technically demanding procedure and intraoperative evaluation of the applied correction can be difficult due to the lack of three-dimensional feedback during surgery when using standard single tube fluoroscopy.

With the development of computer assisted surgery systems, such as the Biomechanical Guidance System (BGS), the surgeon can visualize and gain important intra-operative three dimensional feedback during the procedure [3, 14, 16]. The BGS provides intra-operative tracking of the acetabular fragment and displays diagnostic angles and peak-pressure measurements in real-time. In particular, the acetabular version is difficult for the surgeon to determine with the use of fluoroscopy due to imaging limitations in two dimensions.

Previous work on computer assisted PAO has been based on the procedure introduced by Ganz et al [9] or a modified rotational osteotomy [12]. A minimally invasive transsartorial approach developed by Søballe et al. aims to reduce soft tissue trauma and consequently lessen the duration of surgery, blood loss, transfusion requirements, and length of postoperative rehabilitation [26]. However, it is unclear if this minimally invasive approach is compatible with navigation surgery because the incision from the anterior superior iliac spine descending along the sartorius muscle is only 7 cm long [26]. This offers reduced visibility and limits the accessibility when using the optically tracked pointer of the navigation system [16]. Therefore, it is important to ensure that the method is compatible and to validate the accuracy of computer reported angle measurements against manual CT angle measurements. The goal of PAO is to reduce the peak contact pressure for daily activities; however it is unknown how the peak-pressure changes post-operatively. Finally, no previous study has reported the use of intra-operative navigation system on patients with hip dysplasia. Therefore we investigated if (1) intra-operative computer navigation reported angle measurements agree with manual angle measurements and if (2) peak-pressure decrease post-operatively?

2 Materials and Methods

The study was a prospective case series study conducted at Aarhus University Hospital, Denmark. Patients were recruited and operated on between September 2013 and January 2014.

Written informed consent was obtained and ethical approval was obtained from the Central Denmark Region Committee on Biomedical Research Ethics (Journal Number: M-20100274). The study was registered at Clinical Trials.gov (NCT02015247). In the inclusion period, all patients (n=65) with hip dysplasia scheduled for PAO were identified and considered for inclusion. Inclusion criteria were: radiological diagnosed dysplasia (center-edge angle $< 25°$), osteoarthritis degree ≤ 1 according to the criteria of Tönnis and Heinecke [25], and hip pain. Exclusion criteria were: Legg-Calvé-Perthes disease, neuromuscular diseases, previous major hip surgery, persons with cognitive problems, and age < 18. Due to the need for cleaning and sterilizing the navigation instruments between surgeries, only one patient could be included per day of operation. When multiple candidates were available, the final decision was left to the discretion of the senior author (KS) and the most technically challenging patient was selected. In particular, patients with a retroverted acetabulum were included to evaluate the reliability of the system with a range of cases typically seen in clinical practice.

Patients underwent pre-operative computed tomography imaging on a Brilliance 64 (Philips Healthcare, Best, The Netherlands) one week prior to scheduled surgery. Patients were scanned in a supine position from above the L5S1 joint until below the lesser trochanter. All scans were acquired with a voxel size of $0.45 \times 0.45 \times 0.7$mm. Post-operative scanning was performed one day post-operatively using the same protocol. The bony pelvis and femurs were automatically segmented by a graph cut segmentation technique and a surface model of the pelvis was created [13, 8, 7]. The lunate surface was manually segmented using the lunate-trace method described by Armiger et al [2]. A pre-operative

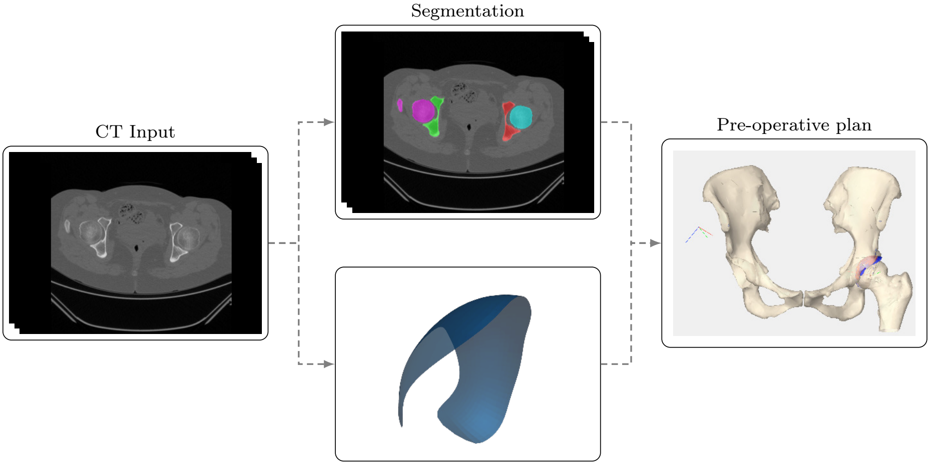

Fig. 1: The pre-operative workflow consisted of obtaining computer tomograph (CT) scans, segmentation of the bony pelvis and the lunate surface. Finally, a pre-operative plan was made using the BGS system.

surgical plan was created based on the biomechanically predicted optimal alignment [3, 16, 18]. However, the surgical plan was not used during surgery and was not revealed to the surgeon in accordance with IRB approval. The pre-operative workflow is shown in Figure 1.

The surgical setup follows that described in Murphy et al [16]. In summary, prior to the start of the surgery, a Polaris optical tracking system (Northern Digital Inc., Waterloo, Canada) was setup on the contralateral side. During surgery, the surgical assistant performed a pivot calibration of the optically tracked pointer and the navigation system. The surgeon performed the opening and initial approach as described in [26]. In addition, on the contralateral side two small incisions were made on the iliac crest and the base of the removable reference geometry (BrainLab, Feldkirchen, Germany) was fixated with two screws. The reference geometry establishes a fixed reference allowing the tracking of the fragment. Before the iliac osteotomy, the pelvis surface model was registered to the patient anatomy. An initial registration was established by touching the anterior superior iliac spine on the operative and contralateral side and the anterior inferior iliac spine on the operative side with the pointer. After collecting surface points on the ilium, pubis, and the iliac crest, a point to surface registration was performed [4]. Before the final osteotomy, four evenly spaced small indentations, referred to as fiducials, on the planned fragment were created using a 1 mm bone burr. The initial position of the fragment was recorded by touching the fiducials with the pointing device. The final osteotomy was completed and the surgeon reoriented the fragment under fluoroscopic guidance. As noted above, the BGS optimized surgical plan was not used during reorientation. When satisfied with the final positioning, the fragment was fixated by use of two cannulated screws and the final position was recorded by touching the fiducials again in the same order. Validation of the BGS system on cadavers was performed and was previously reported by Murphy et al [16]. The procedure was practiced on six cadavers prior to patient inclusion by the operating surgeon and surgical team in order to reduce the learning curve and establish an efficient workflow. The intra-operative workflow is shown in Figure 2.

The patients were ambulatory 6 hours after surgery, allowed 30 kg of weight-bearing on the operated leg and were discharged to their home 2-3 days after PAO.

The following diagnostic angles were measured based on CT data and recorded: center-edge angle of Wiberg [29], acetabular index angle of Tönnis [24], posterior sector, anterior sector, and the acetabular anteversion angle [1]. Measurements were performed using Aarhus Ortho-measure based on the medical imaging interaction toolkit (MITK [19]) previously validated with an inter- and intra-observer in an unpublished study showing a good intra- and inter-operative reliability with ICC > 0.94 for all angle measurements. The program provides the user with an axial, coronal, and sagittal view of the CT data. After selecting the centers of the femoral heads and the most anterior point

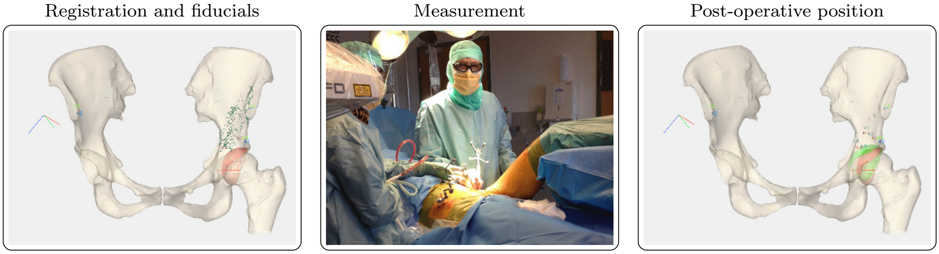

Fig. 2: A schematic overview of the intra-operative workflow.

on the L5S1 joint, the volume is re-orientated such that the axis aligns the centers of the femoral heads. Subsequently, the anterior, posterior, lateral and medial point of the lunate is selected for each hip. Angle measurements are then calculated between the points. Measurements were repeated to determine the intra-observer reliability in the current study. An experienced operator (SDR) performed all measurements.

BGS reported angle and pressure measurements were calculated based on the segmented lunate surface. In summary, the angle measurements were calculated by finding the intersection points between the lunate trace and the coronal or axial plane [2]. Subsequently, the angles were calculated according to standard definitions. Pressure measurements were based on discrete-element analysis, which finds the peak-pressure by simulating the joint force and modeling the pressure distribution on the surface [3].

The agreement between computer reported angle measurements and manual measurements were examined by summary statistics and the intraclass correlation coefficient (ICC) and Bland-Altman plots to examine bias and limits of agreement [5]. The change in peak-pressure was analyzed as percentage change with respect to baseline. Data was tested for normality by using Shapiro-Wilk test in addition to Skewness and Kurtosis tests. Normally distributed data with equal variances was tested with a paired T-test. Significance level was set at $p < 0.05$. In this pilot study the study size was set to ten patients. All analysis was performed using Stata 13 (StataCorp, College Station, USA).

The study population consisted of 3 males and 7 females (10 patients). The mean age was 32 (median: 31.5, range: 20 to 47) years.

3 Results

Do intra-operative computer navigation reported angle measurements agree with manual angle measurements? We found a good agreement between manual and BGS reported angle measurements with ICC varying between 0.94 and 0.98. Results are shown in Table 1. Bland-Altman plots for each angle are shown in Figure 3. No statistically significant difference was found for the center-edge (p=0.056), acetabular index (p=0.212), and anterior sector (p=0.452) angles. A statistically significant difference was found for the posterior sector (p=0.001) and acetabular anteversion (p=0.004) angles. For one patient, the anterior inferior edge of the lunate surface was superior to the center of the femoral head. As a result, no anterior reference point for the calculation of the anterior sector and the acetabular anteversion angle could be found. Hence, the corresponding angle measurements could not be performed and the patient was excluded for analysis for the corresponding angles. Results for repeated manual measurements are shown in Table 2. A good agreement between repeated manual angle measurements was found with ICC ranging from 0.95 to 0.99. A significant difference was found for the anterior sector angle (p=0.007).

Does peak-pressure decrease post-operatively? The mean difference in peak-pressure after surgery was −13% (95% CI −22% to −4%, p=0.008). In one patient, the peak-pressure increased by 5% post-operatively.

4 Discussion

In PAO, accurate intra-operative evaluation of the reorientation of the acetabular fragment is crucial to obtaining satisfactory results and long-term survival of the biological hip joint [11, 26]. Traditional use of single plane fluoroscopy allows the evaluation of the center-edge angle and acetabular index. However, evaluating the posterior and anterior coverage and the acetabular version using a false profile view with fluoroscopy is difficult. Using a computer navigation system such as the BGS, all angle measurements can be reported as intra-operative feedback to the surgeon, and the peak-pressures without subjecting the patient to extra

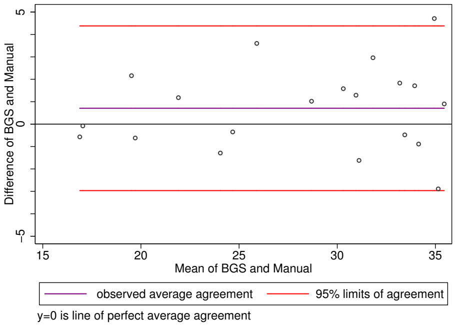

(a)

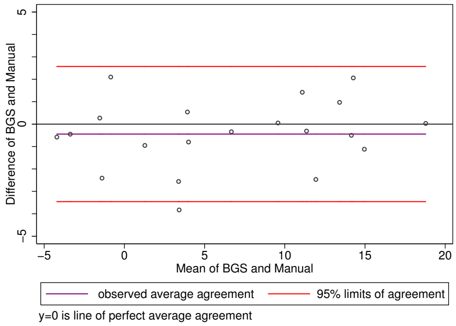

(b)

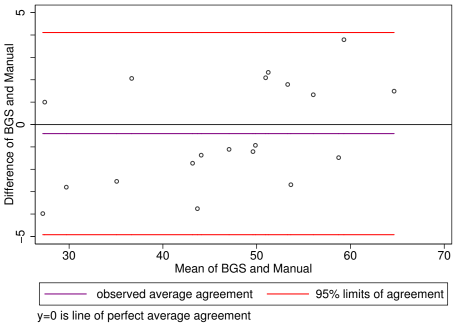

(c)

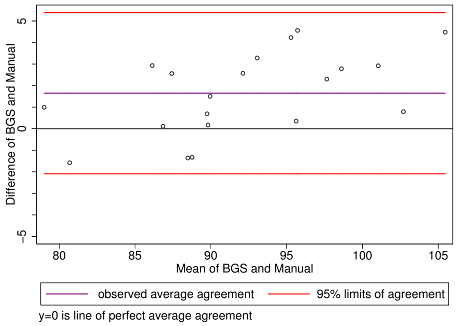

(d)

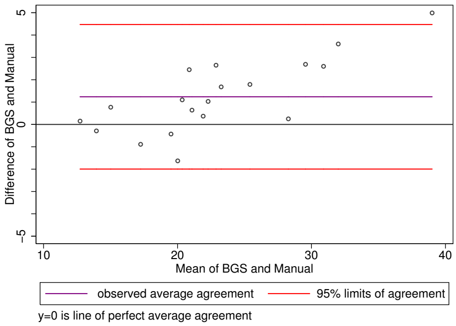

(e)

Fig. 3: Bland-Altman plots comparing manual measurements to intra-operative computer navigation reported angle measurements.

Table 1: Summary of result comparing between manual and BGS reported angle measurements

Angle	ICC	Avg. Diff.	SD	95 % CI		p-value
Center-edge	0.95	0.86	1.88	−0.03	1.74	0.056
Acetabular index	0.98	−0.44	1.54	−1.16	0.28	0.212
Acetabular anteversion	0.95	1.24	1.65	0.44	2.03	0.004*
Posterior sector	0.94	1.65	1.91	0.75	2.53	0.001*
Anterior sector	0.98	−0.41	2.3	−1.51	0.71	0.452

Table 2: Summary of result comparing repeated manual measurements

Angle	ICC	Avg. Diff.	SD	95 % CI		p-value
Center-edge	0.98	0.42	1.2	−0.14	0.98	0.137
Acetabular index	0.98	−0.14	1.31	−0.75	0.47	0.648
Acetabular anteversion	0.98	0.01	1.28	−0.59	0.61	0.979
Posterior sector	0.95	0.15	2.07	−0.82	1.12	0.745
Anterior sector	0.99	−0.86	1.26	−1.44	−0.27	0.007*

intra-operative radiation. In this study we validated the intra-operative measured angle measurements against manual CT-based angle measurements and evaluated the change in peak-pressure.

This study had a number of limitations. First, the study population was limited to ten patients as an initial pilot study on patients to gain experience with the procedure. However, previous to this study the surgeon and surgical team performed a cadaver study with six cadavers to reduce the learning curve using BGS and streamline the surgical workflow. Validation of the BGS system was previously performed on 19 cadavers [16]. Second, reorientation was performed under fluoroscopic guidance without use of the information from the navigation system or the BGS calculated pre-operative plan. We therefore did not evaluate the ability of the surgeon to achieve the BGS proposed pre-operative plan. However, comparing the BGS calculated plan with post-operative results, we found that the optimized reorientation based on peak-pressure differed from the reorientation performed by the surgeon. It is however unclear if the system optimized reorientation leads to long-term satisfactory outcome or if the used algorithm should be adapted to match the planning of an experienced surgeon. In particular, overcorrection may lead to the risk of femoroacetabular impingement and should be taken into account during automatic pre-operative planning [17]. This should be validated in a larger randomized control study. Third, the pressure calculations are based on the lunate surface based on the boney structure of the acetabulum. A more accurate pressure distribution could be calculated by using the cartilage and the labrum. However, techniques for the accurate segmentation of the cartilage and labrum require CT arthrography or magnetic resonance imaging [23]. However, it is believed that the pressure distribution based on CT segmentations of the lunate surface are an accurate approximation of the joint pressures [3, 16, 18].

We found a good agreement between computer navigation reported angle measurements and manual angle measurements with similar results to repeated manual measurements. In a previous study, they found a mean difference between $-0.46°$ to $0.42°$ and a standard deviation between $2.73°$ to $3.30°$ in this study with three observers [2]. We find a similar range in mean difference and a slightly smaller standard deviations in the current study. This might be attributed to higher quality CT volumes and a smaller in-plane voxel size (0.4 mm versus 1.0 mm), allowing for more accurate landmark identification. As noted by Armiger et al [2], a difference of 1.0 mm in landmark identification can result in a 2° difference in angle measurement. We found a statistically significant difference for the acetabular anteversion and posterior sector angles between the intra-operative and manual measurements. From Figure 3, it is apparent that the BGS exhibits a slight bias with respect to manual measurements. However, the 95% limits of agreement are within the expected variation from previous inter- and intra-observer studies and we conclude that the variation is within the clinically acceptable range [28].

We found that the peak-pressure decreased by a mean of 13% post-operatively in the current study. For one patient, the peak-pressure increased by 5% post-operatively. In [3], they found a similar case showing an increase of 5% in peak-pressure. They associated the increase with lateral overcorrection and a negative acetabular index angle. This also corresponds to the measurements reported by the BGS system center-edge: 33.3° and acetabular index: $-2.6°$. However, manual angle measurements were center-edge: 30.1° and acetabular index: −0.1°. These values are within optimal acetabular angle limits with a center-edge angle between 30° and 40° and acetabular index of less than 10° [10].

In a previous study on the validation of the BGS planning system on 29 dysplastic subjects, a mean decrease of 49.2% was found after optimal reorientation [18]. The optimal plan was calculated by the BGS based on biomechanical simulation of the peak-pressure. This decrease was much larger than we found in the current study. However, the average change in center-edge angle was also larger ($-19.0 \pm 7.7°$) compared to in the current study ($-10 \pm 6°$). The smaller correction needed for the patients in the current study may therefore lead to a smaller decrease in peak-pressure.

5 Conclusions

In this work we investigated and validated the use of computer navigation with a minimally invasive transsartorial approach for PAO on patients with hip dysplasia. The system offers reliable angle measurements intra-operatively and provides the surgeon with three-dimensional visualization of the applied reorientation and the peak-pressure. The additional information with respect to that obtained by fluoroscopy may especially be of value for less experienced surgeons. However, the system may become an important tool for both less experienced and experienced surgeons to ensure optimal reorientation is achieved for all patients. Further studies with a larger cohort and follow-up will allow us to investigate the association with peak-pressure and post-operative outcome and pave the way to clinical introduction.

References

1. Anda S, Terjesen T, Kvistad KA, Svenningsen S (1991) Acetabular angles and femoral anteversion in dysplastic hips in adults: CT investigation. J Comput Assist Tomogr 15(1):115–120
2. Armiger RS, Armand M, Lepisto J, Minhas D, Tallroth K, Mears SC, Waites MD, Taylor RH (2007) Evaluation of a computerized measurement technique for joint alignment before and during periacetabular osteotomy. Comput Aided Surg 12(4):215–224
3. Armiger RS, Armand M, Tallroth K, Lepisto J, Mears SC (2009) Three-dimensional mechanical evaluation of joint contact pressure in 12 periacetabular osteotomy patients with 10-year follow-up. Acta Orthop 80(2):155–161
4. Besl PJ, McKay ND, McKay ND (1992) A method for registration of 3-D shapes. IEEE Transactions on Pattern Analysis and Machine Intelligence 14(2):239–256
5. Bland JM, Altman DG (1986) Statistical methods for assessing agreement between two methods of clinical measurement. Lancet 1(8476):307–310
6. Cooperman DR, Wallensten R, Stulberg SD (1983) Acetabular dysplasia in the adult. Clin Orthop Relat Res No. 175(175):79–85
7. De Raedt S, Mechlenburg I, Stilling M, Rømer L, Søballe K, de Bruijne M (2013) Automated measurement of diagnostic angles for hip dysplasia. In: Proceedings of SPIE - The International Society for Optical Engineering
8. De Raedt S, Mechlenburg I, Stilling M, Rømer L, Søballe K, de Bruijne M (2015) Lunate Extract: Fully automatic acetabular lunate segmentation and hip angle measurements. Submitted
9. Ganz R, Klaue K, Vinh TS, Mast JW (1988) A new periacetabular osteotomy for the treatment of hip dysplasias. Technique and preliminary results. Clin Orthop Relat Res (232):26–36
10. Hartig-Andreasen C, Troelsen A, Thillemann TM, Søballe K (2012) What Factors Predict Failure 4 to 12 Years After Periacetabular Osteotomy? Clin Orthop Relat Res 470(11):2978–2987
11. Hipp JA, Sugano N, Millis MB, Murphy SB (1999) Planning acetabular redirection osteotomies based on joint contact pressures. Clin Orthop Relat Res (364):134–143
12. Hsieh PH, Shih CH, Lee PC, Yang WE, Lee ZL (2003) A modified periacetabular osteotomy with use of the transtrochanteric exposure. J Bone Joint Surg Am 85(2):244–250
13. Krčah M, Székely G, Blanc R (2011) Fully automatic and fast segmentation of the femur bone from 3D-CT images with no shape prior. In: ISBI, pp 2087–2090
14. Lepisto J, Armand M, Armiger RS (2008) Periacetabular osteotomy in adult hip dysplasia - developing a computer aided real-time biomechanical guiding system (BGS). Suom Ortoped Traumatol 31(2):186–190
15. Leunig M (2011) Evolution of technique and indications for the Bernese periacetabular osteotomy. Bull NYU Hosp Jt Dis 69 Suppl 1:S42–6
16. Murphy RJ, Armiger RS, Lepisto J, Mears SC, Taylor RH, Armand M (2014) Development of a biomechanical guidance system for periacetabular

osteotomy. Int J Comput Assist Radiol Surg pp 1–12

17. Myers SR, Eijer H, Ganz R (1999) Anterior femoroacetabular impingement after periacetabular osteotomy. Clin Orthop Relat Res (363):93–99
18. Niknafs N, Murphy RJ, Armiger RS, Lepisto J, Armand M (2013) Biomechanical factors in planning of periacetabular osteotomy. Front Bioeng Biotechnol 1:20
19. Nolden M, Zelzer S, Seitel A, Wald D, Müller M, Franz AM, Maleike D, Fangerau M, Baumhauer M, Maier-Hein L, Maier-Hein KH, Meinzer HP, Wolf I (2013) The Medical Imaging Interaction Toolkit: challenges and advances : 10 years of open-source development. Int J Comput Assist Radiol Surg 8(4):607–620
20. Reijman M, Hazes JMW, Hazes JMW, Pols HAP, Pols HAP, Koes BW, Koes BW, Bierma-Zeinstra S (2005) Acetabular dysplasia predicts incident osteoarthritis of the hip: The Rotterdam study. Arthritis Rheum 52(3):787–793
21. Sharp IK (1961) ACETABULAR DYSPLASIA The Acetabular Angle. J Bone Joint Surg Br 43-B(2):268–272
22. Siebenrock KA, Schöll E, Lottenbach M (1999) Bernese periacetabular osteotomy. Clin Orthop Relat Res (363):9–20
23. Tabrizi PR, Zoroofi RA, Yokota F, Tamura S, Nishii T, Sato Y (2015) Acetabular cartilage segmentation in CT arthrography based on a bone-normalized probabilistic atlas. Int J Comput Assist Radiol Surg 10(4):433–446
24. Tönnis D (1987) Congenital Dysplasia and Dislocation of the Hip in Children and Adults. Springer Berlin Heidelberg, Berlin, Heidelberg
25. Tönnis D, Heinecke A (1999) Acetabular and femoral anteversion: Relationship with osteoarthritis of the hip. J Bone Joint Surg Am 81(12):1747–1770
26. Troelsen A, Elmengaard B, Søballe K (2008) A new minimally invasive transsartorial approach for periacetabular osteotomy. J Bone Joint Surg Am 90(3):493–498
27. Troelsen A, Elmengaard B, Søballe K (2009) Medium-term outcome of periacetabular osteotomy and predictors of conversion to total hip replacement. J Bone Joint Surg Am 91(9):2169–2179
28. Troelsen A, Rømer L, Kring S, Elmengaard B, Søballe K (2010) Assessment of hip dysplasia and osteoarthritis: Variability of different methods. Acta Radiol 51(2):187–193
29. Wiberg G (1939) Studies on dysplastic acetabula and congenital subluxation of the hip joint. Acta Orthop Scand 83(Supplementum 58)